“In the realm of chiroptical spectroscopy, electronic circular dichroism is considered the king. For about 50 years, this technique has been applied worldwide to successfully solve problems related to absolute configuration and to elucidate conformational and supramolecular aspects in complex cases.

Much less known and even less employed is its emission counterpart: circularly polarized luminescence or CPL.„

2016

UNIVERSITÀ DI PISA

CPL: from spectroscopy to applications

F. Zinna

Circularly Polarized Luminescence

from spectroscopy to applications

Francesco Zinna

UNIVERSITÀ DI PISA

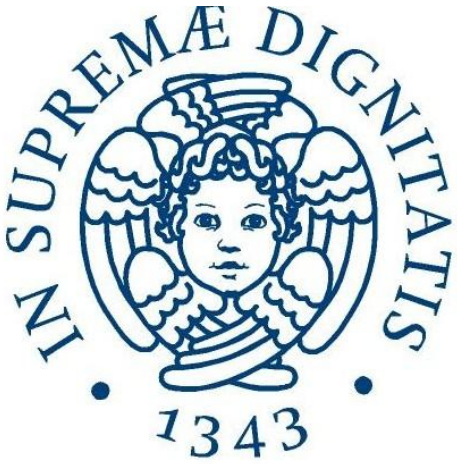

Doctoral school in Chemistry and Materials Sciences

XXIX Cycle

PhD thesis

Circularly polarized luminescence: from spectroscopy to applications

Candidate:

Francesco Zinna

Supervisor:

Prof. Lorenzo Di Bari

2016

On the cover: light spirals from: freeimageslive.co.uk

Abstract

Chiral molecules can emit left and right polarized light with different intensities; this phenomenon is known as circularly polarized luminescence (CPL). CPL can be observed in photoluminescence and in electroluminescence. In general CPL spectroscopy can be an interesting tool to investigate the chirality of the excited state or it can be employed in technological applications such as OLEDs able to directly emit circularly polarized electroluminescence (CP-OLEDs).

The first part of this work concerns chiral lanthanide complexes, which can emit CPL with a degree of circular polarization which is almost precluded to non-aggregated purely organic molecules. In this part, we present a new chiral Eu complex with highly polarized emission and, a series of CP-OLEDs based on a lanthanide complex. Following this strategy, the highest polarization degree reported to date is obtained. Moreover, we discuss and rationalize the factors affecting the polarization inside a device.

In the second part, we investigate the CPL properties of chiral organic molecules and we apply CPL spectroscopy as a qualitative analytical tool in pH-dependent chiroptical switch and to signal the interaction between fluorescent stains and protein-based matrices used in paintings.

Table of contents

General introduction

In the realm of chiroptical spectroscopy, electronic circular dichroism (ECD) is considered the king. For about 50 years, this technique has been applied worldwide to successfully solve problems related to absolute configuration[1] and to elucidate conformational[2] and supramolecular[3] aspects in complex cases.

Much less known and even less employed is its emission counterpart: *circularly polarized luminescence* or CPL.

CPL is observed when luminescent chiral molecules or systems emit right and left polarized light with different intensities. In a typical CPL experiment, the sample is excited with non-polarized light and the two circularly polarized components (left, I_L and right I_R) are collected separately, the half sum of these two components is the total luminescence spectrum, while their difference ($I_L - I_R$) is the CPL signal.

While ECD probes the chirality of the ground state, CPL is a valuable tool to study the chirality of the excited states.[4] In particular:

- It gives information about the chirality of the luminescent state.
- It allows one to observe transitions that can not be observed in absorption as is often the case with $f \rightarrow f$ transitions of lanthanides (see Chapter 1).
- Usually one transition is observed in emission, while many overlapping transitions are usually recorded in absorption. Even in complex systems, one may expect to observe emission mainly from the lowest excited state (cfr. Kasha's rule).[5]
- Sometimes the chirality of the ground state may not be sufficient to give rise to ECD signals, but nevertheless the excited state could give a CPL signal (see Chapter 1, 5, 7).

In principle, the circular polarization of the emission does not depend on the pathway that the molecule (or the molecular system) follows to reach the excited

state. Commonly CP emission is observed following photoexcitation (CP photoluminescence), either exciting the same electronic transition from which one is going to observe emission or exciting a different transition from which the energy is then transferred to a different emitting excited state.[4]

The first observation of CP photoluminescence was made in 1948 by Samojlov[6] on a chiral uranyl acetate crystal. In 1967 Emeis and Oosterhoff[7] measured the CPL of the n→π* transition of a chiral ketone (*Trans*-β-hydrindanone, see Chapter 5, Scheme 5-1) and the circular polarization of the phosphorescent transition of $Cr(en)_3(ClO_4)_3$; in the same work they proposed the theory describing chiroptical activity in emission.[7,8] Since then, CPL was observed on lanthanide complexes[9-11] (in solution and in crystals), and on many organic molecules and metallorganic[1] complexes.[12] Moreover, CPL activity was reported for racemic mixture upon excitation with circularly polarized light[13,14] and for achiral/racemic molecules upon interaction with chiral environments[15-17] (induced CPL). Nowadays, CPL is observed from supramolecular aggregates of chiral organic molecules[18] (small molecules[19-22] and polymers[23-25]); in such cases it is possible to study supramolecular aggregation (joining ECD with CPL) and to investigate the chirality of emitting excimers. CPL of aggregate systems will *not* be a subject of this work.

It is also possible to observe CP emission when semiconductor materials (either chiral or doped with some chiral molecules) experience an electric current sufficient to induce electroluminenscence (CP electroluminescence). The first example was reported in 1997 by Dekkers et al.,[26] measuring CP electroluminescence in an organic LED in which the active layer contained a chiral poly-phenylene vinylene polymer (see Chapter 3).

Furthermore, a chiral molecule can be excited by a chemical reaction and emit CP chemiluminescence. This phenomenon was observed for the first time by Dekkers et al.[27] in 1976 for an optically active dioxetane.

---

[1] In this case, *metallorganic* is referred only to *d*-metal complexes. Lanthanide complexes generally display much stronger CPL properties and will be treated separately

Moreover, in principle it would be possible to observe CP emission following a mechanical excitation: mechanoluminescence such as sonoluminescence or triboluminescence. To the best of our knowledge, no example of CP mechanoluminescence has been reported so far, although there is no fundamental reason preventing one from obtaining CP mechanoluminescence from mechanoluminescent chiral systems. However, the practical measurement poses some experimental issues, also possibly on the account that mechanoluminescence phenomena are not yet fully understood at a molecular level.

The extent of CPL is usually quantified through the l*uminescence dissymmetry factor g*,[28] defined as:

$$g = \frac{I_L - I_R}{1/2(I_L + I_R)} = \frac{\Delta I}{I} \qquad \text{with} \qquad I = \frac{1}{2}(I_L + I_R) \qquad (1)$$

Where I_L and I_R are the left and right polarized emission intensities respectively. The factor 2 is needed to normalize the total emission ($I_L + I_R$). It follows immediately that g = ±2 means complete polarization of the emitted light while 0 corresponds to an unpolarized emission. It should be noted that only up to a factor of 2, Eq. 1 closely retraces the classical definition of enantiomeric excess, and therefore g could be interpreted as the excess of one polarization over the other in the emitted light.

In this work, we shall refer to the dissymmetry factor measured for photoexcited system as g_{PL} (photoluminescence g) and g_{EL} in the case of circularly polarized electroluminescence.

Despite being an old spectroscopic technique, CPL can represent a useful tool even in modern research in the domain of chirality (see Chapter 1 for some examples). Beside spectroscopy, in recent years, many examples of applications of CPL in the most diverse fields were proposed. In particular, CPL finds a natural applications in chiral optoelectronics and photonics (e.g. in electronic devices able to emit circularly polarized light),[26,29,30] information technology

(e.g. in optical data storage, since different information can be encoded in different polarization state),[31-33] and chiral photoswitches.[34]

The present doctoral work arises from such a contest and tries to address the following points.

- The need of chiral molecules emitting bright and highly polarized light. In order to accomplish this task, a rigorous spectroscopic work joined with a rational insight is required in first place to asses and understand the chiroptical properties of different molecules.
- Development of electronic devices (OLEDs) able to emit highly circularly polarized electroluminescence based on a completely new approach. In the same time, the factors affecting the polarization inside a device, beside the intrinsic emission of the chiral emitter, must be identified and rationalized.
- New spectroscopic applications for CPL as a qualitative analytical tool.

Thesis outline

This work is divided in two parts. Part I (Chapters 1-4) concerns CPL of chiral lanthanide systems, Part II (Chapters 5-8) describes CPL investigations of single chiral organic molecules (not aggregated) in different contexts and our home-made instrument used for such studies. All the chapters, except Chapters 5, contain material which is either published or submitted to publication.

The first chapter of each part serves as an introduction, putting into context the following chapters.

Part I:

- **Chapter 1.** CPL of chiral lanthanide complexes, examples of applications and the fundamental reasons for their outstanding chiroptical properties.[35]

- **Chapter 2.** Synthesis and spectroscopic characterization (paramagnetic NMR and solution and solid state ECD/CPL) of new lanthanide complexes based on carvone.[36]
- **Chapter 3.** Development of circularly polarized OLEDs (CP-OLEDs) based on chiral lanthanide complexes and discussion of factors affecting the polarization inside a device (reflection on the cathode).[30]
- **Chapter 4.** Optimization of the concept of Ln-based CP-OLEDs and a more advanced rationalization of the effects of the device architecture on the polarization performances.[37]

Part II:

- **Chapter 5.** Brief overview of different single organic molecules employed for CPL.
- **Chapter 6.** CPL spectroscopic and computational study of axially chiral BODIPYs.[38]
- **Chapter 7.** CPL study of a helicene with pH-dependent chiroptical switch behaviour.[39]
- **Chapter 8.** Study of the interaction between some fluorescent stains and protein matrices used in painting using CPL spectroscopy.[40]
- **Chapter 9.** Description of our home-made spectrofluoropolarimeter.[38]

References

[1] N. Berova, L. Di Bari , G. Pescitelli, *Chem. Soc. Rev.*, **2007**, *36*, 914.
[2] G. Pescitelli, L. Di Bari , N. Berova, *Chem. Soc. Rev.*, **2011**, *40*, 4603.
[3] G. Pescitelli, L. Di Bari , N. Berova, *Chem. Soc. Rev.*, **2014**.
[4] J. P. Riehl , F. S. Richardson, *Chem. Rev.*, **1986**, *86*, 1.
[5] M. Kasha, *Discuss. Faraday Soc.*, **1950**, *9*, 14.
[6] B. Samojlov, *J.Exp.Theor. Phys.*, **1948**, *18*, 1030.
[7] C. Emeis , L. Oosterhoff, *Chem. Phys. Lett.*, **1967**, *1*, 129.
[8] C. A. Emeis , L. J. Oosterhoff, *J. Chem. Phys.*, **1971**, *54*, 4809.
[9] C. K. Luk , F. Richardson, *Chem. Phys. Lett.*, **1974**, *25*, 215.
[10] H. G. Brittain, *J. Am. Chem. Soc.*, **1980**, *102*, 3693.
[11] A. Das Gupta , F. Richardson, *Inorg. Chem.*, **1981**, *20*, 2616.
[12] T. Wu, X.-Z. You , P. Bouř, *Coord. Chem. Rev.*, **2015**, *284*, 1.
[13] H. P. Dekkers, C. Emeis , L. J. Oosterhoff, *J. Am. Chem. Soc.*, **1969**, *91*, 4589.
[14] G. Nilmes , J. Riehl, *J. Phys. Chem.*, **1983**, *87*, 3300.
[15] D. H. Metcalf, S. W. Snyder, S. Wu, G. L. Hilmes, J. P. Riehl, J. Demas , F. Richardson, *J. Am. Chem. Soc.*, **1989**, *111*, 3082.
[16] K. Kano, H. Matsumoto, S. Hashimoto, M. Sisido , Y. Imanishi, *J. Am. Chem. Soc.*, **1985**, *107*, 6117.
[17] H. Brittain , F. Richardson, *J. Phys. Chem.*, **1976**, *80*, 2590.
[18] J. Kumar, T. Nakashima , T. Kawai, *J. Phys. Chem. Lett.*, **2015**, *6*, 3445.
[19] J. Kumar, H. Tsumatori, J. Yuasa, T. Kawai , T. Nakashima, *Angew. Chem. Int. Ed.*, **2015**, *54*, 5943.
[20] H. Li, J. Cheng, H. Deng, E. Zhao, B. Shen, J. W. Lam, K. S. Wong, H. Wu, B. S. Li , B. Z. Tang, *J. Mater. Chem. C*, **2015**, *3*, 2399.
[21] Z. Shen, T. Wang, L. Shi, Z. Tang , M. Liu, *Chem. Sci.*, **2015**, *6*, 4267.
[22] J. Li, C. Yang, C. Huang, Y. Wan , W.-Y. Lai, *Tetrahedron Lett.*, **2016**, *57*, 1256.
[23] D. Yang, Y. Zhao, K. Lv, X. Wang, W. Zhang, L. Zhang , M. Liu, *Soft Matter*, **2016**, *12*, 1170.
[24] Y. Zhao, N. A. Abdul Rahim, Y. Xia, M. Fujiki, B. Song, Z. Zhang, W. Zhang , X. Zhu, *Macromol.*, **2016**, *49*, 3214.
[25] S. Zhang, Y. Sheng, G. Wei, Y. Quan, Y. Cheng , C. Zhu, *Polym. Chem.*, **2015**, *6*, 2416.
[26] E. Peeters, M. P. Christiaans, R. A. Janssen, H. F. Schoo, H. P. Dekkers , E. Meijer, *J. Am. Chem. Soc.*, **1997**, *119*, 9909.
[27] H. Wynberg, H. Numan , H. Dekkers, *J. Am. Chem. Soc.*, **1977**, *99*, 3870.
[28] J. P. Riehl , F. S. Richardson, *Chem. Rev.*, **1986**, *86*, 1.
[29] Y. Yang, R. C. da Costa, D. M. Smilgies, A. J. Campbell , M. J. Fuchter, *Adv. Mater.*, **2013**, *25*, 2624.
[30] F. Zinna, U. Giovanella , L. Di Bari, *Adv. Mater.*, **2015**, *27*, 1791.
[31] C. Wang, H. Fei, Y. Qiu, Y. Yang, Z. Wei, Y. Tian, Y. Chen , Y. Zhao, *Appl. Phys. Lett.*, **1999**, *74*, 19.
[32] C. Wagenknecht, C.-M. Li, A. Reingruber, X.-H. Bao, A. Goebel, Y.-A. Chen, Q. Zhang, K. Chen , J.-W. Pan, *Nat. Photonics*, **2010**, *4*, 549.

[33] R. Farshchi, M. Ramsteiner, J. Herfort, A. Tahraoui , H. Grahn, *Appl. Phys. Lett.*, **2011**, *98*, 162508.
[34] B. L. Feringa, *Acc. Chem. Res.*, **2001**, *34*, 504.
[35] F. Zinna , L. Di Bari, *Chirality*, **2015**, *27*, 1.
[36] F. Zinna, C. Resta, S. Abbate, E. Castiglioni, G. Longhi, P. Mineo , L. Di Bari, *Chem. Commun.*, **2015**, *51*, 11903.
[37] F. Zinna, M. Pasini, F. Galeotti, C. Botta, L. Di Bari , G. Umberto, *Adv. Funct. Mater.*, **2016**, *in the press*, doi: 10.1002/adfm.201603719.
[38] F. Zinna, T. Bruhn, C. A. Guido, J. Ahrens, M. Bröring, L. Di Bari , G. Pescitelli, *Chem. Eur. J.*, **2016**, *22*, 16089.
[39] S. Pascal, C. Besnard, F. Zinna, L. Di Bari, B. Le Guennic, D. Jacquemin , J. Lacour, *Org. Biomol. Chem.*, **2016**, *14*, 4590.
[40] S. Orsini, F. Zinna, T. Biver, L. Di Bari , I. Bonaduce, *Rsc Advances*, **2016**, *6*, 96176.

Part I

Lanthanide circularly polarized luminescence

Chapter 1

Introduction to part I

Compared to *d*-metals, lanthanides (III) are endowed with peculiar spectroscopic features.[1-3] Their absorption and emission bands are narrow and the energies of their electronic transitions are largely independent of the coordination environments. They can be considered spherical emitters in ordinary solutions with a long excited state life-time (up to milliseconds), so they have sufficient time to randomly re-orientate themselves losing any possible preferential excitation due to linearly polarized light (photoselection), which could possibly lead to artefacts when measuring CPL spectra.

Purely electric-dipole intraconfigurational *f→f* transitions are Laporte-forbidden and are associated with very small absorption bands ($\varepsilon = 1-10^2\ M^{-1}cm^{-1}$), but they can be conveniently observed in emission, once they reach an excited state by means of some energy transfer process. Usually this is made possible through a so-called antenna effect, which requires that the organic ligand[2] absorbs high energy radiation and passes excitation onto the Ln(III).

Lanthanide coordination chemistry is well known,[7] this allows one to rationally design ligands containing chromophoric groups:[8] if the electronic levels of donor (ligand) and acceptor (lanthanide) match[2] and if they are in close proximity and with the correct lifetimes, the ligand-to-lanthanide energy transfer process can be quite efficient.[3]

In fact high quantum yields are possible especially for Eu^{3+} and Tb^{3+} in the visible (red and green) region. At the moment, one can reasonably predict the main features of a successful complex, and justify *a posteriori* its experimental

[2] There are some reports of *d-f* dimetallic complexes where the absorbing chromophore is the *d*-metal.[4-6]

[3] This mechanism ensures large Stokes shift: 250 nm can be typical.

behaviour. This leads to a rational ligand design, although not always the final products meet the expectations, because of the multiple parameters involved in the process.

For these characteristics, luminescent Ln^{3+} have been employed with various purposes, such as:[9] molecular probes for biomedical imaging and sensing[10] and bioanalytical applications[11] (see below for some examples), electroluminescent devices,[12-15] in photovoltaics as spectrum downshifters,[16] in telecommunications,[17] and as dyes in security inks and labels.[3,18]

In addition, when the emissive complex is chiral non racemic, it may emit *circularly polarized luminescence*.

While organic chiral molecules or macromolecules typically display g_{PL} values of 10^{-4}–10^{-2}, lanthanide complexes show values of 0.1–1,[19-21] with 1.38 being the highest value ever reported so far for a lanthanide complex[22] (and, to the best of our knowledge, one of the highest values ever measured at all).

In the literature there are only rare and relatively old examples of measurements in the solid state, possibly due to special experimental care that should be taken when measuring chiroptical properties in solid state. However the current interest for applications of lanthanide luminescence in devices of various types is soliciting a new interest in solid state CPL.

Where to look for high g_{PL} values

High g_{PL} values are to be sought for among electric dipole forbidden/magnetic dipole allowed transitions.

In fact, for the transition $i \rightarrow j$, the luminescence dissymmetry factor can be written as:

$$g_{\mathrm{PL}} = 4\frac{|\boldsymbol{\mu}_{ij}|\cdot|\mathbf{m}_{ji}|}{|\boldsymbol{\mu}_{ij}|^2+|\mathbf{m}_{ji}|^2}\cdot\cos\theta_{\boldsymbol{\mu},\mathbf{m}} \qquad (1\text{-}1)$$

where $\boldsymbol{\mu}_{ij}$ e $\mathbf{m}_{ji}$ are the electric and magnetic transition dipole vectors and $\theta_{\boldsymbol{\mu},\mathbf{m}}$ is the angle between them. In the case of an electric dipole allowed transition, the $|\mathbf{m}_{ji}|^2$ term is negligible with respect to $|\boldsymbol{\mu}_{ij}|^2$; so Eq. (1-1) becomes:

$$g_{\mathrm{PL}} = 4\frac{|\mathbf{m}_{ji}|}{|\boldsymbol{\mu}_{ij}|}\cdot\cos\theta_{\boldsymbol{\mu},\mathbf{m}} \qquad (1\text{-}2)$$

with the $|\mathbf{m}_{ji}|/|\boldsymbol{\mu}_{ij}|$ ratio being well less than 1.

Strict Laporte selection rule can not apply in chiral molecules, because rotation-reflection elements, like symmetry planes and inversion centres are excluded by chirality itself. Nonetheless, if the chromophore can be considered intrinsically achiral, then one can generally expect that for some of its electronic transitions, $\boldsymbol{\mu}_{ij}$ is very small so that g_{PL} may become sizeable (but in any case smaller than 2).

Richardson[23] classified lanthanide transitions into three classes (*DI*, *DII* and *DIII*) concerning the dissymmetry factor: the magnitude of the observed dissymmetry factors is expected to decrease as *DI*>*DII*>*DIII*. Richardson himself noted that the Eu^{3+} $^5D_0\rightarrow{}^7F_1$ is the only lanthanide transition belonging to class *DI* easily accessible to CPL measurement; no wonder that the highest g_{PL} values have been measured for this transition.

Beside Eu^{3+}, CPL spectra in the visible region are commonly measured for Sm^{3+},[22,24] Tb^{3+},[24,25] and Dy^{3+}[24] complexes; in Table 1-1 we show the transitions generally observed in CPL measurements and their *D* class.

Table 1-1. Ln^{3+} transitions generally observed in CPL measurements with their D class[23] and their approximate wavelength.

Ion	**Transition**	**Wavelength** (nm)	**Class**
Sm^{3+}	$^4G_{5/2}\rightarrow{}^6H_{5/2}$	565	*DII*
	$^4G_{5/2}\rightarrow{}^6H_{7/2}$	595	*DIII*
Eu^{3+}	$^5D_0\rightarrow{}^7F_1$	595	*DI*
Tb^{3+}	$^5D_4\rightarrow{}^7F_5$	545	*DII*
Dy^{3+}	$^4F_{9/2}\rightarrow{}^6H_{11/2}$	670	*DIII*

CPL and total luminescence

Although the emission bands of most lanthanide complexes are very narrow, especially compared to those of organic or *d*-metal emitters, very often they display a fine structure, consisting in lines of one or a few nm width.

Taking as an example the $^5D_0 \rightarrow {}^7F_J$ transitions associated to an Eu^{3+} complex, it can be noted that the initial state is singly degenerate, while the final state is *(2J+1)*–fold degenerate in a total symmetric environment: depending on the coordination sphere, this degeneracy can be removed,[26,27] leading to a splitting of the emission band.

The energy gap among these levels can be as small as 100–130 cm^{-1}, which translates in 5 nm or less in the yellow-orange region.

As a consequence, at room temperature, sometimes this may be only partially resolved.

As it occurs in other spectroscopies where bands may have different signs, and very notably in electronic and vibrational CD, in CPL there may be an apparent resolution enhancement when nearby transitions have opposite rotational strengths.

This is notably the case of the CPL spectrum shown in Figure 1-1, concerning the $^5D_4 \rightarrow {}^7F_5$ transition of a Tb^{3+} chiral complex.[28]

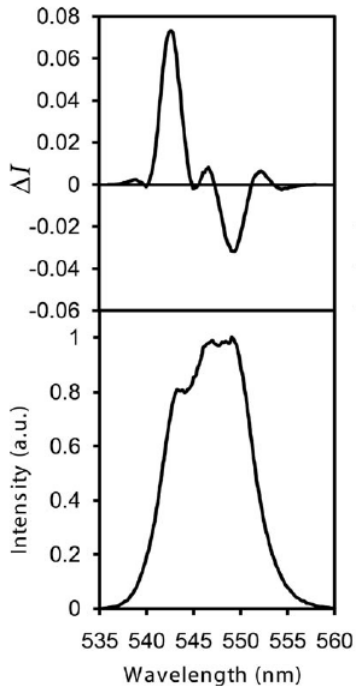

Figure 1-1. CPL and total emission of a Tb^{3+} complex for $^5D_4 \rightarrow {}^7F_5$ transition. Notice how the manifold is resolved in CPL spectrum (reproduced with permission from Ref [28]).

Clearly, when this happens, total emission and CPL bands do not coincide in general and special care should be taken in evaluating the g_{PL} value.

Knowing the energies of the *J* levels provides useful information about the crystal field environment which in turn can be correlated with the polarizability of the donor groups.[29]

Often lanthanide complexes in solution give rise to multiple species of different symmetry and shape which may also be involved in a network of equilibria: in any case the number of lines of each term-to-term manifold cannot exceed the multiplicity of the states involved in the transition.

In fact, before luminescence occurs, the system rearranges to a single low energy excited state sublevel. If the number of apparent transitions in a given multiplet is larger than expected, this can be taken as a strong indication that there is more than one emitting species.

For example, the observation of a single sharp band for the $^5D_0 \rightarrow {}^7F_0$ transition around 580 nm is often used as an argument in favour of the presence of a single emitting species.

In fact the $^7F_0$ level is non-degenerate and a true single band is expected. However this transition is usually quite weak and the multiplicity can remain hidden within the band width;[27,30] moreover, owing to the small extent of spin-orbit couplings and the crystal field effects which modulate the exact wavelength of lanthanide *f*→*f* transitions, accidental degeneracy of the $^5D_0 \rightarrow {}^7F_0$ within several (exchanging) species is possible, which would lead to a true single band in that region.

When dealing with such a situation in chiral complexes, it can be convenient to excite the complex with left, right and linearly polarized light; if there is a single emitting species, no significant change of the CPL spectrum will be visible.[31]

Development of complexes with high g_{PL} values

Macrocycles and podates

Cyclen (L^1) and its smaller relative triazacyclononane (L^2, Scheme 1-1) are versatile scaffolds to be functionalized at the N-atoms with arms bearing coordinating groups such as carboxylates, amides, phosphinates and N-donors; central chirality elements can be introduced in the ring or, more frequently, on the side-arms at a carbon centre.[32-35]

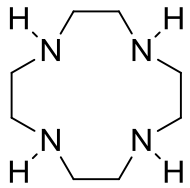

L^1

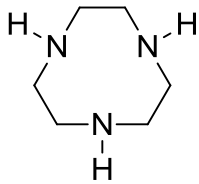

L^2

Scheme 1-1. Cyclen (L^1) and triazacyclononane (L^2)

The arms can carry also a chromophore (e.g. aryl, etheroaryl, azaxanthones) able to sensitize the lanthanide ion. These complexes were extensively exploited as CPL probes by Parker's group (see Section below).

Podate complexes were shown to strongly bind Ln^{3+} ions, saturating their coordination sphere and shielding them from other coordinating molecules, such as H_2O. This makes them suitable for application in aqueous solutions; water in the first coordination sphere can be a major issue in Ln emission, since O-H is a high-energy oscillator and can lead to a non-radiative deactivation of the luminescence.[36,37]

Raymond et al.[24,25] reported the ligand L^3, in which four 2-hydroxyisophthalamide pendant arms are bound to ethylendiamine; the arms are further functionalized with a 1-phenylethylamine substituent each, encoding the chiral information (Scheme 1-2).

This ligand has proven to be particularly efficient in sensitising four different Ln^{3+} ions,[4] namely: Sm^{3+}, Eu^{3+}, Tb^{3+}, Dy^{3+}. All these complexes display good emission and CPL activity. Unfortunately, the geometry and the coordination mode of these complexes remains undetermined.

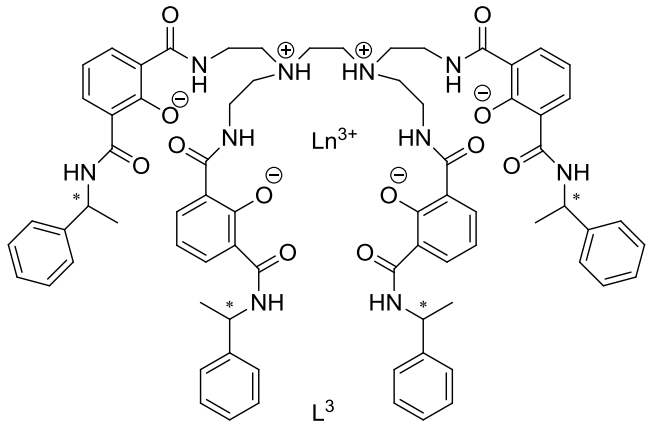

Scheme 1-2. Conjectural structure for the podate lanthanide complexes reported by Raymond et al.[24] (Ln = Sm, Eu, Tb, Dy). The stereogenic centers are homochiral and the complex was prepared and characterized with both ligand enantiomers.

[4] It may be interesting to notice that the same ligand was also employed to sensitize curium(III).[38]

The same structural motif was employed to develop similar ligands, designed to provide a bigger steric hindrance and shield the Ln^{3+} ion from water coordination in a more effective way.[25]

β-diketonates

Due to the oxophilicity of Ln^{3+} ions, β-diketonates are effective coordinating molecules for lanthanide ions. Through their use, it is possible to prepare *tetrakis* complexes, which are often resistant to moisture, thanks to the bidentate nature of the ligand: indeed, this leads to an 8-coordination number, and to the fact that the resulting complex is anionic.[5]

Neutral *tris* species can also be prepared but their coordination sphere must be completed by at least a molecule of water or other Lewis bases such as bipyridines or phenanthrolines.

β-diketonates are often good sensitizers for Eu^{3+}. In particular:

- The diketonate-centred $\pi \rightarrow \pi^*$ transition is strong and falls in the near UV region, moreover its electric dipole moment is centred in the middle of the diketonate moiety.
- Eu^{3+} ion is commonly only 2.3–2.4 Å distant from the donor oxygen atoms.[6,[7]]
- Substituents at positions 1 or 3 can modify the absorption wavelength of the diketonate and modulate the energy of the triplet state, in order to optimize the energy levels involved in the ligand-to-metal energy transfer.

[5] It should be recalled that Ln-DOTA complexes are partially hydrated, despite the fact that the ligand is 8-dentate and the resulting complexes anionic. However, this is a function of the ionic radius of a given lanthanide.[39]

[6] Two main mechanisms describe the energy transfer: *Dexter* and *Förster resonant energy transfer* (FRET).[2] Both depend strongly on the donor-acceptor distance *R*: Dexter mechanism depends on $e^{-\alpha R}$, while FRET depends on R^{-6}.

- Chiral diketones can be easily synthesized through a Claisen type reaction from cheap natural enantiopure ketones (see Chapter 2).

Therefore, it is not surprising that many complexes with outstanding optical and chiroptical properties belong to this class: to the best of our knowledge, $Eu(TTA)_3 \cdot 2L_6$ (TTA = 2-thenoyltrifluoroacetonate, L^4; L^5 = dibenzylsulfoxide; Scheme 1-3) displays the highest quantum yield reported for a Eu^{3+} complex (85%) in solid state,[40,41] while the heterobimetallic complex $CsEu(hfbc)_4$ (hfbc = heptafluorobutyrylcamphorate, L^6; Scheme 1-3) showed a g_{PL} value of 1.38, the highest ever measured for a Ln^{3+} system.[22,42] It should also be noted that the same ligand L^6 was able to sensitize Sm^{3+}, providing another complex with excellent polarisation characteristics. For the manifold associated to the Sm^{3+} $^4G_{5/2} \rightarrow {}^6H_{5/2}$ transition, Kaizaki et al.[22] Reported g_{PL} values of −1.15 (at 553 nm), −0.35 (561 nm), +0.96 (575 nm) and −0.45 (588 nm).

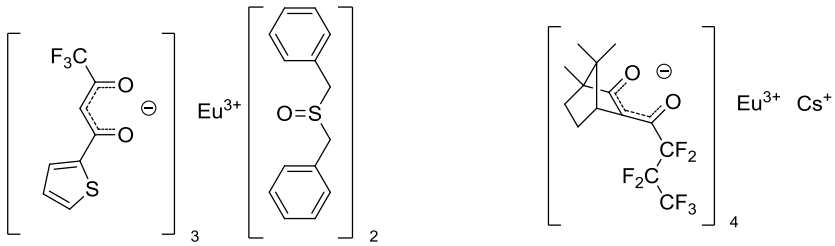

Scheme 1-3. Two Eu^{3+} complexes displaying peculiar optical ($Eu(TTA)_3 \cdot 2L_5$, quantum yield = 85 %), and chiroptical ($CsEu(hfbc)_4$, g_{PL} = 1.38) features.

Camphor-based systems

Camphor provides a rigid chiral backbone employable in the synthesis of β-diketones; aside from the exceptional performances already mentioned for $CsEu(hfbc)_4$, several other camphorate-based complexes have been investigated by CPL spectroscopists with interesting results.

Tris europium trifluoromethylcamphorate ($Eu(facam)_3$, facam = L^7; Scheme 1-4) in dimethylsulphoxide displays a g_{PL} of |0.78|[43] and it is used as a standard for

CPL instruments calibration,[44] even though this practice was recently criticized and other systems have been proposed.[45]

Recently Eu(facam)$_3$ complexes with several ancillary ligands were synthesized and their CPL measured in solution.

Harada et al.[46,47] have employed ligands with *atropos* or *tropos* axial chirality such as (*R*/*S*)-2,2'-bis(diphenylphosphoryl)-1,10-binaphthyl ((*R*/*S*)-BINAPO, (*R*/*S*)-L[9]), 2,2'-bis(diphenylphosphoryl)-1,10-biphenyl (BIPHEBO, L[10]), with central chirality as bis-(4*R*/4*S*)-(4-isopropyl-oxazolinyl)pyridine ((*R*/*S*)-^{i}Pr-Pybox, ((*R*/*S*)-L[11]), and bis-(4*S*,5*S*/4*R*,5*R*)-(4-methyl-5-phenyl-oxazolinyl)pyridine ((*S*,*S*/*R*,*R*)-Me-Ph-Pybox, (*S*,*S*/*R*,*R*)-L[12]), and achiral ligands as 1,10-phenanthroline (Phen, L[13]) and triphenylphosphine oxide (TPPO, L[14]) (Scheme 1-4). The g_{PL} values reported for the magnetic transitions in acetone-d_6 range from |0.44| to |1.0| (Table 1-2).

Changing the absolute configuration of the ancillary ligands in Eu((*R*/*S*)-BINAPO)(*D*-facam)$_3$ and Eu((*R*/*S*)-^{i}Pr-Pybox)(*D*-facam)$_3$, the g_{PL} sign remains unchanged, indicating that in these cases the CPL activity is mainly controlled by the chirality of *D*-facam ligands.

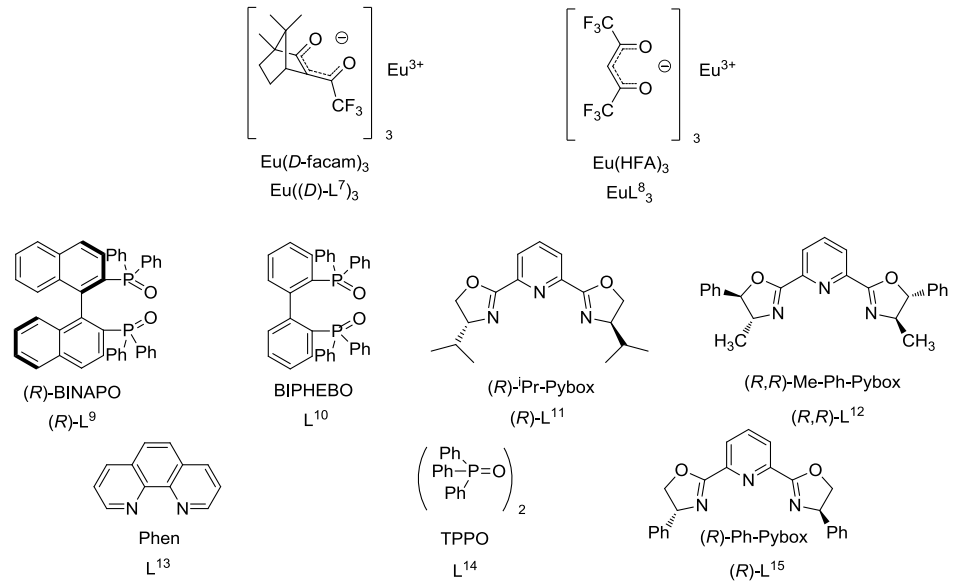

Scheme 1-4. Diketonate-based Eu^{3+} complexes and ancillary ligands reported in References [46,47].

Table 1-2. Ancillary ligands for Eu(*D*-facam)$_3$ and g_{PL} values of the resulting complexes measured in d_6-acetone[46,47] (see Scheme 1-4).

Ancillary ligand	g_{PL} **(λ=595 nm)**
(*R*)-BINAPO ((*R*)-L^9)	0.44
(*S*)-BINAPO ((*S*)-L^9)	0.34
BIPHEBO (L^{10})	0.24
(*R*)-^{i}Pr-Pybox ((*R*)-L^{11})	-1.0
(*S*)-^{i}Pr-Pybox ((*S*)-L^{11})	-0.8
(*S*,*S*)-Me-Ph-Pybox (*S*,*S*)-L^{12})	-1.0
Phen (L^{13})	-0.46
TPPO (L^{14})	0.47

Other diketonate-based chiral complexes

1,1,1,5,5,5-hexafluoropentane-2,4-dione (HFA, L^8, Scheme 1-4) is known to be a good sensitizer for Eu^{3+}. HFA has been used by Yuasa et al.[48] to synthesize a series of complexes Ln(HFA)$_3$L* (L* = L^{15}, L^{11}, L^{12}, Scheme 1-4) in which the

chiral ligand L^* induces an asymmetric arrangement of the three HFA ligands around the lanthanide.

With the reported series of Pybox ligands as L^*, they obtained high luminescence quantum yields (34–41 %) and g_{PL} values (|0.15|–|0.46|) in CD_3CN solution for Eu^{3+} complexes.

Interestingly enough, the CPL signs of the $^5D_0 \rightarrow {}^7F_1$ and $^5D_0 \rightarrow {}^7F_2$ transitions were the same for L^* = (*R*)-^{i}Pr-Pybox ((*R*)-L^{11}) and (*R*,*R*)-Me-Ph-Pybox ((*R*,*R*)-L^{12}) but they were inverted for bis-4*R*-(4-phenyl-oxazolinyl)pyridine ((*R*)-Ph-Pybox, (*R*)-L^{15}) (see Table 1-3 and Scheme 1-4).

In order to correlate the CPL spectrum signature with the complex structure, single-crystal X-ray structural analyses were performed. It was found that the ligand-ligand intramolecular interactions account for the asymmetric arrangement around the lanthanide ion, justifying the observed CPL spectrum signature. Anyway no analysis to assess the actual structure in solution neither the possible stereoisomer equilibria was carried out. However, the CD spectra measured in solution for $EuL^8{}_3L^{11}$ and $EuL^8{}_3L^{12}$ display bands with the same sign, while the sign it is inverted for $EuL^8{}_3L^{15}$, consistently with the solid state data.

It is worth noting that the CPL of $Eu(facam)_3L^{14}$ and $Eu(HFA)_3L^{15}$ has been investigated even in solid state taking the measurement on single crystals.[49]

Table 1-3. Ancillary ligands for $Eu(HFA)_3$ and g_{PL} values of the resulting complexes measured in CD_3CN[48] (see Scheme 1-4).

Ancillary ligand	g_{PL}	
	$^5D_0 \rightarrow {}^7F_1$	$^5D_0 \rightarrow {}^7F_2$
(*R*)-Ph-Pybox ((*R*)-L^{15})	0.15	-0.020
(*R*)-^{i}Pr-Pybox ((*R*)-L^{11})	-0.46	0.034
(*R*,*R*)-Me-Ph-Pybox/ ((*R*,*R*)-L^{12})	-0.35	0.026

Polynuclear systems

Recently, chiral polylanthanidic systems with large g_{PL} values have begun being synthesized.

Mamula et al.[50] reported a C_3 trinuclear complex with a chiral bipyridine–carboxylate ligand (L^{16}, Figure 1-2), formed through a completely diastereoselective self assembly process which shows also a complete chiral self-recognition in the presence of enantiomer mixtures of the ligand, yielding the system of formula $Eu_3L^{16}{}_6$. In addition ^{1}H-NMR studies showed that the gross crystal structure of the system (see Figure 1-2) is preserved in CH_2Cl_2 solution.[51] g_{PL} of |0.088| and |0.0806| were measured in CH_2Cl_2 for the $^5D_0 \rightarrow {}^7F_1$ and $^5D_4 \rightarrow {}^7F_5$ transitions of the Eu^{3+} and Tb^{3+} complexes respectively.

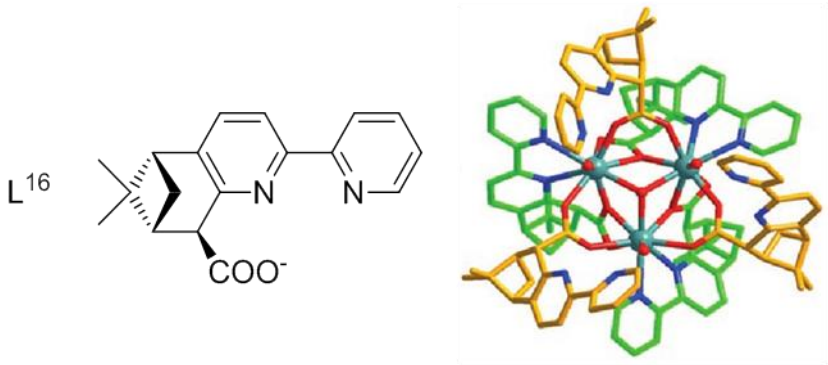

Figure 1-2. (–)-5,6-pinene-bipyridine ligand (L^{16}) and the X-ray structure of the $(EuL^{16}{}_2)_3$ complex (reproduced with permission from Ref [51]).

More recently, Mazzanti et al.[52] syntesized a Eu^{3+} complex with multilayered supramolecular architecture using (S/R)-6'-(4-phenyloxazolin-2-yl)-2,2'-bipyridine-6-carboxylate as a ligand (L^{17}, Figure 1-3) and investigated its optical properties.

Starting from a ligand of *S* (or *R*) chirality, one obtains a mixture of diastereomeric Δ and Λ complexes of $EuL^{17}{}_2$ stoichiometry with only partial selectivity ($\Lambda/\Delta \approx 1.8$, with *S* ligand). In concentrated acetonitrile solution (6 mM), complexes of formula $Eu_3L^{17}{}_6$ self-assemble with a defined helicity

(namely Δ, with *S* ligand); this system displays 25 % quantum yield with a |0.45| g_{PL} value for the $^5D_0 \rightarrow {}^7F_1$ transition.

A controlled addition of $Eu(OTf)_3$ leads to formation of an heptanuclear system displaying a 27 % quantum yield with a |0.10| g_{PL} value. This g_{PL} is lower than that measured for the trinuclear complex, in fact in the heptanuclear system, the central Eu^{3+} ion coordinates six $EuL^{17}{}_2$ units; three of them display Δ chirality, while the other three ones display Λ chirality; moreover these units come in an alternate fashion, so the intrinsic chirality of each $EuL^{17}{}_2$ is almost balanced out in the complex (Figure 1-3).

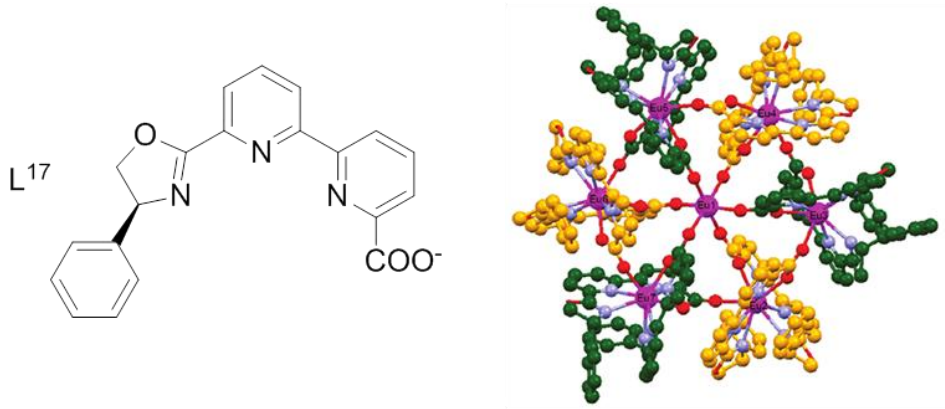

Figure 1-3. Left: (S)-6'-(4-phenyloxazolin-2-yl)-2,2'-bipyridine-6-carboxylate (L^{17}) ligand. **Right:** the XRD structure of the heptanuclear complex, where the units yellow and green represent Δ and Λ mononuclear complexes $EuL^{17}{}_2$, respectively (reproduced with permission from Ref [52]. Copyright 2012 American Chemical Society).

It is worth noting that helicates containing both Eu and Cr^{III} centres displaying g_{PL} factors around 10^{-2} (for $^5D_0 \rightarrow {}^7F_1$ transition) were reported as well.[53]

Lanthanide CPL probes for molecular sensing

Thanks to the great sensitivity of the CPL signals to conformational and structural aspects and to the peculiar optical and chiroptical properties discussed above, lanthanide complexes were employed as probes for small molecules and also proteins.

Parker et al. reported a wealth of cyclen and triazacyclenonane-based Eu^{3+} and Tb^{3+} complexes[10,54-56] (Scheme 1-1).

Lanthanide CPL and organic molecules

Dynamically racemic complexes. Tb^{3+} *tris* 2,6-pyridine-dicarboxylate (L^{18}) and chelidamic acid (L^{19}) (Scheme 1-5) D_3 racemic complexes can interact with non racemic compounds, giving rise to CPL.[52,53] Recently, they have been employed by Muller et al.[57] as probes for aminoacids. These are in fact chiral D_3 complexes, but Λ and Δ enantiomers undergo a rapid equilibrium in solution and can not be resolved.

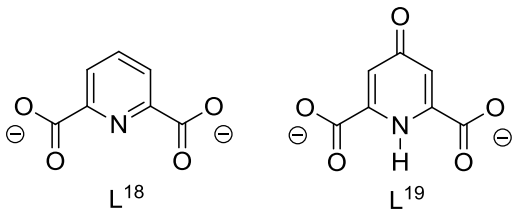

Scheme 1-5. 2,6-pyridine-dicarboxylate (L^{18}) and chelidamic acid (L^{19}).

When they interact with enantiopure aminoacids, thanks to their ability to form a hydrogen-bond network, one form prevails over the other one, since they are now in a diastereomeric relationship (*Pfeiffer effect)*.[58,59] This event is signalled by the rising of an induced CPL signal in the region of the $^5D_4 \rightarrow {}^7F_5$ transition.

With a similar approach, Parker et al. synthesized a cyclen-based Eu^{3+} (EuL^{20}) complex in which the chirality of the complex is defined by the position of the azaxanthone and carboxylate pendant arms but it is dynamically racemic and of course no CPL can be detected (Figure 1-4).[54,60]

When α_1-acid glycoprotein (α_1-AGP) is added, EuL^{20} shows optical activity and a CPL signal is switched on. The complex is coordinatively unsaturated and a weakly coordinated axial water molecule is needed to fill the coordination sphere.

The α_1-AGP displaces the axial ligand and, at the same time, it perturbs the racemic equilibrium towards one of the two conformational enantiomers, as signalled by the change of the total emission spectrum and mainly by the appearance of a strong CPL signal (Figure 1-4).

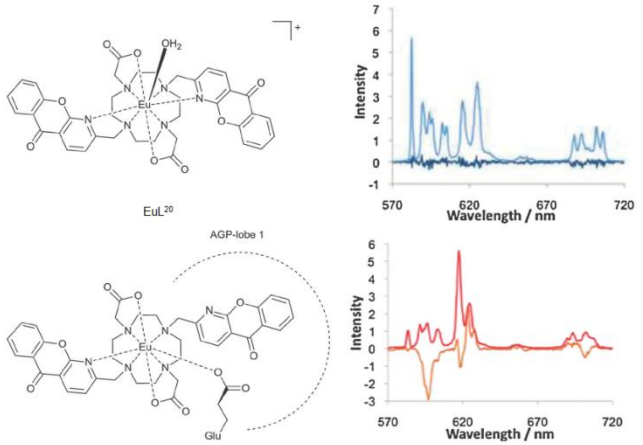

Figure 1-4. Binding between the EuL^{20} and α_1-AGP. On the right: CPL (blue navy and orange) and total luminescence (light blue and red) for free and bound forms (reproduced from Ref [54] with permission of The Royal Chemical Society).

In particular the g_{PL} factor of the $^5D_0 \rightarrow {}^7F_1$ transition increases upon adding the protein, allowing one to estimate a binding constant for the system formed by EuL^{20} and α_1-AGP.

Given the selectivity of the CPL response to α_1-AGP, this one and similar systems pave the way to the development of an analytical method to track this protein: the importance of monitoring α_1-AGP levels in serum has been recently recognized, because it increases as a response to an inflammatory acute state and can be used as a biomarker for breast cancer.

Enantiopure complexes Enantiopure complexes are endowed with intrinsic CPL, which can be modified in both intensity and shape after the interaction with a target molecule.

The CPL signal accompanies total luminescence and provides additional information, since the shape and signature of the CPL spectrum is very sensitive to the coordination environment and thus the signal may be very specific for a certain target.

Parker et al. reported Tb^{3+} and Eu^{3+} enantiopure cyclen-based systems as CPL probes for proteins:[10] Figure 1-5 shows the Tb^{3+} macrocyclic complex TbL^{21} employed for serum albumin sensing.[61]

The complex bears three asymmetric carbon atoms on the side-arms and it exists as diastereomer pair: *SSS*-Δ-[TbL^{21}] and *SSS*-Λ-[TbL^{21}] with the former being prevailing in solution.

Serum albumin binds to *SSS*-Δ-[TbL^{21}] (and only more weakly to its enantiomer), and as a consequence to the formation of this adduct, the preferred helicity of TbL^{21} is reversed from Δ to Λ and a switching of the CPL spectrum signature is observed.[62]

This switching occurs selectively with serum albumin while it does not with other proteins, cyclodextrins or chiral anions. This led Parker et al. to envisage a potential use for these complexes as a probe for circularly polarized luminescence microscopy.[10]

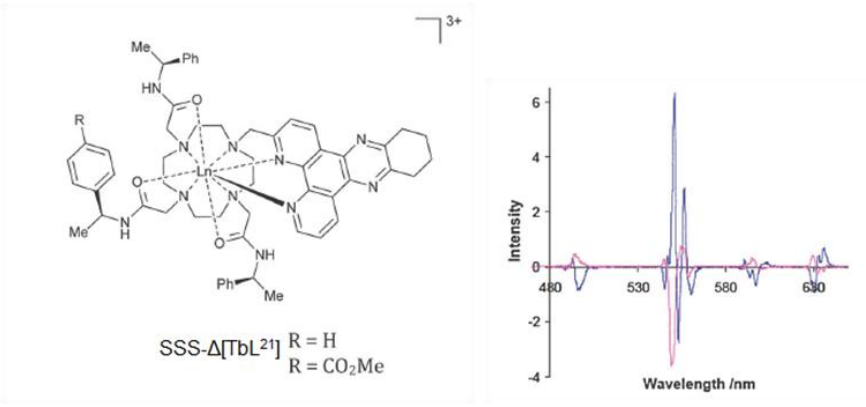

Figure 1-5. Lanthanide macrocyclic complex (TbL_{21}) and CPL spectrum before (blue) and after (purple) addition of serum albumin (reproduced with permission from Ref [10]. Copyright 2009 American Chemical Society).

The sensitive nature of the lanthanide-centred CPL has been further demonstrated by Yuasa et al.[63] A 1-biphenyl-3-perfluoroethyldiketonate moiety was covalently bound to bovine serum albumin or other proteins, such as *Staphylococcus aureus* recombinant nuclease A and insulin. This diketonate has a strong affinity for lanthanides and is a good sensitizer for Eu^{3+}; in fact, by complexing these systems with Eu^{3+}, the protein fills the coordination sphere around the lanthanide as a function of its structural and chemical characteristics, in addition, it provides an asymmetric environment allowing one to record different Eu^{3+}-centred CPL spectra (Figure 1-6).

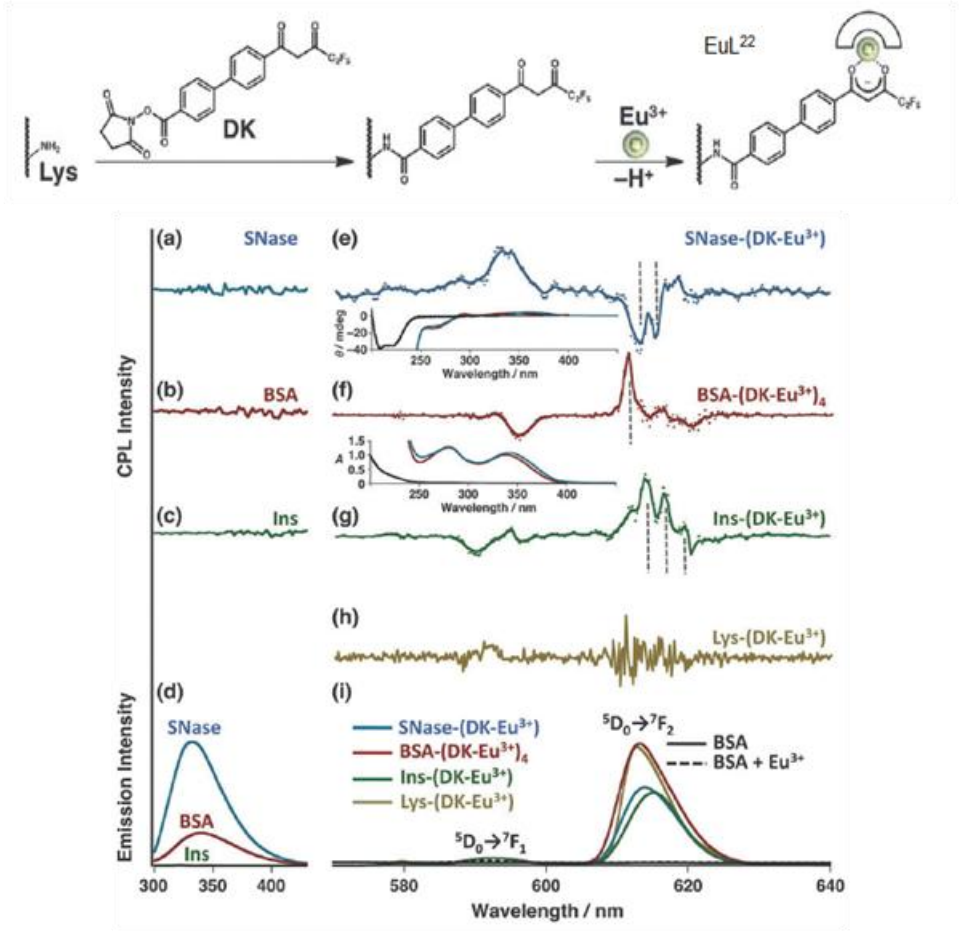

Figure 1-6. Covalent binding of 1-biphenyl-3-perfluoroethyldiketonate to the protein and complexation with Eu^{3+} and Eu-centred CPL of various adducts (reproduced from Ref [63] with permission of The Royal Chemical Society).

Lanthanide CPL and ion binding

Lanthanides display strong affinity for hard anions, which are able to displace weak neutral ligands. Moreover it is possible to tune the coordination strength of acidic ligands as a function of pH and the pK_a of the ligand itself. A variable coordination may modulate the coordination geometry to which CPL is sensitive.

Eu^{3+} complexes have been used as probes for bicarbonate or pH.[54,64] Various enantiopure cyclen-based structures have been developed as responsive systems in which the concentration of bicarbonate can be tracked following the variation of the luminescence dissymmetry factor for a selected transition.

Complex EuL^{23}, bearing a sulfonamide moiety on one arm proved to be pH-responsive: when pH increases the sulfonamide moiety is deprotonated and thus it is able to coordinate the metal centre; this results in a rigidification of the complex leading to an increase in g_{PL} values at 632 nm (Figure 1-7).

According to Parker et al.,[54] it is also possible that the coordination changes the geometry around the lanthanide providing a twist angle closer to the ideal one for static coupling mechanism (namely 22.5°) (see Section below).

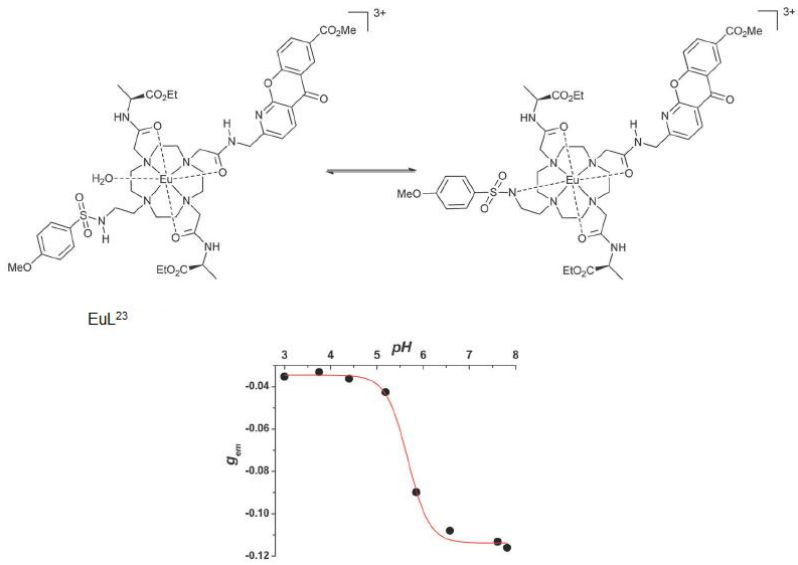

Figure 1-7. Top: changes in the coordination sphere of EuL^{23} as a response to increasing pH. Bottom: g_{lum} for the transition at 632 nm as a function of pH (reproduced from Ref [54] with permission of The Royal Chemical Society).

Origin of strong CPL

Any chiroptical activity requires a non-vanishing rotational strength:

$$R_{ij} = \Im\,[\langle i|\hat{\boldsymbol{\mu}}|j\rangle \cdot \langle j|\hat{\mathbf{m}}|i\rangle] = \Im[\boldsymbol{\mu}_{ij} \cdot \mathbf{m}_{ji}] \qquad (1\text{-}3)$$

where $\hat{\boldsymbol{\mu}}$ and $\hat{\mathbf{m}}$ are the electric and magnetic dipole transition operators and $\Im$ is the imaginary part of the following expression. In an emission process the energy of the initial state *i* is higher than that of the final state *j*; in this case Eq. (1-3) gauges CPL.

For a magnetic dipole allowed-electric dipole forbidden transition, like a Ln-centred *f*–*f* transition, $\boldsymbol{\mu}_{ij} \approx 0$[7] is expected and therefore a vanishing rotational strength. The process giving rise to CPL activity can be conveniently represented with reference to two limiting mechanisms: *static* and *dynamic coupling*.[23] The former is the only possibly relevant one when the ligand lacks any significant chromophoric group; in all the other cases both mechanisms should be taken carefully into account.

Static coupling

In a dissymmetric environment, a mixing of e. g. *4f* and *5d* orbitals may provide the necessary odd-parity interconfigurational character yielding $\boldsymbol{\mu}_{ij} \neq 0$.[23,65] This can happen only if the first coordination sphere is chiral and therefore the covalent contribution to the bonds between the lanthanide and the donor atoms entails invoking such hybrids.

In the typical parlance of the chiroptical spectroscopies, and in particular in ECD, this case can be described as an intrinsically chiral chromophore.

[7] We recall that $\boldsymbol{\mu}_{ij}$ is exactly 0 only in a centro-symmetric environment, however even for chiral molecules it is generally very small.

In the limit of low covalence, the coordination neighborhood causes only a weak perturbation to the metal states, so the sum rule can apply yielding a vanishing integral of the CD or CPL spectrum over all the *f* transitions. This is hardly of practical aid when we dealing with a complex of Eu^{3+}, Tb^{3+} or other visible-emissive lanthanides, because their transitions range from IR to UV region and many of them will almost surely be covered by ligand-centred bands.

Yb^{3+} and Ce^{3+} represent a special case: since they have a $4f^1$ and $4f^{13}$ electronic configuration respectively, they behave as monoelectronic systems with only two levels each. In particular, while Ce^{3+} $^2F_{7/2} \rightarrow {}^2F_{5/2}$ transition falls in the IR region and may be covered by ligand vibrational CD signals, Yb^{3+} $^2F_{7/2} \rightarrow {}^2F_{5/2}$ falls in the NIR region and can thus be often easily recorded without significant interferences.[34,66] In the limit of perfect static coupling the integral over the manifold corresponding to the M_J splitting allied with this transition is expected to vanish.

This result can be transferred to isostructural complexes of other lanthanides. Lanthanide complexes often show isostructurality along the series; this means that the geometry of the system may show no significant dependence on the lanthanide ion.[8]

For this mechanism, in the common case of a distorted square antiprismatic geometry, as found for example in DOTA-like complexes or in *tetrakis* diketonates (notably in the case of $CsEuL^6_4$) the CPL signal should vary with the *twist angle* φ following a $\sin(4\varphi)$ trend, so the maximum is reached for $\varphi = 22.5°$ (Figure 1-8).[68]

[8] Ligand-centred ECD spectra of isostructural compounds do not display significant variations. A non-chiroptical method to asses isostructurality is through analysis of the NMR data (see Chapter 2); in fact paramagnetic shifts and relaxation rates of paramagnetic Ln^{3+} compounds contain geometric information. For details we refer to the specific literature.[66,67]

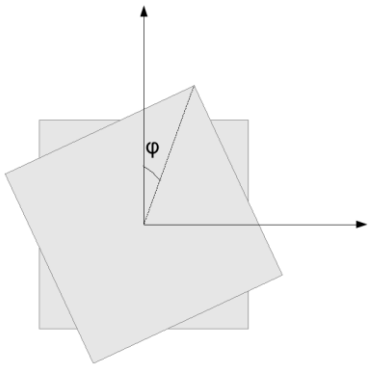

Figure 1-8. Twist angle φ in the case of a distorted square antiprismatic geometry.

Dynamic coupling

When the coordination polyhedron is itself achiral, the ligand field should allow only *f*→*f* electronic transitions with pure magnetic dipole character. Once more, making reference to common nomenclature in ECD theory, we deal with an intrinsically achiral chromophore. Optical activity can stem from some coupling interaction between metal-centred transitions and the dissymmetric environment provided by the ligands beyond the first coordination sphere.

The previously cited $CsEu(hfbc)_4$ (Scheme 1-3) complex provides an interesting example to analyze.

$CsEu(hfbc)_4$ has an almost perfect antiprismatic geometry in solution with a twist angle of 41.4°, thus static coupling mechanism alone can not account for the measured g_{PL}=1.38 value at 598 nm,[69] i.e. for the $^5D_0 \rightarrow {}^7F_1$ transition, which has magnetic dipole but no electric dipole character. Indeed, in an ideal antiprismatic geometry the twist angle is 45°, which means that the coordination polyhedron is completely symmetric with respect to rotation-reflection operations.

On the other hand, dynamic coupling between the Eu-centred and the nearby diketonate $\pi \rightarrow \pi^*$ transitions may help us rationalising this case.

Figure 1-9 represents two of the 4 β-diketonate moieties of the $CsEu(hfbc)_4$ complex (belonging to C_4 point group).

The lanthanide-centred $^5D_0 \rightarrow {}^7F_1$ magnetic transition ($\mathbf{m}_{Ln}$) is associated with electric quadrupole moment; the nearby diketonate groups constitute polarisable linear oscillators ($\boldsymbol{\mu}_{lig}$), which can be excited (through dipole-quadrupole interaction) when the $^5D_0 \rightarrow {}^7F_1$ transition is active, providing a **m-μ** coupling mechanism.[70]

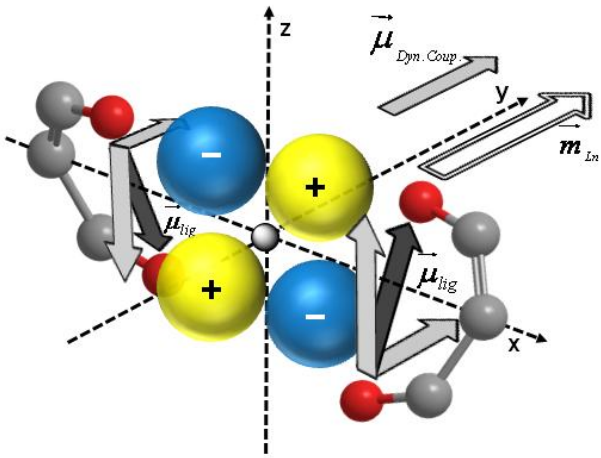

Figure 1-9. Dynamic coupling mechanism occurring in a C4–symmetric Ln diketonate: for simplicity, only two β-diketonate moieties are depicted. The four lobes represent the quadrupolar charge distribution (blue and yellow) allied to the magnetic dipole transition (with moment $\mathbf{m}_{Ln}$, along the y-axis). This induces a polarisation of the diketonate group, which is represented by the two skew $\boldsymbol{\mu}_{lig}$ vectors. The horizontal components of $\boldsymbol{\mu}_{lig}$ provide non vanishing terms to the scalar product $\mathbf{m}\cdot\boldsymbol{\mu}$. (Adapted from Ref [71]).

With reference to Figure 1-9, the lanthanide-centred magnetic moment $\mathbf{m}_{Ln}$ (belonging to irrep *E* of the C_4 point group) is contained in the *x*-*y* plane, orthogonal to the C_4 (*z*-axis). For the sake of simplicity, in Figure 1-9 we represented only its *y*-component. The associated quadrupolar charge distribution during this Ln-centered transition is shown as well.

Each diketonate can be depicted as a linear polarizable group, directed parallel to the vector joining the two oxygen atoms, that is, oblique with respect to the *xy*-plane. When the Ln-centred transition is excited (either in absorption or in emission), its associated electric quadrupole induces a simultaneous electric

dipole moment $\boldsymbol{\mu}_{lig}$ on each diketonate. In turn, these 4 electric dipoles couple with one another providing components with different symmetry: either belonging to *A*-irrep, *i.e.* oriented along *z*, or doubly degenerate (*E*) in the *x*-*y* plane.

Only this latter (low energy) *E* component of the $\boldsymbol{\mu}_{lig}$-$\boldsymbol{\mu}_{lig}$ coupling ($\boldsymbol{\mu}_{Dyn.Coup}$) can constructively interact with the $\mathbf{m}_{Ln}$ to provide rotational strength (consisting in the scalar product $\mathbf{m}\cdot\boldsymbol{\mu}$). On the contrary, the axial *A*-counterpart leads to cancellation.

Dynamic coupling mechanism can only be efficient when the lanthanide and the chromophoric group are spatially close, since the dipole-quadrupole interaction depends on the Ln-$\boldsymbol{\mu}_{lig}$ distance as R^{-4}; moreover it depends on the difference between the frequencies of the lanthanide-centred and the ligand-centred transitions; this dependence can be accounted for as a perturbation. When these conditions are fulfilled, this mechanism can provide transitions with a strong circular polarization, if compared with the simple static coupling; in fact dynamic coupling does not entail invoking Ln orbital hybridation, which is generally small, since the covalency is low in the Ln-ligand bond.

When this mechanism is active, $f \rightarrow f$ transitions can no longer be considered isolated, because it is naturally coupled with ligand-centred transition(s); so, unlike the case of static coupling, the integral over the bands of the NIR-CD spectrum of an Yb^{3+} isostructural complex will be non-vanishing.

Measurement of CPL spectra

CPL spectra are usually measured through a continuous wave scan[43] whose most significant parameters are the passing band *w*, the time constant *k* and the scan-speed *v*; they all display critical aspects, when dealing with Ln complexes.[72]

A general rule among spectroscopists states that these parameters must fulfil the condition:

$$\frac{1}{2}w > k \cdot v \qquad (1\text{-}4)$$

Particular caution should be taken in setting the passing band width; in fact, as stated above, lanthanide emission bands can be very narrow (less than 5 nm), and they are often multiplets with nearby bands, with possibly opposite CPL signs; if this components remain unresolved, they will cancel out (at least partially), causing error in the assessment of the intensity of the CPL signal and in the calculation of the g_{PL} value.

With a passing band of 1 nm and a time constant of 1 sec, the scan-speed should be set to 0.5 nm/sec. As an example we note that it will take 4 min for each scan to acquire a 120 nm region: this may be typical when dealing with Eu^{3+} complexes.

A low enough scan-speed is also necessary to accurately detect the emission maxima of the narrow CPL lines, which in turn is necessary to extract accurate g_{PL} values.

Lanthanide CPL spectra are usually recorded with a 90° geometry between the source and the detector, as in an ordinary fluorescence experiment. On the other hand, if it is an issue, their large Stokes shift would allow one to adopt an in-line geometry. To this end, one must prevent the exciter beam to reach the detector, which may be achieved by simply adding a low-pass filter after the sample. When using a diffraction-grate monochromator, one must be aware that higher harmonics of the exciting radiation may fall in the emission region.[9]

Moreover, the large luminescence dissymmetry factors usually obtained for lanthanides, may allow one to measure lanthanide CPL spectra using simple static optics, employing a quarter wave retarder and a linear polarizer. Early measurements in the field of CPL were made with similar devices without photoelastic modulators, which are now common in CPL spectrophotometers (see Chapter 9).[72]

[9] For example setting the excitation to 305 nm, it may interfere with the 610 nm band of an Eu^{3+} complex.

This setup allowed Oosterhoof et al. to measure g_{PL} values with a standard deviation within 0.005 and 0.01.[73-75]

Plotting g_{PL} vs. λ

In a CPL measurement ΔI and I are not absolute quantities, in fact, as in ordinary fluorescence experiments, not all of the emitted light is detected, depending on the experimental conditions. On the other hand, the luminescence dissymmetry factor, as defined in Eq. (1-1), is an absolute value. Therefore there are good physical reasons to discuss and report CPL spectra also in terms of g_{PL}, not only of individual bands but also as a continuous function of wavelength (or wavenumber).

However some precautions should be taken when plotting $g_{PL}(\lambda)$. Indeed, out of the emission zones, I and ΔI are equal to 0, thus g_{PL} gives rise to a mathematically undefined form: the practical result is an amplification of the instrumental fluctuations around zero emission,[10] with erratic and possibly very large values of *g*, where one would actually expect 0. This may be quite a serious issue with lanthanides, since the emission bands are very narrow and commonly without relevant tailing. Moreover, such narrow bands are commonly instrumentally traced with very few data points, therefore trying to eliminate the noise through smoothing algorithms is a risky choice, in fact in this way a faithful reproduction of the profile of these bands can be hard to achieve.

We therefore suggest to introduce a trivial mathematical artifice defining a *corrected* g_{PL} as:

$$\tilde{g} = \frac{\Delta I}{I+\delta} \qquad (1\text{-}5)$$

where the correcting constant δ has to be chosen bigger than the instrumental noise but negligible with respect to the smallest emission signal one wants to measure (for example, 1/100 of I).

[10] This noise comes from the definition of g_{PL} itself and not directly from the experimental measurement.

As an example, in Figure 1-10 we show a plot of g_{PL} (without correction) and $\tilde{g}_{PL}$ ($\delta = 3 \cdot 10^{-4}$, i.e. 2/100 of the maximum intensity of the band at 585 nm) for a CPL spectrum obtained for $CsEu(hfbc)_4$.

For instance, considering the 550–570 nm region, one can see that the correction is sufficient to smooth the baseline while not large enough to significantly affect the signal bands (Insets of Figure 1-10).

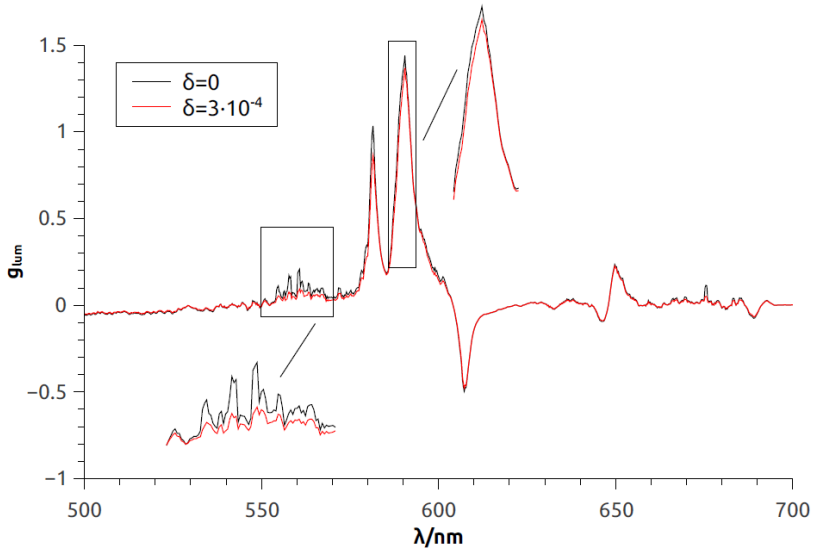

Figure 1-10. Plot of g_{PL} with (red) and without correction (black) for $CsEu(hfbc)_4$. Notice that the baseline is naturally smoothed while the bands are not affected by the correction (insets).

Conclusions

Chemists may design and synthesise new ligands in order to optimise the desirable properties of the final lanthanide complex (see Chapter 2). In particular an optimal ligand should:

- form a stable/inert lanthanide complex;
- be a good sensitiser for a given lanthanide;
- form a complex with a chiral geometry that can give rise to a strong CPL, according to the mechanisms described herein;

- form a complex with good solubility in the intended solvent or medium.

Lanthanide peculiar spectroscopic features (large ligand-induced Stokes shift, narrow and characteristic emission bands), joined with their outstanding circularly luminescence properties can give rise to a multidisciplinary interest. The selectivity of the CPL response is employed as a bioanalytical method to quantify and track biomarkers, and more specific tools, as circularly polarised microscopy, can be developed using tailored lanthanide complexes.

Other applications, in which luminescent lanthanide complexes are already employed, can be extended using chiral analogues with strong circularly polarised emission, such as electroluminescent circularly polarized light emitters (see Chapter 3 and 4).[76,77]

Chapter 2

A new lanthanide complex for CPL

Introduction

As seen in the previous Chapter, the ligand has two primary functions: **1)** to chelate the Ln^{3+}, making it soluble and stable in the desired environment; **2)** to provide the so-called antenna effect, i.e. to capture excitation (for example absorbing high energy light) and pass it onto the Ln^{3+}, which thereupon emits a photon. As a further bonus, the ligand lends itself to a huge amount of manipulations and decorations, typical of organic chemistry, and thus modulate chemical, optical, and electronic properties of the complex.[8]

In the work presented in this Chapter, we addressed two main issues: **1)** we wanted to push the excitation wavelength toward visible light, in order to avoid undesirable (far)-UV irradiation; **2)** we sought highly circularly polarized luminescence in term of g_{PL}.

Feature **1)** is desirable, because typical excitation wavelengths are 330 nm or below, which is hard on eyes and skin and induces serious damage to tissues (limiting *in vivo* imaging applications). In any case the extremely large shift between absorption and emission wavelengths of Ln complexes ensures that there would be no interference between absorption and emission processes. Feature **2)** will respond to a need of encoding information in the form of light polarization which may find application e.g. for the development of 3D-displays,[78,79] for open-space communications, or for anti-counterfeiting labelling systems. As discussed in the previous Chapter, lanthanide chiral complexes have proven ideal candidates as emitters of circularly polarized light, since they can often attain g_{PL} 2−3 order of magnitude higher than the ones obtained with purely organic molecules.[20,80,81]

With this in mind, we chose carvone, a commercially available chiral α,β-unsaturated ketone which naturally occurs in both enantiomers. A Claisen reaction with ethyl perfluorobutyrate as the partner yielded a β-diketone. In order to assess the suitability of the product for most practical applications, it is necessary to test its CPL in the solid state. This kind of measurements is still uncommon, maybe due to the fact that special experimental care should be taken to avoid the occurrence of artifacts.[31,72,82]

Results

The ligand heptafluorobutyrylcarvone[83] (hfbcvH) was readily synthesized, acylating the carvone enolate with ethyl heptafluorobutyrate (see Scheme 2-1).[11] It is noteworthy that λ_{max} for the lowest lying transition of the anion is 370 nm, some 40 nm red-shifted compared to common diketonates.[22,41]

At first, for the metalation, we employed a biphasic system using triethylamine as the base and $LnCl_3$;[84] unfortunately these conditions yielded a mixture of two lanthanide adducts (see below), while we observed a certain decomposition of the ligand to yield back carvone and heptafluorobutyrate, due to a retro-Claisen process. Using instead a stoichiometric quantity of Cs_2CO_3 as the base in anhydrous acetonitrile (Scheme 2-1), ^{1}H-NMR demonstrated the presence of one paramagnetic compound, although in presence of a small quantity of unreacted ligand. These anhydrous conditions prevented the retro-Claisen decomposition. Upon complexation, the $\pi \rightarrow \pi^*$ diketonate band undergoes a blue shift of about 15 nm (see Appendix A, Figure A2-1). Using Na^+ and K^+ carbonates, the reactions were sluggish and were discarded. The main reason of this drawback can be ascribed to the poor solubility of sodium and potassium carbonates in organic media compared to Cs_2CO_3. Before discussing the nature of the Ln^{3+} species formed, we shall describe the foremost optical properties of the Eu-derivative, which were the target of our investigation.

[11] hfbcvH was already reported in reference [83] to be employed as the stationary phase in a column for chiral chromatography, however the authors do not report any detailed characterization.

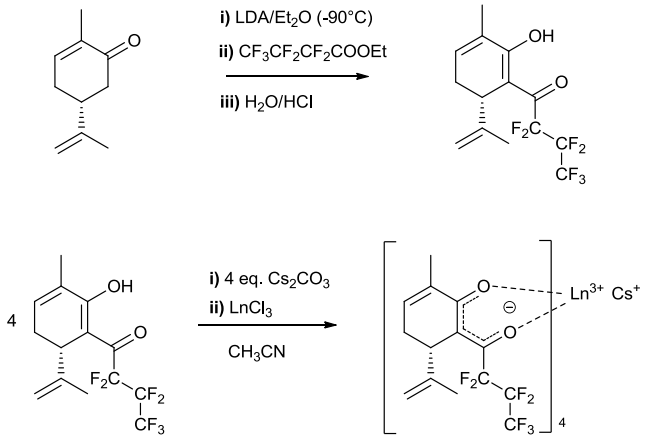

Scheme 2-1. Synthesis of heptafluorobutyrylcarvone (hfbcvH) and $Cs[Ln(hfbcv)_4]$ complexes.

Figure 2-1 displays the emission in acetonitrile solution (top) and of a quartz window deposition (bottom).

Identity of the emission spectra of solution and deposition is the first hint that the emitting species must the similar in both states.

Excitation spectrum (Figure 2-2) shows that, although maximum excitation is obtained with λ_{exc} = 370 nm, much longer wavelengths would profitably be used, possibly extending to 420 nm.

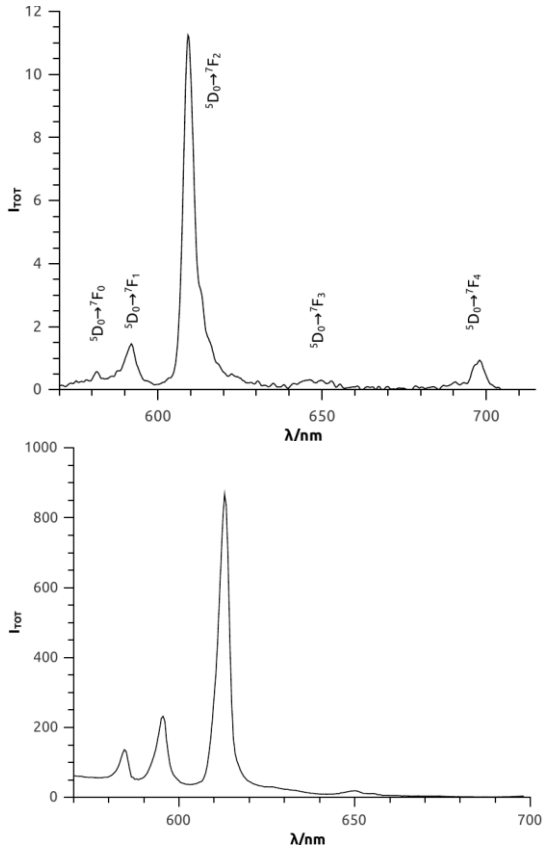

Figure 2-1. Top: Emission spectrum of Cs[Eu(*(R)*-hfbcv)$_4$] in CH_3CN solution, **Bottom:** on a quartz plate deposition (λ_{exc}=370 nm).

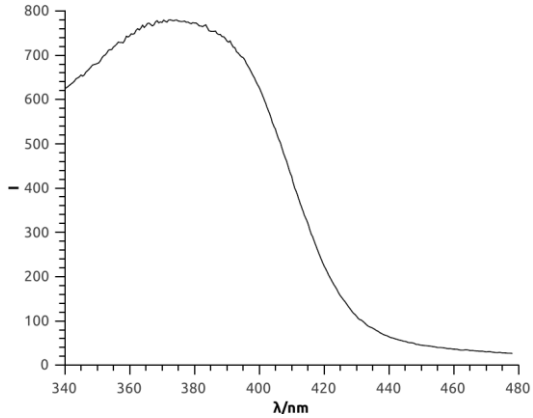

Figure 2-2. Excitation spectrum of Cs[Eu(*(R)*-hfbcv)$_4$] on a quartz plate deposition (λ_{em} = 612 nm).

A further evidence is given by the similarity of circular dichroism (CD) spectra (Figure 2-3) taken on the CH_3CN solution and on a quartz deposition. This indicates that the arrangement of ligands is not particularly different in the two media.[48]

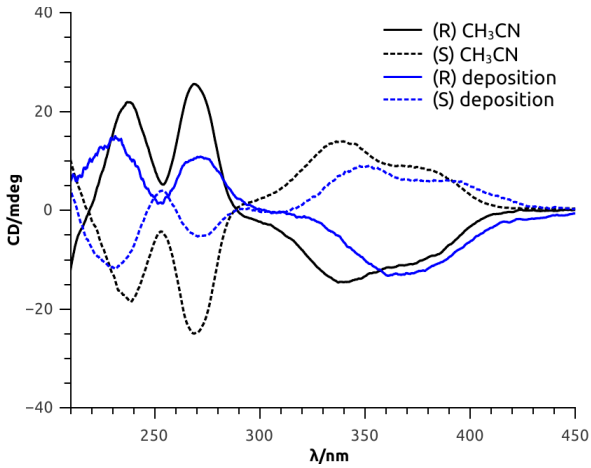

Figure 2-3. CD spectra of the two enantiomers of $Cs[Eu(hfbcv)_4]$ (R/S dashed/continuous lines) in CH_3CN solution (black) and on quartz plate depositions (blue).

The CPL spectrum of the acetonitrile solution is depicted in Figure 2-4. We may observe that for the two enantiomers of the ligand the spectra are mirror images, as expected, and we should also mention that the CPL data are completely consistent and reproducible from one sample to the next, also starting from completely new preparations of the ligand. The magnetically-allowed transition $^5D_0 \rightarrow {}^7F_1$ at about 594 nm displays the respectable *g*-value of 0.15. As it often occurs in chiral diketonates, it has a rotational strength almost equal and opposite to the one of $^5D_0 \rightarrow {}^7F_2$ around 612 nm. Because this has electric-dipole character, it is associated with a strong luminescence and it is indeed the most prominent feature of the total emission spectrum. Accordingly, its *g*-value is much smaller.

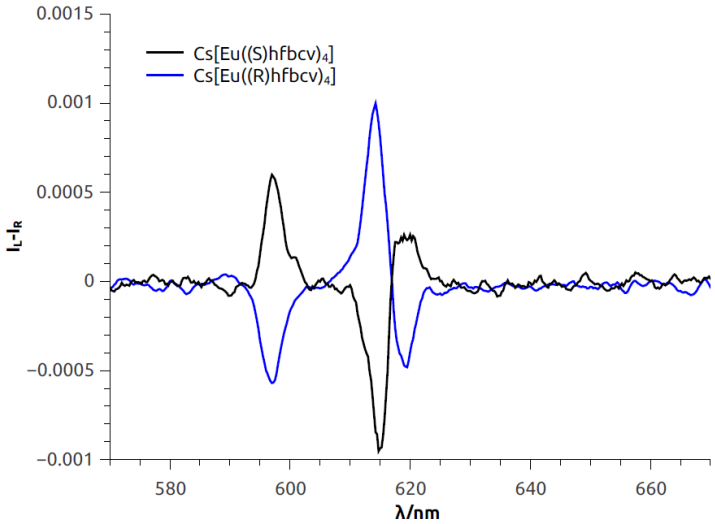

Figure 2-4. CPL spectra of the two enantiomers of Cs[Eu(hfbcv)$_4$] in CH_3CN solution (λ_{exc} = 370 nm).

Much more interesting features were found when we switched to the solid state (deposition of a few drops of the CH_3CN solution followed by slow solvent evaporation). In this case, we find the CPL spectrum of Figure 2-6, which displays much stronger signals. In this case, the *g*-value at 594 nm reaches 0.82 (Figure 2-5). To the very best of our knowledge, this value is one of the highest ever recorded[19,20,42] and one of the first reports of outstanding CPL properties of chiral lanthanide complexes in solid state.

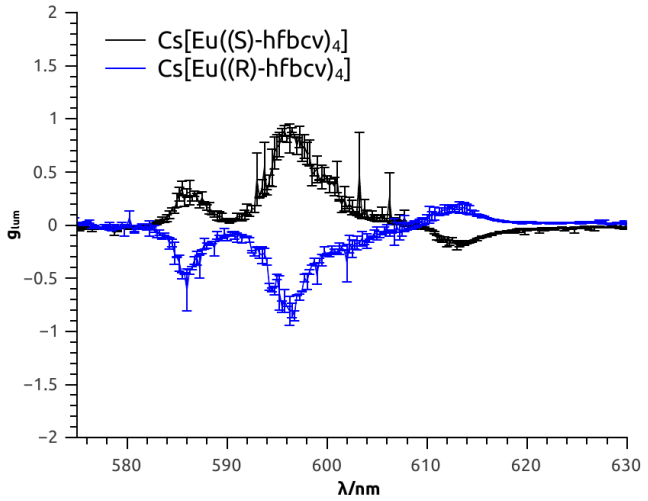

Figure 2-5. Average values of g_{PL} on three independent measurements as a function of wavelength for the two enantiomers of Cs[Eu(hfbcv)$_4$] complexes on quartz plate.

depositions. The bars represent one standard deviation (λ_{exc} = 370 nm).

The reproducibility of the data over several depositions, starting from different preparations of the complexes (Figure 2-5), the absence of fluorescence linear anisotropy signals and above all the almost perfect mirror-image CPL of the two enantiomers rule out the occurrence of artifacts (Figure 2-6). We notice that the solid state luminescence is enhanced with respect to the solution one, this is in agreement with previous observations,[41] although no ultimate explanation has been put forward. Possibly, crystal packing on one hand and solvation on the other may account for both total luminescence and CPL enhancement in solid state samples.[85]

The $^5D_0 \rightarrow {}^7F_0$ transition at 583 nm is a single sharp band, in both solution and solid state, this is consistent with the presence of only one Eu species in both cases.

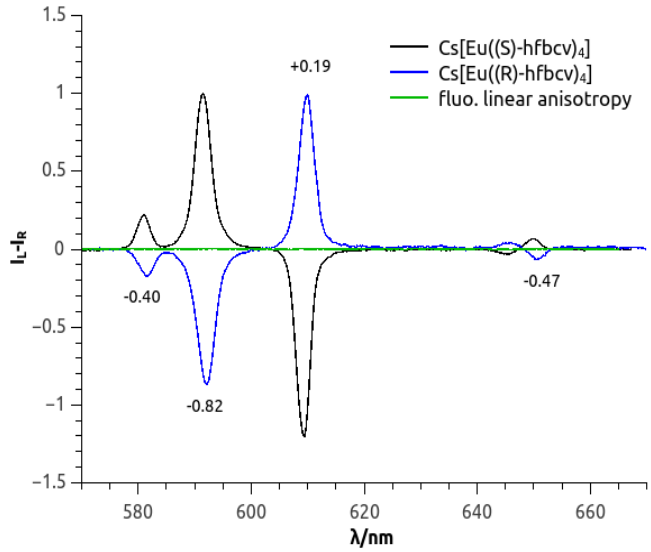

Figure 2-6. CPL spectra of Cs[Eu(*(S)*-hfbcv)$_4$] (black) and Cs[Eu(*(R)*--hfbcv)$_4$] (blue) on a quartz plate upon irradiation at 370 nm, with calculated g_{PL} values and fluorescence linear anisotropies (green).

The promising features of the CPL make us prospect immediate applications: in the first place, one can envisage a security ink which can emit red circularly polarized light under blue-light illumination, secondly, we may wonder whether

the ease of excitation of the ligand will have consequences in electroluminescence, as it does with photoexcitation, and therefore its effect in circularly polarized light emitting diodes (Chapter 3 and 4).[76] For these reasons, we attempted by all means to isolate the active species, which unfortunately resulted elusive. This is possibly due to the unavoidable presence of residual ligand. Willing to get as much information as possible on the active species and given our ability to solve solution structures based on paramagnetic NMR,[66,67] we addressed the following questions: **1)** what is the CPL-active species; **2)** determine its solution structure; **3)** what other species are present, possibly in equilibrium with the most abundant one.

In order to characterize the product that we obtained and to give an answer to point **3**, we acquired MALDI-TOF mass spectra of $Cs[Eu(hfbcv)_4]$, in CH_2Cl_2 solution in both positive (Figure A2-7) and in negative (Figure A2-8) mode. The positive MALDI-TOF (Figure A2-7) shows a peak at m/z 1666.5, attributed to the $Cs[Eu(hfbcv)_4]$ (detected as $[M]H^+$) species. The low quality of the spectrum was due to a low ion efficiency of the analyzed molecular systems. On the other hand, the presence of the *tetrakis* compound ($[Eu(hfbcv)_4]^-$) is much better appreciated by negative MALDI-TOF spectrum (Figure A2-8) which displays an intense peak at m/z 1532.6. This peak is ascribed to the anionic species resulting from the cation (Cs^+) loss from $Cs[Eu(hfbcv)_4]$ during the MALDI desorption process. The inset of Figure A2-8 provides a comparison between the experimental isotopic cluster peaks at m/z 1532.6 with the expected simulated isotopic distribution for $[Eu(hfbcv)_4]^-$. The same spectrum shows also a signal at m/z 1187.3 and a less intense peak at m/z 345.5 attributed to $Eu(hfbcv)_3$ and to the free ligand $hfbcv^-$ respectively.

The ^{1}H-NMR spectra of all synthesized $Cs[Ln(hfbcv)_4]$ complexes (Ln= Ce, Pr, Nd, Eu, Tb) in CD_3CN solution showed only one set of paramagnetically shifted proton resonances, compatible with the hfbcv resonances, indicating that the only paramagnetic species present has a C_4 symmetry. The narrow lines suggested that the complexes do not undergo conformational rearrangements in slow or

intermediate exchange regime on the NMR time scale under the investigated conditions.[66]

We assigned the NMR spectra through homo- and heterocorrelation experiments and we extracted the pseudocontact shifts (see Table A2-1, A2-2, Figure A2-4, A2-5). The analysis of these shifts indicates isostructurality along the investigated portion of the series (Figure A2-2).

Taking advantage of the structural information contained in pseudocontact shifts, we were able to asses a structure for Cs[Ln(hfbcv)$_4$] compounds in acetonitrile solution (Figure 2-7), using the routine PERSEUS (see also Appendix A),[66,86] starting from a DFT level pre-optimized ligand structure and imposing a C_4 symmetry for consistency with experimental data. Beside ^{1}H shifts, we included in the calculation pseudocontact ^{13}C shifts, relaxation rates and an estimated Ln−O distance (2.4 Å),[7] as additional boundaries. The dihedral angle between the ring and the isopropenyl group remained unchanged with respect to the DFT structure of the ligand used as the input of PERSEUS.

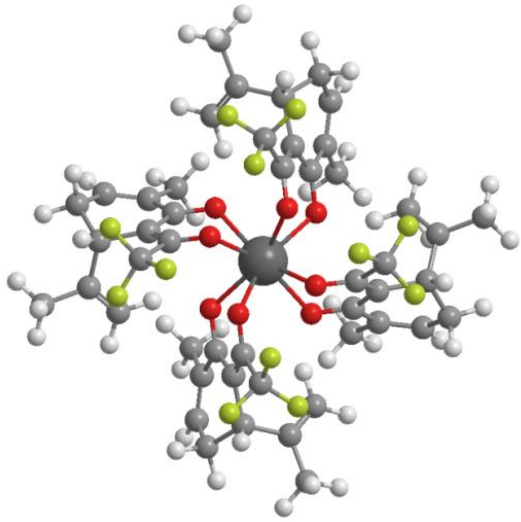

Figure 2-7. Solution (CD_3CN) structure of Cs[Ln(*(R)*-hfbcv)$_4$] obtained from PERSEUS. Since the perfluoropropyl chains could not be included in the calculation, they are here represented as trifluoromethyl groups for visual purpose only.

The PERSEUS output (Table A2-3, A2-4) pointed out that the structure is a twisted square antiprism (TSA) with a twist angle of 22.9° meaning that the coordination polyhedron itself is chiral and it may account for the high luminescence dissymmetry factor that we observed (see Chapter 1).[68] The bite angle is 73.0° which is especially small and definitely does not allow for water coordination to the axial position. This is consistent with the observation that the residual HDO signal in the NMR spectrum of $Cs[Ln(hfbcv)_4]$ systematically falls at 2.13 ppm, i.e. at the usual chemical shift of water in acetonitrile and it does not experience any Ln-dependent dia- or paramagnetic shift, as one would expect in the case of water participating in metal coordination.

Using a similar argument, we observed that ^{133}Cs-NMR spectra of $Cs[La(hfbcv)_4]$ and $Cs[Pr(hfbcv)_4]$ are practically identical, i.e. there is no detectable paramagnetic shift of ^{133}Cs.

This means that Cs^+ does not occupy a precise geometric position with respect to Pr^{3+} magnetic anisotropy tensor. Consequently, we do not deal with a true heterobimetllic complex, but rather with an anionic complex $[Ln(hfbcv)_4]^-$, which is remarkably different from what had been deduced for the apparently similar camphorate system $CsLn(hfbc)_4$.

All the investigated complexes show the presence of variable quantities of free ligand in solution and the exchange equilibrium between free and bound ligands in the *tetrakis* species is active. This could be demonstrated by means of a EXSY spectra which displays exchange cross peaks between all paramagnetically shifted signals and those of the free ligand.

The nature of this anionic *tetrakis* species can be best appreciated by contrast with *tris* $Ln(hfbcv)_3$, which we found present when using a different synthesis protocol (i.e. a biphasic system). In this case, EXSY experiments reveal that the *tetrakis* and *tris* forms are in slow exchange on the NMR timescale: this ensures that if the *tris* complex were present in the product of Cs_2CO_3 protocol, we would see its fingerprint in the NMR spectrum.

Standard bidimensional NMR techniques allowed us to assign the resonances related to $Ln(hfbcv)_3$ (Ln = Pr, Eu). We noticed that only in the samples containing the tris complex, the water resonance was shifted upfield indicating an axial coordination to the lanthanide, in $Ln(hfbcv)_3$, which, unlike the *tetrakis* species, is coordinatively unsaturated. The different behaviour of the $[Ln(hfbcv)_4]^-$ and $Ln(hfbcv)_3$ with respect to axial coordination was further investigated by testing them with DMSO which has a strong affinity for Ln^{3+}. Indeed, upon adding increasing quantities of DMSO to the mixture of *tris*/*tetrakis* Pr compounds, the water resonance recovered its standard shift at 2.13 ppm, DMSO resonance resulted shifted upfield, in accordance with axial coordination to Pr. Moreover, all the resonances assigned to the *tris* species were affected by the DMSO addition, while those of the tetrakis complex remained unchanged (Figure 2-8).

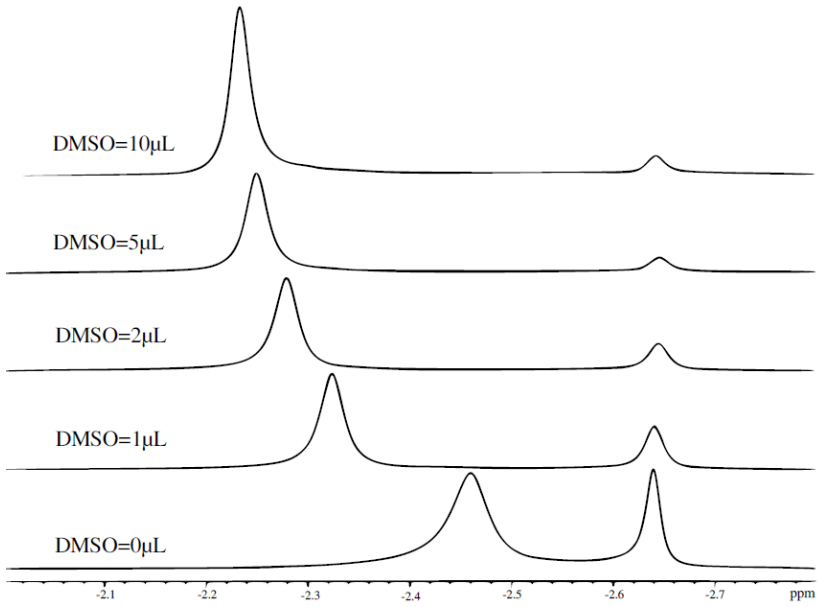

Figure 2-8. Me_9 (see Appendix A) resonances for Pr(*(R)*-hfbcv)$_3$ (left signals) and $[Pr(\textit{(R)}\text{-hfbcv})_4]^-$ (right signals) at increasing concentrations of DMSO.

We observed that during the titration, the molar ratio *tris*/*tetrakis* increased, suggesting that the *tris* species is stabilized by the axial coordination of DMSO. A quantitative analysis is reported in Appendix A (Table A2-5 and Figure A2-5).

Conclusions

We synthesized a new Eu species, with near UV excitation and highly circularly polarized photoluminescence in solid state (0.82 for the magnetic $^5D_0 \rightarrow {}^7F_1$ transition). We also investigated the structure of the series of complexes of early lanthanides through paramagnetic NMR spectroscopy and we propose a fast NMR method to distinguish between *tris* and *tetrakis* species.

Chapter 3

Development of Circularly Polarized Light Emitting Diodes Based on Chiral Lanthanide Complexes

Introduction

Organic light-emitting diodes (OLEDs) represent an attractive technology to fabricate efficient energy-saving light sources with high colour quality, wide viewing angles and a true black colour.[87,88]

Although OLEDs available on the market, in the form of OLED lamps, OLED-TVs, OLED display-equipped portable devices, generate exclusively unpolarized electroluminescence (EL) emission, investigation on linearly polarized EL emission of organic systems[89,90] has been stimulated in the last years by development of stereoscopic 3D-displays. Circularly polarized (CP) light has further found intriguing photonic applications such as molecular photoswitches,[91] optical data storage,[92] optical quantum information[93] and spintronics[78] and its use in other fields, such as chirality sensing[94,95] or enhanced image contrast in advanced medical imaging techniques,[96] appears promising.

The ability to control the polarization of the emitted light in conjugated molecular and polymeric systems is a fascinating issue in the design of new materials. While this is well established for CP photoluminescence (PL), the direct generation of CP EL still lags behind. Yet, it would be more efficient in terms of device simplicity (thickness), production costs and integration with other organic optoelectronic devices (transistors, photodetectors), with respect to conventional CP devices employing polarizing filters.[97]

In order to achieve CP EL, the emitting material must be chiral and non racemic, in addition to all the expected features for electroluminescent devices.

Direct CP EL generation was first demonstrated in a chiral-substituted poly(*p*-phenylenevinylene) (PPV) derivative[98] and since then two main strategies have

been followed in the design of such devices: decorating the light-emitting polymer with chiral side-chains, or doping *achiral* polymers with a chiral molecule (Figure 3-1). Geng et al.[99] achieved the highest g_{EL} value of 0.35 reported so far, by employing a hyperbranched poly(fluorenevinylene). Oda et al.[97] measured g_{EL} of 0.16 and −0.25 for liquid-crystal chiral-substituted polyfluorene-based OLEDs. In these cases, circular polarization stems from the chiral supramolecular organization of the active layer, which may be strongly temperature- and possibly batch-dependent.[59]

Following the second approach, Fuchter et al.[100] obtained a g_{EL} value of 0.2 by doping a conventional (achiral) polymer with a helicene as the chiral inducer. An advantage of this strategy consists in the use of a previously optimized and efficient electroluminescent material, although the considerable amounts of the chiral inducer can perturb the emitter properties and affect the homogeneity of the active layer.

As typically occurs for polymer-based OLEDs, the emission band is broad, covering a relevant part of the visible spectrum; interestingly, the g_{EL} value remains almost constant throughout the band.

Although wide bands and constant g values may be desirable for certain applications,[78,92] there are other ones for which nearly monochromatic emission is requested (e.g. for highly saturated colours).[101-103] Furthermore, higher levels of CP EL are essential in order to switch to practical application in chiral optoelectronics and photonics.

Sharp bands can be generated employing OLEDs based on lanthanide complexes. Moreover, Eu(III)-based OLEDs have potential for a high electroluminescence internal quantum efficiency, thanks to their ability of harvesting triplets for light emission. Indeed, Eu(III)-based OLEDs are now an established technology for standard non-polarized electroluminescent devices[101,104] and recently devices embedding Eu(III) beta-diketonate complexes with external quantum efficiency (EQE) exceeding 4 %[105] and tunable color emission were reported.[14]

As described in the previous Chapters, other intriguing features of Ln(III) complexes are the outstanding chiroptical properties displayed by chiral compounds, but notably their use as circularly polarized electroluminescent emitters has never been investigated so far.

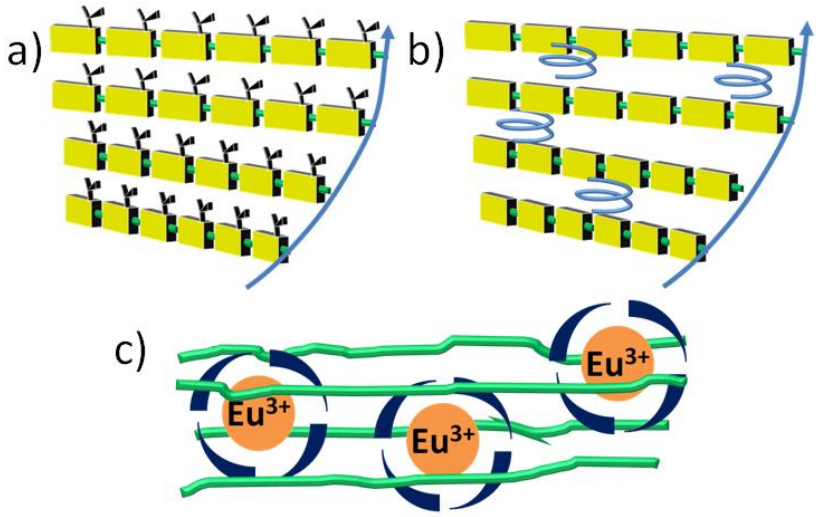

Figure 3-1. Three strategies employed in CP-OLED: a) polymers with chiral sidechains, able to form chiral supramolecular aggregates; b) a chiral small molecule dopant, inducing chirality on an achiral emissive polymer; c) our approach based on emissive small chiral molecules, endowed with high intrinsic polarized emission dispersed in a polymer host. This figure has only a diagrammatic purpose.

Results

In this Chapter, we present a completely novel approach for manufacturing an OLED with high intrinsic circularly polarized sharp red emission with a level of CPEL as high as 70 %, largely outperforming previously reported results (Figure 3-1). For the first time, we used a chiral lanthanide complex as the guest emitter in a well established solution-processed polymer-based device and we investigated the critical factors affecting g_{EL} value in CP-OLEDs.

For this prototype device, the Ln(III) complex $CsEu(hfbc)_4$ (Figure 3-2a), with the highest available CP PL (g_{PL} = 1.38 at 595 nm, meaning a I_L/I_R ratio of 85:15, see also Chapter 1) for a lanthanide system,[22] was selected as the chiral emitter. Even

though it has a low PL quantum yield (3% as powder), for our purposes, it provides a very good trade-off between polarization and total luminescence. Moreover, very recently, Yuasa et al.[85] reported that the photophysical properties of $CsEu(hfbc)_4$ (g_{EL} and PLQY) can be improved in solid state thanks to specific packing and aggregation modes.

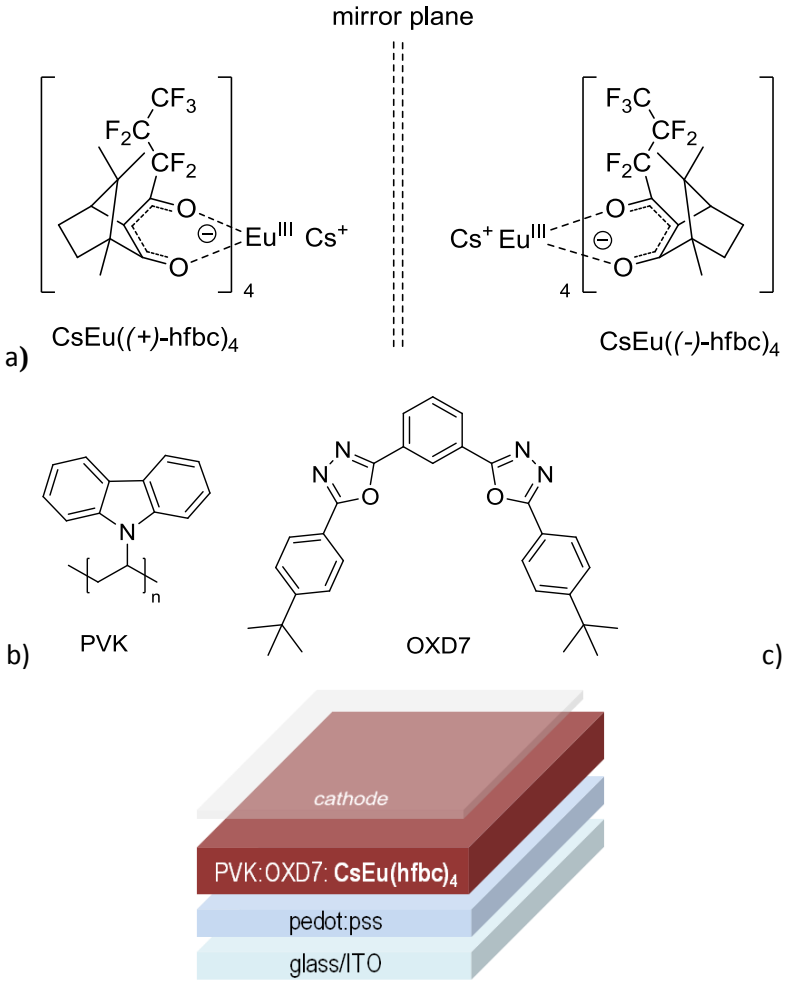

Figure 3-2. Molecular structure of the two enantiomers of $CsEu(hfbc)_4$ (a); PVK polymer host and OXD7 additive constituting the blend for the emitting layer (b); Device architecture showing the thin film containing the Eu(III) complex-based active layer, sandwiched between a PEDOT:PSS-coated ITO anode and a Ba/Al cathode (c).

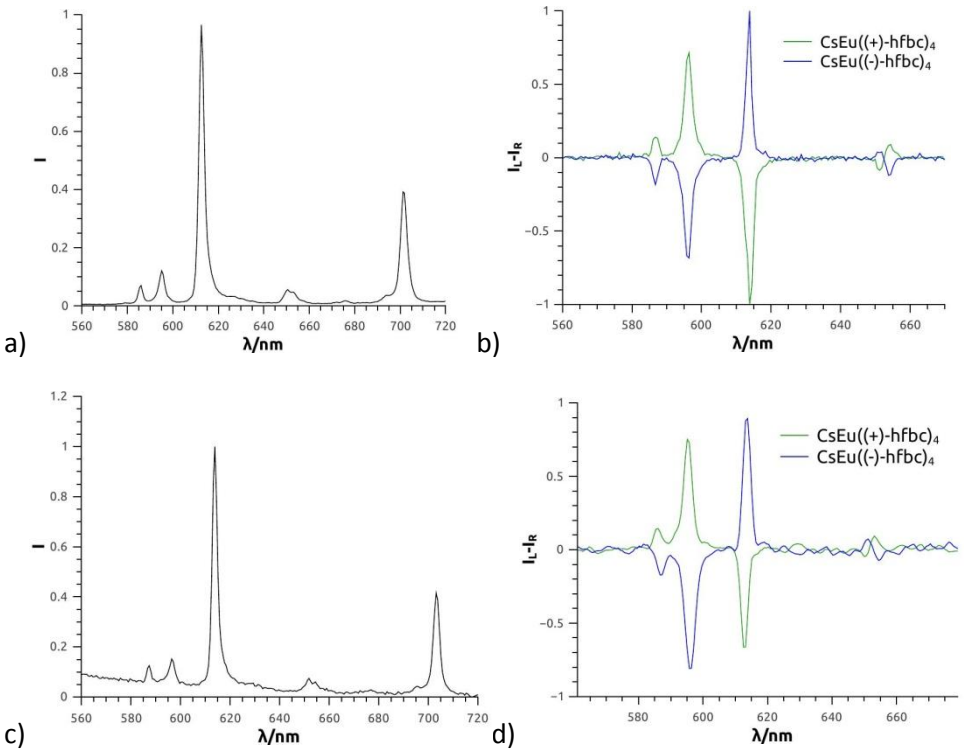

Figure 3-3. Photoluminescence of $CsEu(hfbc)_4$ in $CHCl_3$ solution (a) and in the blend film (c) and circularly polarized photoluminescence of (b) $CHCl_3$ solution; d) film. λ_{exc} = 360 nm.

In our strategy for the development of the CP-OLED architecture, two critical issues were addressed: inhibition of all the emission from the matrix, in order to have light stemming only from the Eu(III)-complex, and minimization of internal reflection of emitted light on the back electrode, to preserve CP EL.

In such CP-OLEDs the emission from the matrix is undesired because all the photons arising from other sources than the chiral Eu(III) complex would reduce the chiroptical response (in terms of *g*-factor) of the system. We focused on the easily processable polyvinylcarbazole (PVK, Figure 3-6b), possessing good hole transport properties and weak electroluminescence, which was demonstrated as a suitable host for Eu(III) complexes.[106,107] In order to provide a better carrier transport and carrier/exciton confinement, a soluble oxidiazole derivative, 1,3-

bis[2-(4-tert-butylphenyl)-1,3,4-oxadiazo-5-yl]benzene (OXD7, Figure 2-6b), was added to the blend, typically in the ratio PVK:OXD7/3:1. We found that a concentration of 10 wt.% of the Eu(III) complex emitter in the blend was optimal to collect pure Eu(III)-centred emission (Figure 3-3c, Figure A3-2), although in the PL spectrum the PVK emission was still dominant in the blue region (Figure A3-1).

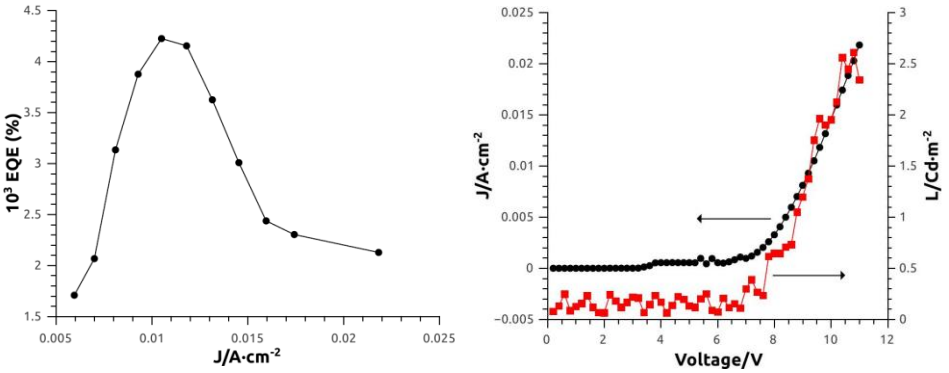

Figure 3-4. left: Total external quantum efficiency versus current density J; **right:** Representative curve of J (circles) and luminance L (squares) as a function of applied voltage.

The reflection of light reverses the handedness of CP light: if this occurs on the back electrode, the polarization of light exiting the ITO window would be reduced,[98] even though the intrinsic emission of the active component in the device is strongly polarized (Figure 3-3b,d). The usual configuration of OLEDs consists in a fully reflecting metal top electrode, in order to collect also the photons emitted opposite to the transparent substrate. In our devices, this would be highly detrimental and therefore the reduction of the cathode thickness to obtain a semi-transparent surface is imperative. A Ba/Al cathode was preferred to the more conventional LiF/Al/Ag,[108] commonly used in top-emitting devices, since it was demonstrated as a good electrode in PVK-based devices.[14] A 50 % cathode transmittance was found to be suitable to grant reduced reflection, thus ensuring a highly polarized EL with a good stability.

Following this strategy, we fabricated devices with a very basic architecture: on top of PEDOT:PSS covered glass/ITO substrate, a $CsEu(hfbc)_4$ 10wt.%-doped PVK:OXD7 single active layer was deposited by spin-coating technique

(Figure 3-2c). The appropriate solvent and concentration of the solution ensured good film quality (Figure A3-5). Devices with 4 nm Ba and different Al cathode thickness in the range from 80 nm to 6 nm (50% transmittance at 612 nm) were built to investigate the effect of internal reflections on the g-factor. The maximum EQE, measured as the total number of emitted photons on number of injected carriers, was $4.2 \cdot 10^{-3}$ % (current efficiency $5 \cdot 10^{-3}$ Cd/A, power efficiency $6.7 \cdot 10^{-3}$ lm/W, Figure 3-4 and A3-4). Devices switched on at about 8 V and were driven at 20 mA/cm^2 (about 10 V) for recording CP EL spectra. The light was collected from the glass surface in perpendicular direction and the stability of the emission spectra was verified for the time required for the characterization (Figure A3-4).

The total EL spectrum (Figure 3-5a) showed the typical Eu(III)-centred emission in a wide range of driving voltages (Figure A3-2).

The CP EL was measured by using a quarter wave retarder and a linear polarizer prior to a CCD detector. By rotating the easy axis of the quarter wave plate by ±45° with respect to the linear polarizer, the I_L and I_R polarized components of the emission were alternatively acquired. By subtracting the I_L and I_R spectra, the CPEL spectra were obtained; g_{EL} was derived according to the definition reported above.

The CP EL spectra obtained for the devices containing the two enantiomers ($CsEu((+)\text{-hfbc})_4$ and $CsEu((–)\text{-hfbc})_4$), were almost perfectly mirror image (Figure 3-5b) and showed the same patterns of bands reported for the CP PL spectra measured in $CHCl_3$ (Figure 3-5b).[22] This excludes all artifacts due to linear polarization and birefringence of any component in both OLEDs and detection apparatus. It further ensures that the observed CP EL is Eu(III)-centred, ruling out any contribution of the polymeric matrix to the measured EL and CP EL.

A g_{EL} value of about ±0.75, at 595 nm (for the Eu $^5D_0 \rightarrow {}^7F_1$ transition, see Table 3-1), was recorded from the devices with the thinnest cathode (4 nm Ba + 6 nm Al); this means that about 70 % of the EL is circularly polarized. To

the best of our knowledge, this is the highest value ever measured for a CP-OLED and the very first report of lanthanide-centred circularly polarized EL.

Similarly, the CP EL of the band at 612 nm (for the Eu $^5D_0 \rightarrow {}^7F_2$ transition, see Table 3-1) showed a value of g_{EL} of −0.09/+0.15. As expected from the PL spectrum, this band possessed an opposite sign with respect to the emission at 595 nm. The measurements carried out on devices with different cathode thickness showed an exponential-like reduction of g_{EL} upon increasing electrode thickness (Figure 3-7).

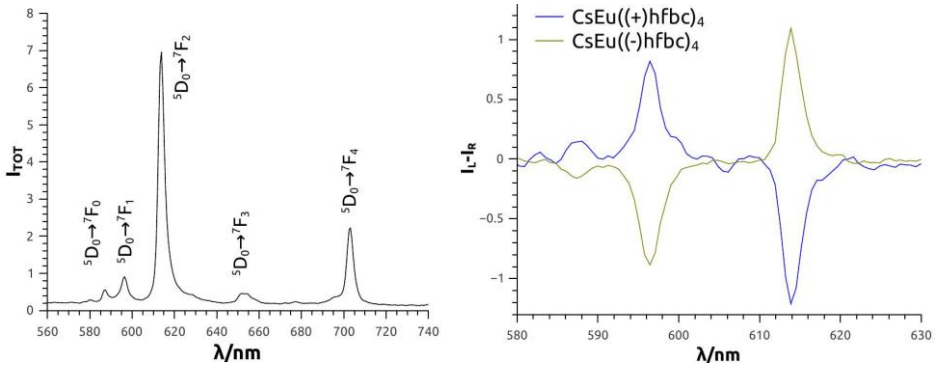

Figure 3-5. left: EL spectrum of CsEu(hfbc)$_4$-based OLEDs; **right:** CPEL of the devices containing each enantiomer of CsEu(hfbc)$_4$. See Appendix A for acquisition details.

Table 3-1. EL dissymmetry factors (g_{EL}) for CsEu(*(±)*-hfbc)$_4$-based devices with standard deviations (σ_d) and PL dissymmetry factors (g_{PL}) of the complexes in $CHCl_3$ solution.

	g 595 nm ($^5D_0 \rightarrow {}^7F_1$)	**g** 612 nm ($^5D_0 \rightarrow {}^7F_2$)
CsEu(*(+)*-hfbc)$_4$ g_{EL} (σ_d)	+0.73 (0.08)	–0.09 (0.05)
CsEu(*(–)*-hfbc)$_4$ g_{EL} (σ_d)	–0.79 (0.02)	+0.15 (0.06)
CsEu(*(+)*-hfbc)$_4$ g_{PL} (σ_d)	+1.41 (0.04)	–0.25 (0.04)
CsEu(*(–)*-hfbc)$_4$ g_{PL} (σ_d)	–1.41 (0.05)	+0.22 (0.04)

In order to explain the variation of the polarization outcomes with the reflectivity of the cathode, we may consider that about 50 % of the emitted light is directed forward and exit the transparent anode window without any polarization loss. On

the other hand, the other half of the emitted light is directed backward towards the cathode and it is reflected (Figure 3-6).

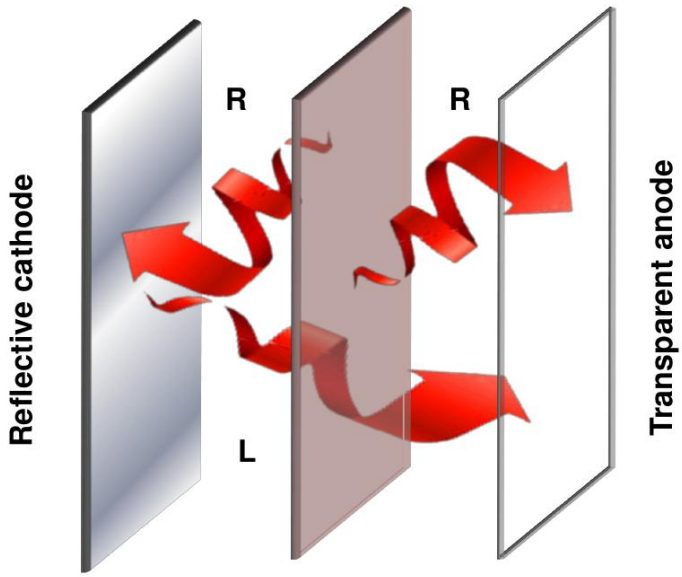

Figure 3-6. Pictorial illustration of the effects of reflection on polarization inside a CP-OLED.

If R is the reflectivity of the Al coating, we get that the two polarized components exiting the device (I'_L and I'_R) are:

$$I'_L = I_L + R \cdot I_R \quad (3\text{-}1a)$$

$$I'_R = I_R + R \cdot I_L \quad (3\text{-}1b)$$

By the definition, we get that the measured g_{EL} for the device is:

$$g_{EL} = 2\frac{(I'_L - I'_R)}{(I'_L + I'_R)} \quad (3\text{-}2)$$

Substituting Eq. (3-1a) and (3-1b) in Eq. (3-2), we get:

$$g_{EL} = g_{EL}^{(0)}\frac{(1-R)}{(1+R)} \quad (3\text{-}3)$$

Where $g_{EL}^{(0)}$ is the intrinsic dissymmetry factor of the chiral europium species.

Hass and Waylonis[109] reported the reflectivity R of Al thin layers for various thicknesses.

Using these data we may calculate the expected g_{EL} values as a function of the Al cathode thickness of our devices from Eq. (3-3) with $g_{EL}^{(0)} = 1.38$. In Figure 3-7, we report these values along with our experimental points.

R reaches a limiting value of about 0.91[109] and therefore Eq. (3-3) predicts a limiting value of 0.07, experimentally we found a value of about 0.1 for an Al thickness of 80 nm (Figure 3-7).

Of course these considerations are solely intended to heuristically correlate the experimental trend that we observed with simple experimental values. We do not aim here to advance a comprehensive model which would require knowing several other parameters.

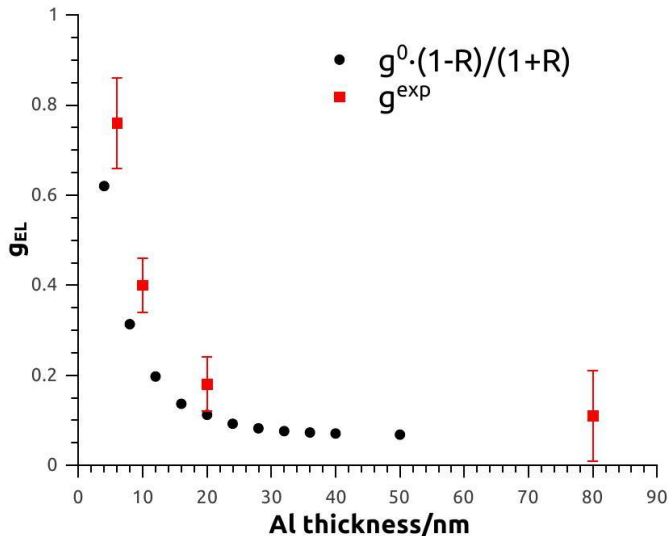

Figure 3-7. Four experimental g_{EL} values obtained for the transition at 595 nm as a function of the cathode thickness (red squares). The error bars represent ±2 standard deviations**.** Black circles represent g_{EL} values calculated using R by Hass and Waylonis[109] and Eq. (3-3) as a function of cathode thickness.

Conclusions

In this Chapter, we have presented a novel approach for manufacturing OLEDs with intrinsic sharp CP emission. For the first time a chiral lanthanide complex was successfully used as the direct circularly polarized emitter in a well-established solution-processed device and an unprecedented study of the effect of cathode transmittance on the level of CPEL was carried out. Following our strategy, we manufactured devices that outperform known CP-OLEDs by at least a factor 2 in terms of g_{EL} value.

Chapter 4

Optimization of lanthanide based CP-OLEDs

Introduction

The promising results obtained in the field of CP-OLEDs, described in the Chapter above, prompted us to propose strategies to improve the EQE of the devices and their polarization performances at the same time. We were especially interested in understanding the factors affecting the fate of the polarization inside the CP-electronic device by combining experimental data and rational modelling.

Again, in the manufacturing of CP-OLEDs, we resorted to $CsEu(hfbc)_4$, since its highly polarized emission is very convenient for identifying key factors that affect circular polarization in CP-OLEDs.

For a correct operation in a solution processed OLED, the β-diketonate Eu(III)-complex must necessarily be homogeneously dispersed in a semiconducting conjugated matrix (so called host/guest approach)[41,105] that features a sufficiently high triplet energy (E_T) to prevent energy back transfer,[41] suitable HOMO/LUMO energy levels to confine radiative excitons on the guest sites, and a bipolar charge transport. The matrix plays an even more crucial role in CP-OLEDs behaviour since its emission can be broad and it is certainly not polarized, which is an issue for both colour purity and polarization performance (g_{EL}) of the device. Hence, the selection of a good compound as host and the optimal blend formulation to address at the same time all those issues is very challenging.

Results

<u>Active layer optimization</u>

Our earlier results, described in the previous Chapter, showed that polyvinylcarbazole (PVK, Figure 3-2b) is a suitable host for $CsEu(hfbc)_4$ complex

to achieve Eu-centered EL with large g_{EL}.[76] However, the difference between g_{PL} and g_{EL} was significant, indicating that there is still room for improvement of the polarization performances of the devices.

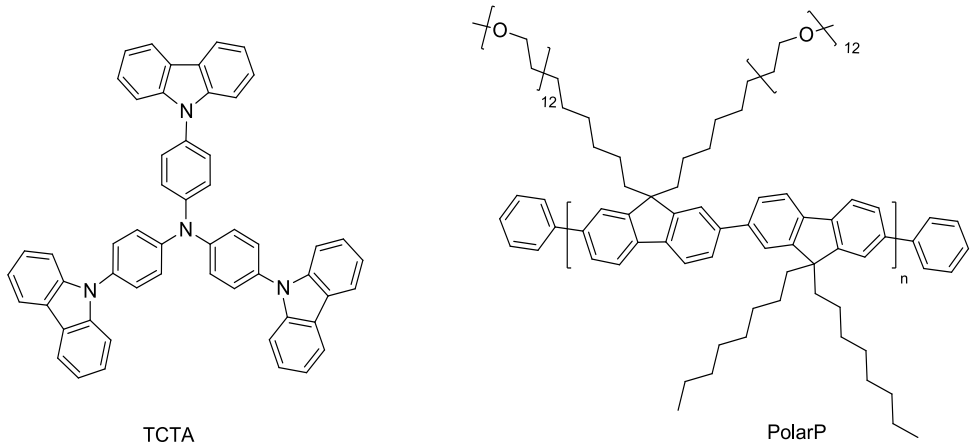

Scheme 4-1. Chemical structures of TCTA and PolarP used as interfacial layer (IL).

The commercially available tris(4-carbazoyl-9-ylphenyl)amine (hereafter TCTA, Scheme 4-1) is here proposed as an alternative to PVK in solution-processed CP-OLEDs, since with respect to PVK, its UV emission is spectrally more separated from Eu(III) complex emission, this would be beneficial for higher polarization degree. E_T of TCTA (2.8 eV, Table A4-1) is high enough with respect to CsEu(*(–)*-hfbc)$_4$ one (2.45 eV) to avoid energy back transfer. The electron transporting 1,3-Bis[2-(4-tert -butylphenyl)-1,3,4-oxadiazo-5-yl]benzene (OXD7, Figure 3-2b) is added to the blend to achieve bipolar charge transport.

The CsEu(*(–)*-hfbc)$_4$ complex is dispersed in TCTA:OXD7 (1:1 wt) in 12 % wt mass ratio and the mixture is dissolved in $CHCl_3$ (15 mg/mL). The present study was conducted only on the enantiomer CsEu(*(–)*-hfbc)$_4$ as we demonstrated previously that the behavior of the two enantiomers is identical (*viz.* opposite) within the experimental error, as expected.[76]

The absorption spectrum (Figure 4-1a) is dominated by the host matrix with a main peak at 295 nm and shoulders at 320, 330 and 350 nm, and the absorption band of CsEu(*(–)*-hfbc)$_4$ lies beneath, with a peak at 310 nm. Films are highly

transparent (transmittance, T > 96 %) in the visible range 400-700 nm (Figure A4-1). Once excited at 330 nm, the PL spectrum features the desired red emission with typical Eu(III) transitions and an UV contribution (peak at 369 nm) from the matrix (Figure 4-1b). The spectral overlap between host emission and Eu(III) complex absorption (Figure 4-1c) enables a long-range resonant energy transfer (FRET) from the matrix to the CsEu(*(–)*-hfbc)$_4$ complex. In fact, the PL excitation spectrum (PLE, (Figure 4-1c) of TCTA:OXD7:12wt.% CsEu(*(–)*-hfbc)$_4$ film monitored at 612 nm (Eu-complex hypersensitive transition) shows contributions of both OXD7 and TCTA. The electronic circular dichroism signal of the blend film (Figure 4-1d) is identical in shape to the spectrum of the complex in solution. This is a strong indication that the chiral Eu complex in the active layer has the same structure as the one studied in solution. The CP PL of the blend film (Figure **4-1**e) displays g_{PL} values of -1.21 ± 0.02 and 0.16 ± 0.02 for 595 nm ($^5D_0 \rightarrow {}^7F_1$) and 612 nm ($^5D_0 \rightarrow {}^7F_2$) transitions respectively. These values are only slightly lower than CsEu(hfbc)$_4$ in solution, meaning that the TCTA:OXD7 matrix has little influence on the intrinsic polarization of the complex. Spin-coated films are homogeneous and very flat with root mean square roughness of 0.22 nm (Figure 4-1f).

On the basis of this optimal blend formulation, we manufactured CP-OLEDs with the architecture ITO/PEDOT : PSS/TCTA : OXD7 : CsEu(*(–)*-hfbc)$_4$ (12 wt.%)/Ba/Al (Figure 4-2a). The thickness (*d*) of the active layer affects g_{EL}, thus it was fixed at 75 ± 5 nm, since this value showed the best performance in PVK-based devices.[76]

The Ba/Al layer used as a cathode in OLEDs is typically thick (d > 100 nm) in order to reflect all the radiation back to the transparent glass substrate, but the reflection of the emitted light is a major issue for the polarization performance of the CP-OLEDs, as explained in Chapter 3. To further (Figure 3-7) quantify the effect of reflection at the cathode on the PL polarization, we cover the blend film with 100 nm thick Al film and measure the CP PL by exciting and collecting light from the glass side (back scattering configuration). The g_{PL} values are lowered to

-0.11 ± 0.01 (from -1.21 in the uncovered film) at 595 nm and below the experimental error at 612 nm.

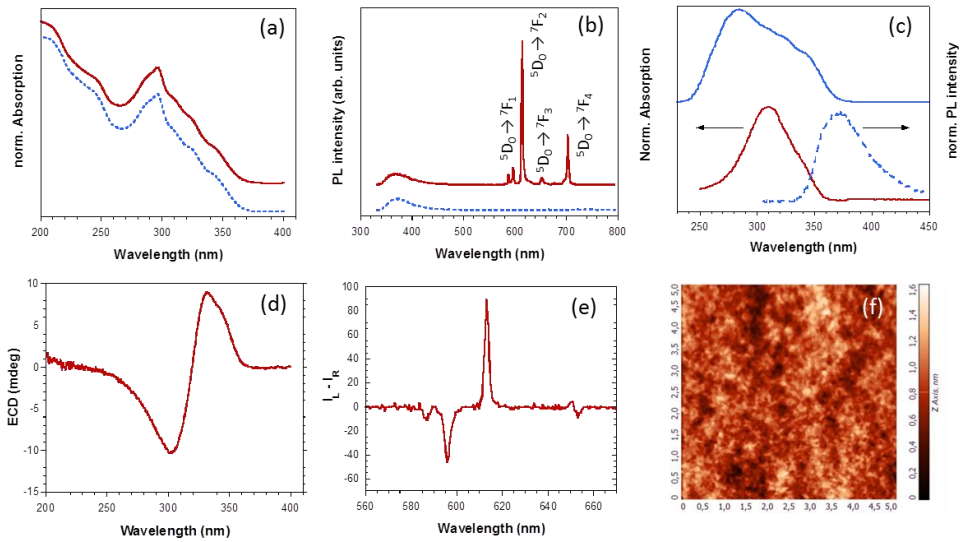

Figure 4-1. (a) Normalized absorbance and (b) PL spectra of TCTA:OXD7 (blue dotted line) and TCTA:OXD7:CsEu(*(–)*-hfbc)$_4$ (red solid line, vertically shifted for clarity) films excited at 330 nm; (c) normalized absorption of CsEu(*(–)*-hfbc)$_4$ solution (red solid line), PL spectrum of TCTA:OXD7 film (blue dotted line) and PLE of TCTA:OXD7:CsEu(*(–)*-hfbc)$_4$ film (blue solid line); (d) ECD and (e) CP PL spectrum of TCTA:OXD7:CsEu(*(–)*-hfbc)$_4$ film; (f) AFM tapping mode 5 x 5 μm image of TCTA:OXD7:CsEu(*(–)*-hfbc)$_4$ film.

In CP-OLEDs, the dependence of g_{EL} on cathode transparency, hence on its reflectivity, is also investigated and compared to the results achieved earlier with PVK as a host. A film of 4 nm of Ba is deposited by thermal evaporation in high vacuum ad successively covered by 6 nm (device A), 20 nm (device B) or 110 nm (device C) of Al layer (Figure 4-2a). Accordingly, the cathode transmittance (T) ranges from 50 % to ~0 %. The EL spectra for all the devices show pure Eu-centred emission, with main typical transitions $^5D_0 \rightarrow {}^7F_1$ (595 nm), the hypersensitive $^5D \rightarrow {}^7F_2$ (612 nm), $^5D_0 \rightarrow {}^7F_3$ (around 635 nm), and $^5D_0 \rightarrow {}^7F_4$ (around 700 nm) (Figure 4-2c). The CP EL was measured by following the method reported in the previous Chapter.

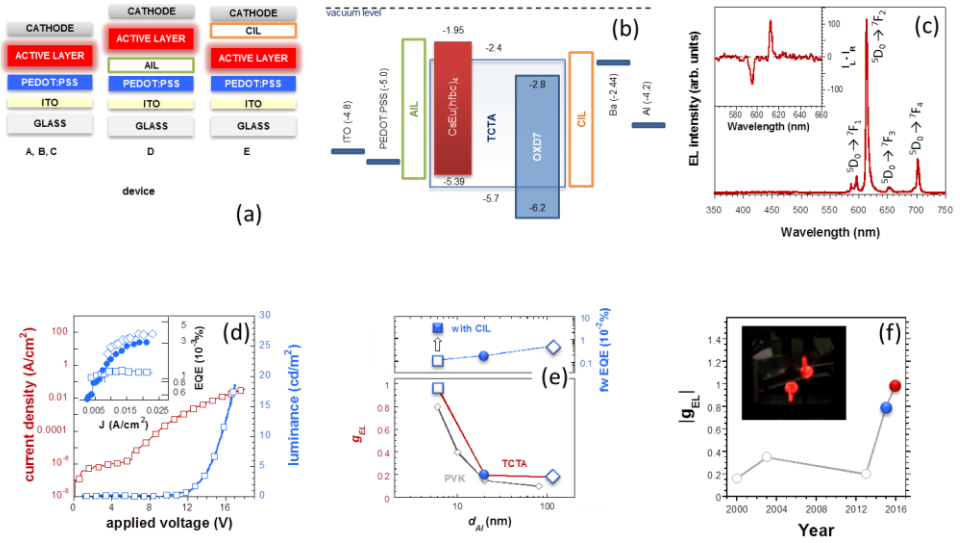

Figure 4-2. (a) Investigated CP-OLED architectures: single layer with 6 nm (A), 20 nm (B) and 110 nm (C) Al thickness, with AIL (D) and CIL (E) charge regulating layers; (b) flat band energy level diagram of all CP-OLEDs constituent layers; (c) representative EL spectra of CP-OLED featuring typical Eu(III) complex transitions and (inset) CP EL of the device A; (d) representative JLV characteristic curves of device A and (inset) EQE recorded in forward (fw) direction (glass side) for the devices A (□), B (●), C (◇); (e) g_{EL} and EQE of devices A (□), B (●), C (◇), E (■) versus Al layer thickness; g_{EL} (◇) behavior of ITO/PEDOT:PSS/PVK:OXD7:CsEu((–)-hfbc)$_4$/Ba/Al is reported for comparison; (f) chronologic evolution of g_{EL} values of CP-OLEDs: state-of-the-art (●)[76] and present work (●); inset, image of working CP-OLEDs prototype.

For the semitransparent Al layer (device A, d_{Al} = 6 nm) we measure a remarkable $g_{EL} = -1.00 \pm 0.08$ at 595 nm and 0.19 ± 0.08 at 612 nm (Table 4-1). This outstanding result outperforms the state-of-the-art CP-OLEDs,[76] with about 75 % of the emitted photons at 595 nm being circularly polarized (Figure 4-1f). For a less transparent cathode (device B, d_{Al} = 20 nm), the g_{EL} drops to -0.21 ± 0.06 and -0.03 ± 0.01 at 595 nm and 612 nm respectively, which is slightly higher than in the case of PVK host. For a cathode with the maximum reflection (device C, $d_{Al} > 100$ nm), the g_{EL} is further reduced to -0.15 ± 0.06 at 595 nm and 0.03 ± 0.01 at 612 nm, in agreement, in the range of experimental error, with the values of g_{PL} of Al-covered blend film (Table 4-1).

Table 4-1. PL and EL dissymmetry factors (g_{PL} and g_{EL}) for CsEu(*(-)*-hfbc)$_4$ dispersed in different host matrices.

host	**device**	**d_{Al} coverage**[a] (nm)	**g_{PL} (σ_d)**		**g_{EL} (σ_d)**	
			595 nm ($^5D_0 \rightarrow {}^7F_1$)	612 nm ($^5D_0 \rightarrow {}^7F_2$)	595 nm ($^5D_0 \rightarrow {}^7F_1$)	612 nm ($^5D_0 \rightarrow {}^7F_2$)
solution ($CHCl_3$)	/	none	-1.35±0.09	+0.15±0.02	/	/
PMMA	/	none	-1.35±0.10	+0.13±0.02	/	/
PVK:OXD7[76]	/	none	-1.30±0.13	+0.20±0.02	/	/
PVK:OXD7[76]	state-of-the-art	6	/	/	−0.79±0.02	+0.15±0.06
TCTA:OXD7	/	none	-1.21±0.02	+0.16±0.02	/	/
TCTA:OXD7	A	6	/	/	−1.00±0.08	+0.19±0.08
TCTA:OXD7	B	20	/	/	−0.21±0.06	+0.03±0.01
TCTA:OXD7	C	110	-0.11±0.01	+0.01±0.01	−0.15±0.06	+0.03±0.01
TCTA:OXD7	D	6	/	/	−0.61±0.14	+0.07±0.04
TCTA:OXD7	E	6	/	/	−0.88±0.14	+0.14±0.09

a) in addition to 4 nm Ba layer

As expected, the EQE, measured in the forward direction, through the glass substrate, increases progressively along with the increase of cathode thickness (inset of Figure 4-2d) up to the maximum value of $5 \cdot 10^{-3}$ % for device C, thanks to the more efficient extraction of photons from the glass side. The rather low values of EQE, comparable to the earlier achievements, impose the search of new approaches for enhanced efficiencies in order to validate CP-OLED technology in the laboratory. Moreover, although the effect of cathode transparency is established, the gap between g_{EL} (~1 at 595 nm) in the prototype with respect to g_{PL} (~1.21 at 595 nm) is still significant, therefore other factors affecting CP EL must be still identified.

Factors affecting CP EL inside the device

Since the amount of light reflected at the cathode is a very critical factor for g_{EL}, in the following we analyze how the position and width of the recombination zone (RZ) of radiative excitons, might affect the polarization of the light collected at

the anode. This aspect was neglected in the simplified model exposed in the previous Chapter[76] for proof-of-concept CP-OLEDs. To clarify the effect of RZ position and propose a more accurate model able to describe the g_{EL} trend, we fabricated CP-OLEDs with different positions of the RZ.

A single layer CP-OLEDs with device A architecture but with the blend TCTA:CsEu(*(–)*-hfbc)$_4$, which features unbalanced charge carrier transport, as active layer was firstly manufactured and characterized. In this configuration, due to the prevalent hole transporting character of the active layer, the RZ is expected close to the cathode interface and we observed a reduction in g_{EL} value to −0.6 at 595 nm with a very poor EQE.

On the other hand, the use of interfacial layers (ILs) is not only an effective way to improve device performances but also allows one to control the position of the RZ. The IL approach was developed in OLED technology to control charge carrier injection and blocking, hence providing the exciton confinement within the emissive layer and boost the performance. Since it requires to deposit an additional layer it has been a unique prerogative of vacuum deposited OLEDs for years. Recently, by keeping the solution process method, semiconducting IL have been developed to fabricate a multi-layered OLED architectures. In fact, besides cross-linkable materials, IL compounds with solubility in orthogonal solvents with respect to the active layer can be selected, hence the successive deposition from solution of the functional layers becomes possible. The performance of IL-optimized solution processed devices are largely improved in terms of EQE, with a lower turn-on voltage that reduces electrical stress.

The multi-layered approach is totally unexplored in CP-OLEDs technology. Here we fabricate two different architectures, by inserting an IL either at the anode (AIL) or at the cathode (CIL), as shown in Figure 4-2a for devices D and E, respectively. Beside the possible efficiency enhancement, these architecture would allow us to move the position of RZ close to the cathode or to the anode interfaces hence facilitating the analysis of the effects on g_{EL}.

In the first device architecture (device D), a RZ close to the cathode is obtained by inserting a thin film of hole transporting PVK as the anode IL (AIL, Scheme 4-1) onto the ITO/PEDOT:PSS glass substrate. The 30 nm thick PVK film, deposited from chlorobenzene solution by following the protocol developed earlier Giovanella, 2011, is optimal for OLED performance. Moreover, the PVK film is fully transparent to Eu(III) complex emission (T > 99 % of 30 nm thick PVK film). The active layer is then deposited from $CHCl_3$ solution and the device is capped with a semitransparent cathode to give the architecture ITO/PEDOT:PSS/AIL/TCTA:OXD7:CsEu(*(–)*-hfbc)$_4$/Ba/Al. The introduction of the PVK layer with a suitable HOMO energy level ($HOMO_{PVK}$ = −5.44 eV, Figure 4-2b) mitigates the potential energy barrier (~0.7 eV) for hole injection into the active layer ($TCTA_{HOMO}$ ~5.7 eV) at the PEDOT:PSS/active layer interface. The facilitated hole injection, combined to the higher hole mobility of TCTA than electron mobility of OXD7, most likely shifts the RZ towards the cathode interface. For this device, we observed the reduction of g_{EL} values down to -0.61 ± 0.14 at 595 nm and 0.07 ± 0.04 at 612 nm, and a low forward-EQE ($2 \cdot 10^{-3}$ %).

The device with RZ close to the anode (device E) is obtained by insertion of a cathode IL (CIL) on top of the active layer prior to the metallic cathode deposition. The CIL consists of the alcohol soluble polar polymer Poly[(2,7-(9,9'-dioctyl)fluorene)-alt-(2,7-(9,9'-bis(5"-polyethylene oxide) pentyl)fluorene)] (PolarP, Scheme 4-1), which showed quite considerable benefits for solution processed LEDs.[110] Thanks to the formation of an electrical dipole at the interface, the CIL promotes the injection of electrons into the active layer and, as a consequence, the RZ is expected to be displaced far from the cathode (i.e. closer to the anode). Besides, the ITO/PEDOT:PSS/TCTA:OXD7:CsEu(*(–)*-hfbc)$_4$/CIL/Ba/Al, with semitransparent cathode, exhibits an enhanced forward-EQE up to 0.05 %, ten times higher than the control device A. The light switches on at 6 V (it was 9 V without CIL) displaying the typical pure Eu-complex EL spectrum. The g_{EL} values of -0.88 ± 0.14 and 0.14 ± 0.09 at 595 nm and 612 nm respectively along with the increased efficiency are very significant with respect

to the state-of-the-art,[76,100] although g_{EL} is slightly lower than in the control device A.

All these observations clearly show that the IL has a remarkable effect on the g_{EL} which, to a first understanding, should depend only on the intrinsic property of the emitter combined to the detrimental effect of back electrode (cathode) reflection, as described in the previous Chapter.

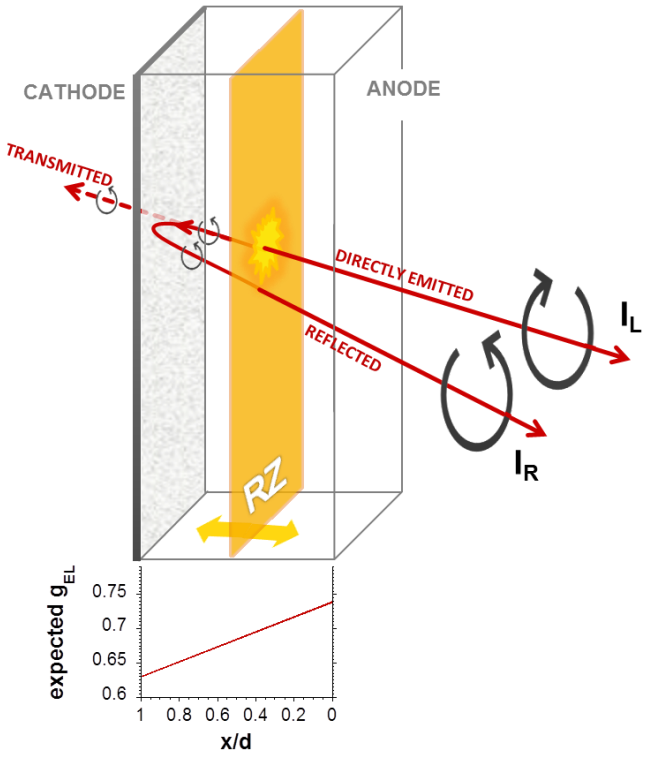

Figure 4-3. Schematic view of a CP-OLED to illustrate the collection of left- and right-handed CP light. The RZ is represented as an orange thin plane at a distance x from the anode. Curved arrows represent left- and right-handed light polarization: forward and backward direct emitted and reflected light. The loss of degree of circular polarization expected by the model with respect to normalized position of RZ is shown, calculated according to Eq. (4-1) with reasonable values for semitransparent device: $g_{EL}^{(0)} = 1.38$, $t_0 = 0.9$, $R = 0.38$.

In that model, we completely neglected any additional depolarization process within the device, eventually due to scattering, interlayer reflections etc. Indeed, in more complete view, we should consider that, on its travel to the transparent

anode, light is attenuated by scattering and absorption processes in the various layers it goes through, which can be conveniently expressed by the transmittance. By itself, this attenuation has minor effect on light polarization, but it changes the relative proportion of light directly emitted forward and light emitted backwards, that reaches the anode only after reflection on the cathode (Figure 4-3). For this reason, the geometrical location of RZ may play a major role.

We assume that excitons are mainly generated in the host and successively transferred, through the FRET mechanism discussed above, to the CsEu(*(–)*-hfbc)$_4$ complex, even if the contribution from direct charge trapping at the chiral emitter sites can not be excluded. We consider that half of the light is emitted forward and half is emitted backward. The light emitted forward is attenuated by a factor depending on T of the active layer itself and of the front layers (PEDOT:PSS, PVK), between RZ and glass. On the contrary, the light emitted backward, attenuated during its travel from the RZ to the cathode, is reflected and changes its handedness. This component reaches the anode undergoing a further attenuation. Eq. (4-1) (see Appendix A for the full derivation) is proposed to describe g_{EL} behaviour with respect to RZ position and takes into account the two polarized components I_L' (left) and I_R' (right) actually collected at the glass side:

$$g_{EL} = 2\,\frac{I_L' - I_R'}{I_L' + I_R'} = g_{EL}^{(0)}\,\frac{1 - R\cdot e^{-2\alpha(d-x)}}{1 + R\cdot e^{-2\alpha(d-x)}} \qquad (4\text{-}1)$$

where $g_{EL}^{(0)}$ is the intrinsic dissymmetry factor of the chiral europium complex, R is the reflectivity of the cathode, α is the attenuation factor taking into account light loss between the electrodes, x is the distance of the RZ from the anode (x = 0 on the anode, x = d on the cathode, see Figure A4-1).

Eq. (4-1) (plotted in Figure 4-3 with reasonable values of R and t_0 for the device A) suggests that a RZ as close as possible to the anode is optimal to preserve the polarization of emitted light. In fact, in this case, the attenuation of the backward emitted component (which undergoes reflection) is maximal, while the attenuation of the forward emitted component (which exits the anode window

without significant polarization loss) is minimized. In the presented devices with semitransparent cathode, the g_{EL} values can vary as much as 15-20 % as an effect of only the RZ position (roughly from ~0.63 to ~0.74). For the sake of comparison, in Table 4-2 we show the experimental g_{EL} values obtained for different architecture sorted by RZ position.

Table 4-2. experimental g_{EL} values obtained for different architecture sorted by RZ position and expected g_{EL} in the two limit cases (x = d and x = 0) as predicted by Eq. (4-1).

RZ near to the	**device**	**g_{EL}**	**Calc g_{EL}**
cathode	AIL/TCTA:OXD7 (D)	0.61	0.63
	AIL/TCTA	0.6	
anode	TCTA:OXD7/CIL (E)	0.88	0.74
	TCTA:OXD7	1/0.8[a]	

[a)] 100 nm active layer thickness.

Despite the simplicity of the model and its heuristic nature, these figures are consistently in qualitative agreement with our experimental observations (see Table 4-1 and 4-2).

Conclusions

In this Chapter, we have shown that by using electrode interlayer, it is possible to enhance the EQE of CP-OLEDs by 10 time and in the mean time obtain excellent polarization performances (up to 1.0). We have worked out a model which allows us to predict the reduction of g_{EL} values as a function of both the position of the RZ and the reflection of the cathode.

Conclusions of Part I

In this first part of this thesis, we have demonstrated that it is possible to obtain lanthanide complexes with outstanding chiroptical properties (in terms of g_{PL}) even with simple chemistry.

CPL of lanthanide complexes can be reliably studied in solid state, in deposition or in thin films. This kind of study is essential to switch to practical applications such as polarized electronic devices or futuristic CPL emitting security inks and labels based on chiral lanthanide complexes.

We have demonstrated that the polarization properties of chiral lanthanide complexes make them suited for chiral optoelectronic and photonic. Our proof-of-concept prototype showed that Ln-based CP-OLEDs can attain g_{EL}-s currently not achieved by polymer based devices.

This concept allows one to manufacture CP devices based on single molecule emitter with intrinsic highly polarized emission. This is in contrast to CP-OLEDs based on emitting polymers whose polarization stems from supramolecular chiral aggregates. Supramolecular aggregates may often suffer from high sensitivity to preparation conditions, leading to a certain batch-to-batch irreproducibility.

With our strategy, it is possible to prepare the devices by using common solution processing without the need of annealing or special treatment.

Despite the low EQE efficiency of our devices, there is much room for improvement. Lanthanides are phosphorescent emitters (several states with different multiplicities are involved in the emission and their excited state life-time can be of the orders of hundreds of miscroseconds or even milliseconds), so in principle the efficiency of Ln-based devices is not limited to singlet state emission (which implies EQE < 25 %).

The high polarization efficiency and the robustness (in terms of batch-to-batch reproducibility) of these OLEDs allowed us to test different device architectures in order to identify the major factors affecting the polarization inside the OLED.

We put forward a simple model to rationalize the experimental polarization losses that we observed. Despite its simplicity, such model allowed us to make predictions about the polarization efficiency of the device in strikingly qualitative agreement with the values found experimentally.

Our concept can be further extended, by employing tailored Ln complexes with enhanced luminescence and even higher dissymmetry factors. Moreover, it is possible to obtain CP-OLEDs emitting in different spectral region, by addressing different lanthanides, such as Tb for green emission and Tm and Yb for near infrared emission.

References

[1] E. G. Moore, A. P. S. Samuel , K. N. Raymond, *Acc. Chem. Res.*, **2009**, *42*, 542.
[2] J.-C. G. Bünzli , C. Piguet, *Chem. Soc. Rev.*, **2005**, *34*, 1048.
[3] J.-C. G. Bünzli , S. V. Eliseeva, *Chem. Sci.*, **2013**, *4*, 1939.
[4] C. Piguet, J.-C. G. Bünzli, G. Bernardinelli, G. Hopfgartner, S. Petoud , O. Schaad, *J. Am. Chem. Soc.*, **1996**, *118*, 6681.
[5] S. I. Klink, H. Keizer , F. C. J. M. van Veggel, *Angew. Chem. Int. Ed.*, **2000**, *39*, 4319.
[6] S. J. A. Pope, B. J. Coe, S. Faulkner, E. V. Bichenkova, X. Yu , K. T. Douglas, *J. Am. Chem. Soc.*, **2004**, *126*, 9490.
[7] C.-H. Huang, *Rare earth coordination chemistry: Fundamentals and applications*, John Wiley & Sons, 2010.
[8] J.-C. G. Buenzli, *Coord. Chem. Rev.*, **2015**, *293*, 19.
[9] J.-C. G. Bünzli, S. Comby, A.-S. Chauvin , C. D. B. Vandevyver, *J. Rare Earths*, **2007**, *25*, 257.
[10] C. P. Montgomery, B. S. Murray, E. J. New, R. Pal , D. Parker, *Acc. Chem. Res.*, **2009**, *42*, 925.
[11] J. Vuojola , T. Soukka, *Methods Appl. Fluoresc.*, **2014**, *2*, 012001.
[12] M. D. McGehee, T. Bergstedt, C. Zhang, A. P. Saab, M. B. O'Regan, G. C. Bazan, V. I. Srdanov , A. J. Heeger, *Adv. Mater.*, **1999**, *11*, 1349.
[13] R. C. Evans, P. Douglas , C. J. Winscom, *Coord. Chem. Rev.*, **2006**, *250*, 2093.
[14] U. Giovanella, M. Pasini, C. Freund, C. Botta, W. Porzio , S. Destri, *J. Phys. Chem. C*, **2009**, *113*, 2290.
[15] H. Xu, Q. Sun, Z. An, Y. Wei , X. Liu, *Coord. Chem. Rev.*, **2015**, *293*, 228.
[16] E. Klampaftis, D. Ross, K. R. McIntosh , B. S. Richards, *Sol. Energy Mater. Sol. Cells*, **2009**, *93*, 1182.
[17] J.-C. G. Bünzli , S. V. Eliseeva, *J. Rare Earths*, **2010**, *28*, 824.
[18] J. Andres, R. D. Hersch, J. E. Moser , A. S. Chauvin, *Adv. Funct. Mater.*, **2014**, *24*, 5029.
[19] G. Muller, *Dalton Trans.*, **2009**, 9692.
[20] F. Zinna , L. Di Bari, *Chirality*, **2015**, *27*, 1.
[21] F. Zinna, C. Resta, S. Abbate, E. Castiglioni, G. Longhi, P. Mineo , L. Di Bari, *Chem. Commun.*, **2015**, *51*, 11903.
[22] J. L. Lunkley, D. Shirotani, K. Yamanari, S. Kaizaki , G. Muller, *Inorg. Chem.*, **2011**, *50*, 12724.
[23] F. S. Richardson, *Inorg. Chem.*, **1980**, *19*, 2806.
[24] S. Petoud, G. Muller, E. G. Moore, J. Xu, J. Sokolnicki, J. P. Riehl, U. N. Le, S. M. Cohen , K. N. Raymond, *J. Am. Chem. Soc.*, **2007**, *129*, 77.
[25] M. Seitz, E. G. Moore, A. J. Ingram, G. Muller , K. N. Raymond, *J. Am. Chem. Soc.*, **2007**, *129*, 15468.
[26] H. Bauer, J. Blanc , D. L. Ross, *J. Am. Chem. Soc.*, **1964**, *86*, 5125.
[27] K. Binnemans, *Coord. Chem. Rev.*, **2015**, *295*, 1.
[28] A. P. Samuel, J. L. Lunkley, G. Muller , K. N. Raymond, *Eur. J. Inorg. Chem.*, **2010**, *2010*, 3343.
[29] R. S. Dickins, D. Parker, J. I. Bruce , D. J. Tozer, *Dalton Trans.*, **2003**, 1264.
[30] P. A. Tanner, *Chem. Soc. Rev.*, **2013**, *42*, 5090.
[31] J. P. Riehl , G. Muller, in *Comprehensive Chiroptical Spectroscopy*, eds. N. Berova, P. L. Polavarapu, K. Nakanishi , R. W. Woody, Wiley, 2012, vol. 1.
[32] H. G. Brittain , J. F. Desreux, *Inorg. Chem.*, **1984**, *23*, 4459.

[33] S. Aime, M. Botta, M. Fasano, M. P. M. Marques, C. F. Geraldes, D. Pubanz , A. E. Merbach, *Inorg. Chem.*, **1997**, *36*, 2059.
[34] L. Di Bari, G. Pintacuda , P. Salvadori, *J. Am. Chem. Soc.*, **2000**, *122*, 5557.
[35] L. Di Bari , P. Salvadori, *ChemPhysChem*, **2011**, *12*, 1490.
[36] Y. Haas , G. Stein, *Chem. Phys. Lett.*, **1972**, *15*, 12.
[37] G. Stein , E. Würzberg, *J. Chem. Phys.*, **2008**, *62*, 208.
[38] G.-L. Law, C. M. Andolina, J. Xu, V. Luu, P. X. Rutkowski, G. Muller, D. K. Shuh, J. K. Gibson , K. N. Raymond, *J. Am. Chem. Soc.*, **2012**, *134*, 15545.
[39] A. Beeby, I. M. Clarkson, R. S. Dickins, S. Faulkner, D. Parker, L. Royle, A. S. de Sousa, J. A. Gareth Williams , M. Woods, *J. Chem. Soc., Perkin Trans. 2*, **1999**, 493.
[40] O. Malta, H. Brito, J. Menezes, F. Gonçalves e Silva, C. de Mello Donegá , S. Alves Jr, *Chem. Phys. Lett.*, **1998**, *282*, 233.
[41] C. Freund, W. Porzio, U. Giovanella, F. Vignali, M. Pasini, S. Destri, A. Mech, S. Di Pietro, L. Di Bari , P. Mineo, *Inorg. Chem.*, **2011**, *50*, 5417.
[42] J. L. Lunkley, D. Shirotani, K. Yamanari, S. Kaizaki , G. Muller, *J. Am. Chem. Soc.*, **2008**, *130*, 13814.
[43] P. Schippers, A. van den Buekel , H. Dekkers, *J. Phys. E*, **1982**, *15*, 945.
[44] J. P. Riehl , F. S. Richardson, *Chem. Rev.*, **1986**, *86*, 1.
[45] S. D. Bonsall, M. Houcheime, D. A. Straus , G. Muller, *Chem. Commun.*, **2007**, 3676.
[46] T. Harada, Y. Nakano, M. Fujiki, M. Naito, T. Kawai , Y. Hasegawa, *Inorg. Chem.*, **2009**, *48*, 11242.
[47] T. Harada, H. Tsumatori, K. Nishiyama, J. Yuasa, Y. Hasegawa , T. Kawai, *Inorg. Chem.*, **2012**, *51*, 6476.
[48] J. Yuasa, T. Ohno, K. Miyata, H. Tsumatori, Y. Hasegawa , T. Kawai, *J. Am. Chem. Soc.*, **2011**, *133*, 9892.
[49] H. Tsumatori, T. Harada, J. Yuasa, Y. Hasegawa , T. Kawai, *Appl. Phys. Express.*, **2011**, *4*, 011601.
[50] O. Mamula, M. Lama, S. G. Telfer, A. Nakamura, R. Kuroda, H. Stoeckli-Evans, R. Scopelitti, *Angew. Chem.*, **2005**, *117*, 2583.
[51] M. Lama, O. Mamula, G. S. Kottas, F. Rizzo, L. De Cola, A. Nakamura, R. Kuroda , H. Stoeckli-Evans, *Chem. Eur. J.*, **2007**, *13*, 7358.
[52] G. l. Bozoklu, C. Gateau, D. Imbert, J. Pécaut, K. Robeyns, Y. Filinchuk, F. Memon, G. Muller , M. Mazzanti, *J. Am. Chem. Soc.*, **2012**, *134*, 8372.
[53] M. Cantuel, G. Bernardinelli, G. Muller, J. P. Riehl , C. Piguet, *Inorg. Chem.*, **2004**, *43*, 1840.
[54] R. Carr, N. H. Evans , D. Parker, *Chem. Soc. Rev.*, **2012**, *41*, 7673.
[55] N. H. Evans, R. Carr, M. Delbianco, R. Pal, D. S. Yufit , D. Parker, *Dalton Trans.*, **2013**, *42*, 15610.
[56] S. J. Butler, L. Lamarque, R. Pal , D. Parker, *Chem. Sci.*, **2014**, *5*, 1750.
[57] A. Moussa, C. Pham, S. Bommireddy , G. Muller, *Chirality*, **2009**, *21*, 497.
[58] S. Kirschner , I. Bakkar, *Coord. Chem. Rev.*, **1982**, *43*, 325.
[59] G. Pescitelli, L. Di Bari , N. Berova, *Chem. Soc. Rev.*, **2014**.
[60] R. Carr, L. Di Bari, S. Lo Piano, D. Parker, R. D. Peacock , J. M. Sanderson, *Dalton Trans.*, **2012**, *41*, 13154.
[61] C. P. Montgomery, E. J. New, D. Parker , R. D. Peacock, *Chem. Commun.*, **2008**, 4261.
[62] D. M. Dias, J. M. C. Teixeira, I. Kuprov, E. J. New, D. Parker , C. F. G. C. Geraldes, *Org. Biomol. Chem.*, **2011**, *9*, 5047.

[63] J. Yuasa, T. Ohno, H. Tsumatori, R. Shiba, H. Kamikubo, M. Kataoka, Y. Hasegawa , T. Kawai, *Chem. Commun.*, **2013**, *49*, 4604.
[64] D. G. Smith, B. K. McMahon, R. Pal , D. Parker, *Chem. Commun.*, **2012**, *48*, 8520.
[65] F. S. Richardson , T. R. Faulkner, *J. Chem. Phys.*, **1982**, *76*, 1595.
[66] L. Di Bari , P. Salvadori, *Coord. Chem. Rev.*, **2005**, *249*, 2854.
[67] S. Di Pietro, S. L. Piano , L. Di Bari, *Coord. Chem. Rev.*, **2011**, *255*, 2810.
[68] J. I. Bruce, D. Parker, S. Lopinski , R. D. Peacock, *Chirality*, **2002**, *14*, 562.
[69] S. Di Pietro , L. Di Bari, *Inorg. Chem.*, **2012**, *51*, 12007.
[70] S. Mason, *Molecular optical activity and the chiral discriminations.*, Cambridge University Press, 1982.
[71] S. Di Pietro, PhD program in Chemical Science PhD thesis, University of Pisa, 2012.
[72] E. Castiglioni, S. Abbate , G. Longhi, *Appl. Spectrosc.*, **2010**, *64*, 1416.
[73] C. Emeis , L. Oosterhoff, *Chem. Phys. Lett.*, **1967**, *1*, 129.
[74] H. P. Dekkers, C. Emeis , L. J. Oosterhoff, *J. Am. Chem. Soc.*, **1969**, *91*, 4589.
[75] C. A. Emeis , L. J. Oosterhoff, *J. Chem. Phys.*, **1971**, *54*, 4809.
[76] F. Zinna, U. Giovanella , L. Di Bari, *Adv. Mater.*, **2015**, *27*, 1791.
[77] F. Zinna, M. Pasini, F. Galeotti, C. Botta, L. Di Bari , G. Umberto, *Adv. Funct. Mater.*, **2016**, *in the press*, doi: 10.1002/adfm.201603719.
[78] R. Farshchi, M. Ramsteiner, J. Herfort, A. Tahraoui , H. Grahn, *Appl. Phys. Lett.*, **2011**, *98*, 162508.
[79] J. R. Brandt, X.-H. Wang, Y. Yang, A. Campbell , M. J. Fuchter, *J. Am. Chem. Soc.*, **2016**.
[80] G. Longhi, S. Abbate, G. Mazzeo, E. Castiglioni, P. Mussini, T. Benincori, R. Martinazzo , F. Sannicolò, *J. Phys. Chem. C*, **2014**, *118*, 16019.
[81] S. Abbate, G. Longhi, F. Lebon, E. Castiglioni, S. Superchi, L. Pisani, F. Fontana, F. Torricelli, T. Caronna , C. Villani, *J. Phys. Chem. C*, **2014**, *118*, 1682.
[82] E. Castiglioni, S. Abbate, F. Lebon , G. Longhi, *Methods Appl. Fluoresc.*, **2014**, *2*, 024006.
[83] V. Schurig, W. Bürkle, K. Hintzer , R. Weber, *J. Chromatogr. A*, **1989**, *475*, 23.
[84] D. Shirotani, T. Suzuki , S. Kaizaki, *Inorg. Chem.*, **2006**, *45*, 6111.
[85] J. Kumar, B. Marydasan, T. Nakashima, T. Kawai , J. Yuasa, *Chem. Commun.*, **2016**, *52*, 9885.
[86] L. Di Bari, G. Pintacuda, S. Ripoli , P. Salvadori, *Magn. Reson. Chem.*, **2002**, *40*, 396.
[87] S. Reineke, F. Lindner, G. Schwartz, N. Seidler, K. Walzer, B. Lüssem , K. Leo, *Nature*, **2009**, *459*, 234.
[88] S. Reineke, M. Thomschke, B. Lüssem , K. Leo, *Rev. Mod. Phys.*, **2013**, *85*, 1245.
[89] M. Grell , D. D. Bradley, *Adv. Mater.*, **1999**, *11*, 895.
[90] A. Bolognesi, C. Botta, D. Facchinetti, M. Jandke, K. Kreger, P. Strohriegl, A. Relini, R. Rolandi , S. Blumstengel, *Adv. Mater.*, **2001**, *13*, 1072.
[91] B. L. Feringa, *Acc. Chem. Res.*, **2001**, *34*, 504.
[92] C. Wang, H. Fei, Y. Qiu, Y. Yang, Z. Wei, Y. Tian, Y. Chen , Y. Zhao, *Appl. Phys. Lett.*, **1999**, *74*, 19.
[93] C. Wagenknecht, C.-M. Li, A. Reingruber, X.-H. Bao, A. Goebel, Y.-A. Chen, Q. Zhang, K. Chen , J.-W. Pan, *Nat. Photonics*, **2010**, *4*, 549.

[94] W. B. Sparks, J. H. Hough, L. Kolokolova, T. A. Germer, F. Chen, S. DasSarma, P. DasSarma, F. T. Robb, N. Manset, I. N. Reid, F. D. Macchetto , W. Martin, *J. Quant. Spectrosc. Radiat. Transfer.*, **2009**, *110*, 1771.
[95] Y. Yang, R. C. da Costa, M. J. Fuchter , A. J. Campbell, *Nat. Photonics*, **2013**, *7*, 634.
[96] B. Kunnen, C. Macdonald, A. Doronin, S. Jacques, M. Eccles , I. Meglinski, *Journal of biophotonics*, **2015**, *8*, 317.
[97] M. Oda, H. G. Nothofer, G. Lieser, U. Scherf, S. Meskers , D. Neher, *Adv. Mater.*, **2000**, *12*, 362.
[98] E. Peeters, M. P. Christiaans, R. A. Janssen, H. F. Schoo, H. P. Dekkers , E. Meijer, *J. Am. Chem. Soc.*, **1997**, *119*, 9909.
[99] Y. Geng, A. Trajkovska, S. W. Culligan, J. J. Ou, H. P. Chen, D. Katsis , S. H. Chen, *J. Am. Chem. Soc.*, **2003**, *125*, 14032.
[100] Y. Yang, R. C. da Costa, D. M. Smilgies, A. J. Campbell , M. J. Fuchter, *Adv. Mater.*, **2013**, *25*, 2624.
[101] A. de Bettencourt-Dias, *Dalton Trans.*, **2007**, 2229.
[102] J. Kido , Y. Okamoto, *Chem. Rev.*, **2002**, *102*, 2357.
[103] Z. Chen, F. Ding, F. Hao, M. Guan, Z. Bian, B. Ding , C. Huang, *New J. Chem.*, **2010**, *34*, 487.
[104] T. Canzler , J. Kido, *Org. Electron.*, **2006**, *7*, 29.
[105] S. Zhang, G. A. Turnbull , I. D. Samuel, *Org. Electron.*, **2012**, *13*, 3091.
[106] C. Rothe, L. Pålsson , A. Monkman, *Chem. Phys.*, **2002**, *285*, 95.
[107] Y. Zhang, C. Li, H. Shi, B. Du, W. Yang , Y. Cao, *New J. Chem.*, **2007**, *31*, 569.
[108] J. W. Huh, J. Moon, J. W. Lee, J. Lee, D.-H. Cho, J.-W. Shin, J.-H. Han, J. Hwang, C. W. Joo , J.-I. Lee, *Org. Electron.*, **2013**, *14*, 2039.
[109] G. Hass , J. Waylonis, *JOSA*, **1961**, *51*, 719.
[110] A. Castelli, F. Meinardi, M. Pasini, F. Galeotti, V. Pinchetti, M. Lorenzon, L. Manna, I. Moreels, U. Giovanella , S. Brovelli, *Nano Lett.*, **2015**, *15*, 5455.

Part II

Circularly polarized luminescence of single organic molecules

Chapter 5

Introduction to part II

In this second part, we shall address CP photoluminescence of single chiral organic molecules (SCOM). Unlike chiral lanthanide complexes, small molecules display intrinsic dissymmetry factor of the order of 10^{-4}–10^{-3}.[1] This is also in contrast with solution or solid state aggregates of chiral polymer or oligomers which sometimes can display g factors about 10^{-2},[2-4] and sometimes higher when cholesteric-like layers are formed.[5-7] An issue related to supramolecular aggregates is their high sensitivity to preparation conditions which often leads to batch-to-batch irreproducibility.[8] Another issues is the fluorescence quenching which occurs upon aggregation, especially in the case of H-type aggregates.[9]

Chiral non-aggregated organic molecules can display high quantum yields and high absorption coefficients, resulting in high brightness. Their emission band can be relatively broad with g factors usually constant throughout the band; as an additional advantage, their emission wavelength can be tuned through rational design and synthesis.[1]

The generally low dissymmetry factors are due to the fact that when strongly allowed electronic transitions are observed, $g_{\mathrm{PL}} = 4\frac{|\mathbf{m}_{ji}|}{|\boldsymbol{\mu}_{ij}|} \cdot \cos\theta_{\boldsymbol{\mu},\mathbf{m}}$ becomes vanishing small (see Chapter 1). Higher dissymmetry factors (around 10^{-2}) can be observed for electric dipole (formally) forbidden transitions. As already mentioned in General Introduction, the early experimental observations of CPL were carried out on the n→π* transitions of chiral ketones.[10,11]

Commonly, today CPL of SCOMs is observed for electric dipole allowed π→π* transitions either in molecules with intrinsically chiral fluorophores, such as helicenes and helicene-like molecules, in chirally perturbed planar chromophores, such as monomeric BODIPYs, or in exciton-coupled systems, such as

functionalized binaphthyls (see Scheme 5-1)[1] or BODIPYs dimers (see Chapter 6).

In the case of intrinsically chiral and chirally perturbed chromophores (and fluorophores), usually a single CPL band is observed. This band corresponds to the fluorescence stemming from the lowest singlet excited state. If the geometry of the emitting excited state is not significantly different from the ground state one, such band has the same sign of the most red-shifted Cotton effect (that is the CD of the same transition observed in absorption) and displays a g_{PL} similar to the absorption dissymmetry factor of the same CD transitions (g_{abs}):

$$g_{\mathrm{abs}} = \frac{A_L - A_R}{\frac{1}{2}(A_L + A_R)} = \frac{\varepsilon_L - \varepsilon_R}{\frac{1}{2}(\varepsilon_L + \varepsilon_R)} = \frac{\Delta\varepsilon}{\varepsilon} \qquad (5\text{-}1)$$

where A_L and A_R are the absorbance for left and right polarized light and similarly ε_L and ε_R are the molar extinction coefficients for the two circular polarizations.

In the case of exciton-coupled systems, the coupled excited state is split into a lower and a higher energy state. Light absorption gives rise to two ECD bands with opposite sign and equal amplitude, corresponding to electronic transitions from the ground state to the higher and lower excited state level (see Figure 5-1).[12] On the other hand, if the molecule follows Kasha's rule (see General Introduction), again only a single band from the lower excitonic level is expected (Figure 5-1). As in the case of intrinsically chiral fluorophores, the sign and the g_{PL} of such band should be compared with the lower energy component of the couplet in the ECD spectrum to look for potential differences in the geometry of the ground and excited state.

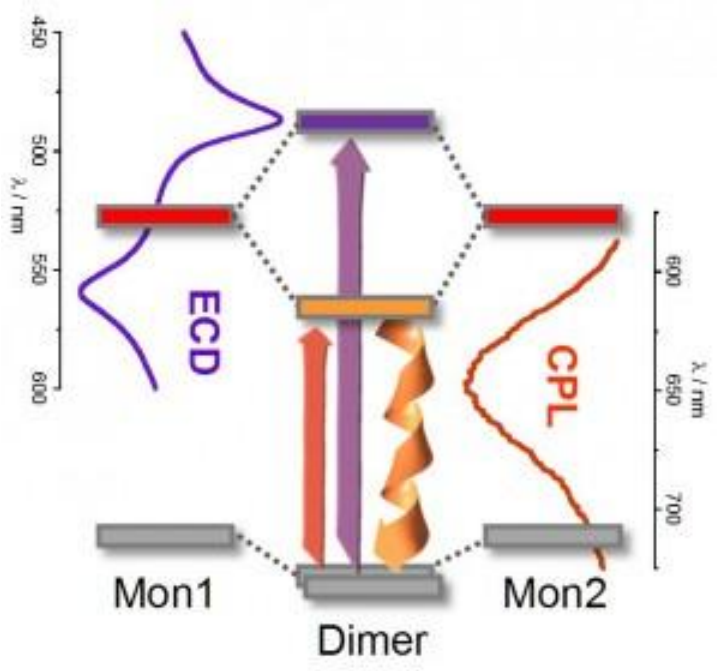

Figure 5-1. Origin of ECD and CPL bands in an exciton-coupled system.

At this point, it may be useful to put in context the relative polarization performances of the main classes of SCOMs, taking into account also their total emission properties. In analogy to the so-called *brightness* ($B_{\lambda_{exc}}$), which considers both quantum yield (φ) and molar extinction coefficient at a certain wavelength λ (ε_λ), we may define a *circular polarization brightness* (B_{CP}), including also the photoluminescence dissymmetry factor.

We define B_{CP} as:

$$B_{CP} = \varepsilon_\lambda \cdot \varphi \cdot \frac{g_{PL}}{2} = B_{\lambda_{exc}} \cdot \frac{g_{PL}}{2} \qquad (5\text{-}2)$$

Where the factor ½ is introduced to normalize g_{PL}.

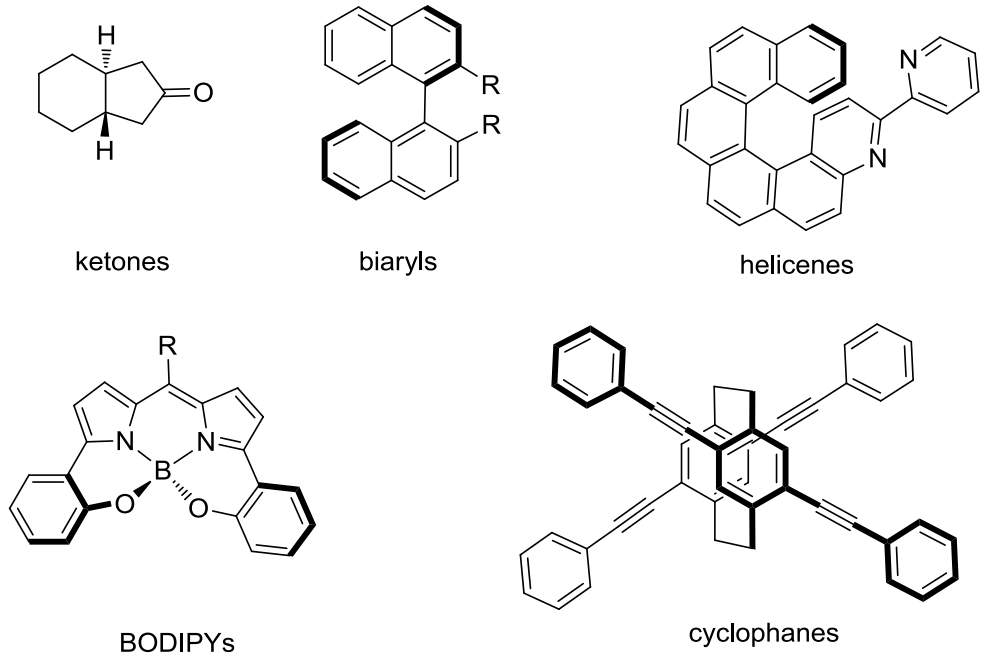

Scheme 5-1. Examples of compounds belonging to the most common classes of CPL SCOMs.

In Table 5-1, we report the B_{CP} values for some of the most studied classes of SCOMs (see Scheme 5-1 for some examples). As seen above, some chiral ketones display g_{PL} factors around 10^{-2} but very low quantum yields and absorption coefficients.[10,11] Biaryls, typically based on the binaphthyl scaffold, display lower g factors (10^{-3}) but much higher ε and φ.[13-16] Again, commonly reported helicenes,[17-22] simple chiral BODIPYs[23-27] and cyclophanes,[1,28] are endowed with B_{CP} spanning from 1 to 10^2. These values are mainly due to very high quantum yields and extinction coefficient, rather than to high g_{PL} (except in the case of some cyclophane displaying a g_{PL} up to $3 \cdot 10^{-2}$[28]).

For the sake of comparison, in the same Table, we report the B_{CP} values for two Eu complexes ($CsEu(hfbc)_4$[29] and $Eu(HFA)_3{}^{i}Pr\text{-}PyBox$,[30] see Chapter 1). In these cases, if the overall quantum yield is measured integrating on the whole transitions, B_{CP} should be multiplied by the branching ratio (β_i) of the selected

band. This is necessary in order to consider only photons emitted for a certain transition.

The branching ratio[31] can be estimated from the experimental spectrum as:

$$\beta_i = \frac{I_i}{\sum_j I_j} \qquad (5\text{-}2)$$

Where I_i is the integrated intensity of the transition considered and $\sum_j I_j$ is the summation over all the transitions observed.

Table 5-1. ε_λ, φ and g_{PL} and B_{CP} for the most common classes of SCOMs (see Scheme 5-1). The same values for two Eu compounds are reported for comparison.

Compound	ε_λ [a] **/M^{-1}·cm^{-1}**	**φ**	**g_{PL}**	**B_{CP}/M^{-1}·cm^{-1}**	**ref**
Ketones	10^1	10^{-3}–10^{-2}	10^{-2}	10^{-3}–10^{-4}	[10,11]
Biaryls	$1.5\cdot10^4$	~0.2	10^{-3}	~1	[13-16]
Helicenes	10^4	~0.3	$5\cdot10^{-4}$–10^{-3}	1−10	[17-22]
BODIPYs	$7.5\cdot10^4$	~0.5	10^{-3}	~20	[23-27]
Cyclophanes	10^5	0.5−0.8	10^{-3}–10^{-2}	10−10^2	[28]
$CsEu(hfbc)_4$	$3.5\cdot10^4$	0.03	1.38[b] (0.23)[c]	~60[b] (~70)[c]	[29,32]
$Eu(HFA)_3{}^i$Pr-PyBox	$3.5\cdot10^4$	0.4	0.46[d] (0.034)[e]	~220[d] (~220)[e]	[30]

[a] Estimated at the maximum absorption wavelength. [b] Values for the $^5D_0\rightarrow{}^7F_1$ transition (β = 0.08). [c] Values for the $^5D_0\rightarrow{}^7F_2$ transition (β = 0.6). [d] Value for the $^5D_0\rightarrow{}^7F_1$ transition (β = 0.07). [e] Values for the $^5D_0\rightarrow{}^7F_2$ transition (β = 0.9).

B_{CP} values reported in Table 5-1 are graphically represented in the bar chart in Figure 5-2.

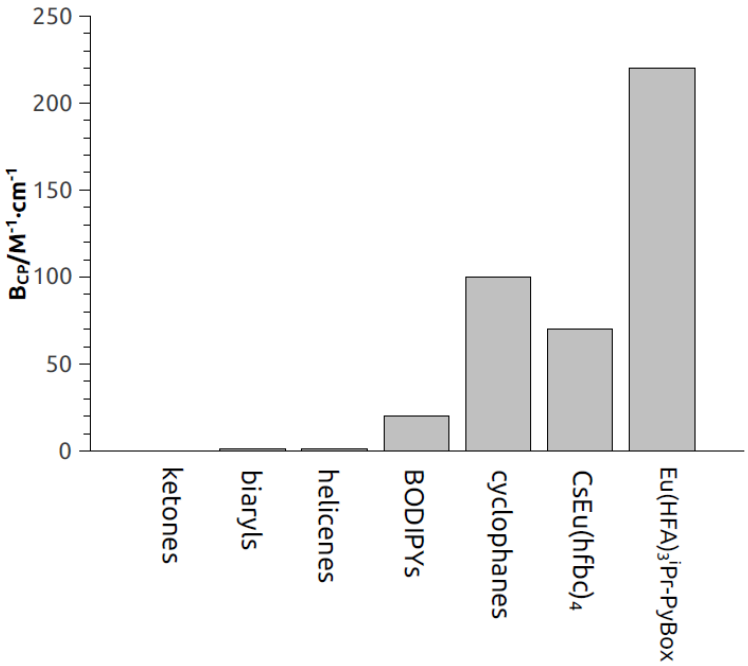

Figure 5-2. Bar chart representing B_{CP} values for the compounds listed in Table 5-1.

As shown in Table 5-1, most SCOM classes display, very low g_{PL} and overall low B_{CP}, if compared with lanthanide emitters or with aggregate organic molecules or macromolecules. Moreover, in most of the cases SCOM fluorescence is almost completely quenched in solid state. All these issues represent a severe obstacle for practical applications of SCOMs in CP-OLEDs or in fields where strongly polarized emission is required in solid state.

On the other hand, the study of CPL of SCOMs offers several advantages from a spectroscopic point of view. We could identify at least three cases.

- As already stated, CPL offers valuable information about the chirality of the excited state. Such information may be joined with *ab initio* calculations to elucidate the photophysics of the emission (see Chapter 6).[33]
- CPL is a complementary technique to both ECD and fluorescence. It could be applied to study interactions between fluorophores (even achiral

or racemic) with chiral environments, even when ECD or fluorescence give little or no information (see Chapter 7).[34]

- Thanks to the high sensitivity of chiroptical techniques to structural aspects, certain SCOMs may change their CPL as a response to some external stimuli (Chapter 8).[35]

In the case of SCOMs, where low g_{PL} factors are expected, CPL detection can not be carried out using static optics (i.e. polarizing filters). Dedicated instruments for CPL measurement (spectrofluoropolarimeters) employ the same high frequency photoelastic modulators used in ECD spectropolarimeters in order to detect small $I_L - I_R$ signals.[36-38] A brief description of our home-made spectrofluoropolarimeter will be given in Chapter 9.

Chapter 6

CPL of axially chiral BODIPY DYEmers

Introduction

As discussed in the previous Chapter, quantum mechanical calculations can guide the rational design of efficient CP fluorophores by means of the insight in the chirality of the excited state.

Boron dipyrrin derivatives (BODIPY, 4,4-difluoro-4-bora-3a,4a-diaza-s-indacene) are widely studied fluorophores due to their high absorption coefficients and high quantum yields which result in high brightness (see Chapter 5).[39,40] Moreover it is possible to finely tune their spectroscopic properties modifying the substituents on the pyrrole rings or on the boron atom. These features make them suitable to be employed in OLEDs (non polarized) or as light-emitting probes and bio-probes,[41] moreover, as described in Chapter 5, recently some research groups to develop chiral BODIPYs (or analogues[42]) capable of emitting circularly polarized light. In the present work, we studied the circularly polarized emission properties of BODIPY dimers (dubbed "DYEmers") **1** and **2** (Scheme 6-1). In the two enantiomeric pairs of atropisomeric dimers, the chirality is brought about by the chirality axis coincident with the bond connecting the two BODIPY monomers. This aspect strongly differentiates our system from the design of previously reported chiral BODIPYs.[26] Compounds **1** and **2** are quasi-isomers differing in the position of the aryl-aryl junction, namely C3/C3' (ring α atoms) in **1**, and C1/C1' (ring β' atoms) in **2** (Scheme 6-1). Perfect isomerism is broken by the replacement of two methyl groups in **1** by ethyl ones in **2**.

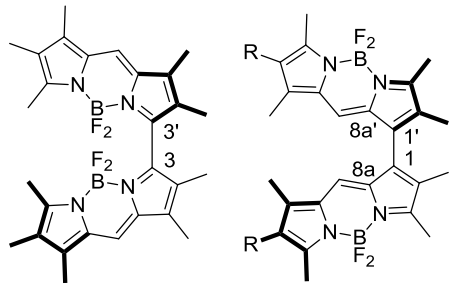

Scheme 6-1. Structures of quasi-isomeric BODIPY DYEmers **1** and **2**, and of model **2a**.

These compounds were synthesized and enantioseprated by the group of M. Bröring (University of Braunschweig).[43,44] These compounds display clear-cut exciton ECD couplets[45] in the long-wavelength region between 400 and 650 nm, allied with the first $\pi \rightarrow \pi^*$ transition of the BODIPY chromophore which is long-axis polarized (ECD spectra are reproduced in Figure 6-1 and Figure 6-2).

Compound **1** obeys the exciton chirality rule, therefore the (a*R*)-enantiomer, endowed with *M* chirality, shows a strong negative exciton couplet with an exceptionally large band splitting of 73 nm (0.33 eV). On the contrary, compound **2** violates the exciton-coupling rule, and the (a*R*)-enantiomer, endowed with *M* chirality, shows a weak positive exciton-couplet. The reason for such an apparent exception was found in the strong intrinsic transition magnetic dipole moments **m** allied with the discussed transition. The electric/magnetic or **μ-m** coupling has the same sign as the electric-electric **μ-μ** coupling for isomer **1**. On the contrary, the two couplings have opposite signs for isomer **2**, the **μ-m** one overwhelms the **μ-μ** one, and the couplet sign is reversed.[44,46] Such a situation is not unique to BODIPY DYEmers but still very infrequent.[46]

While the ground state chiroptical properties of compound **1** and **2** were fully investigated before,[44,46] a characterization of their excited states has not been reported yet. We decided to take advantage of our newly rebuilt spectrofluoropolarimeter (described in Chapter 9) to carry out the CPL measurements of **1** and **2**. The experimental results were corroborated by a

detailed computational investigation (In collaboration with G. Pescitelli, University of Pisa). In particular, it was interesting to study the CPL behaviour of compounds showing the peculiar exciton-coupled ECD spectra discussed above. It is interesting to study bis-chromophoric exciton-coupled compound, in fact there is much interest in CPL as a means for the detection and characterization of chiral supramolecular aggregates of chromophoric species, which are of course also exciton-coupled. In this context, CPL has demonstrated exceptional sensitivity to long-range couplings and has therefore been used as a probe of supramolecular structure, mode of aggregation, degree of disorder, and other properties.[47-50]

Results

Experimental emission and CPL spectra

Both compounds **1** and **2** are highly luminescent and therefore good quality emission and CPL spectra could be obtained. Our instrument (see Chapter 9), is capable to measure CPL and total florescence simultaneously. Emission and CPL spectra of **1** and **2** are shown in Figure 6-1, and the relevant numerical data are summarized in Table 6-1. Absorption and ECD spectra of **1** and **2** have been reported before.[44] They were re-measured and, together with the respective data, are reproduced in Figure 6-1 and Table 6-1 for a direct comparison with their emissive counterparts.

Compound **1** displayed a relatively strong CPL signal with a high signal-to-noise (S/N) ratio. The fluorescence band is Gaussian-shaped with a maximum around 655 nm, and it is retraced by the CPL spectra. A very large Stokes shift is measured, amounting to 95 nm (0.32 eV), confirming previous measurements on the same compound.[51] The Stokes shifts normally observed for monomeric unsubstituted BODIPY dyes are much smaller (10−15 nm). Our value surpasses those observed for purposely designed energy-transfer cassettes[39,40] and reaches those of similar BODIPY dimers.[51,52] The CPL spectra for the two enantiomers of **1** are mirror images, as expected (positive for (a*S*)-**1** and negative for (a*R*)-**1**),

with a $g_{PL} = \pm 3.8 \cdot 10^{-3}$. This value is similar to that reported for other chiral BODIPY derivatives,[23-27] and on the upper edge of the range reported for chiral non aggregated small organic molecules.[1] Moreover, its B_{CP} is ~70 $M^{-1} \cdot cm^{-1}$ (see Chapter 5), again comparable with the best performances of CPL SCOMs and higher than for monomeric BODIPYs (Table 5-1).

The comparison of the CPL with the ECD spectra shows that the most red-shifted Cotton effect (at 560 nm) has the same sign of the CPL spectrum (Figure 6-1). This appears to be a general behavior for ECD/CPL spectra of organic compounds, including all exciton-coupled systems investigated to date,[47,48,53] at least in cases where no substantial geometrical rearrangement occurs between the ground and excited state (see Chapter 5).[54]

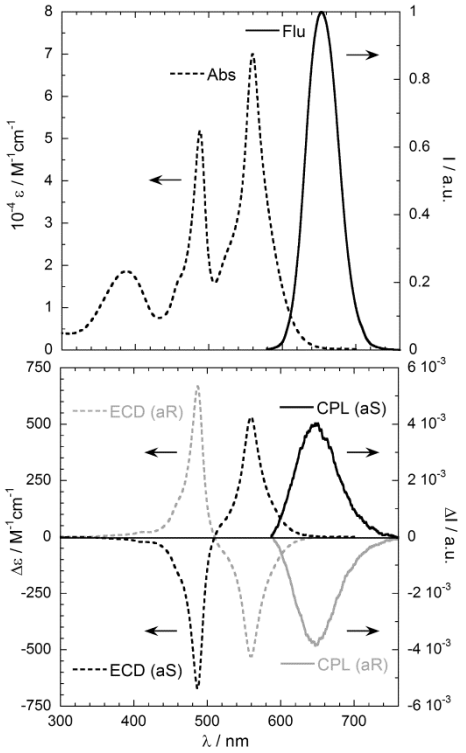

Figure 6-1. Experimental absorption and fluorescence spectra (top), ECD and CPL spectra (bottom) of compound **1**. The scale of the CPL is normalized to the maximum of emission, so that the g_{PL} values can be directly read on *y*-axis at the maximum of each curve. λ_{exc} = 517 nm.

Table 6-1. Spectroscopic experimental and computational data for compounds **1** and **2**.

Compound **1** (α,α dimer)

Experimental[a]			**Calculated TDDFT**[b]			**Calculated CC2**[c]		
Absorption	Emission	Stokes shift	Absorption	Emission	Stokes shift	Absorption	Emission	Stokes shift
560 nm (2.21 eV)	655 nm (1.89 eV)	95 nm (0.32 eV)	471 nm (2.63 eV)	545 nm (2.28 eV)	74 nm (0.35 eV)	480 nm (2.58 eV)	539 nm (2.30 eV)	59 nm (0.28 eV)
g_{abs}	g_{PL}		g_{abs}	g_{PL}		g_{abs}	g_{PL}	
$9.5\cdot10^{-3}$	$3.8\cdot10^{-3}$		$8.7\cdot10^{-3}$	$5.6\cdot10^{-3}$		$7.3\cdot10^{-3}$	$4.9\cdot10^{-3}$	

Compound **2** (β',β' dimer)

Experimental[a]			**Calc. TDDFT** (transoid conformer)[b,d]			**Calc. CC2** (transoid conformer)[b,d]		
Absorption	Emission	Stokes shift	Absorption	Emission	Stokes shift	Absorption	Emission	Stokes shift
552 nm (2.24 eV)	603 nm (2.05 eV)	51 nm (0.19 eV)	469 nm (2.64 eV)	521 nm (2.38 eV)	52 nm (0.26 eV)	477 nm (2.59 eV)	516 nm (2.40 eV)	39 nm (0.19 eV)
g_{abs}	g_{PL}		g_{abs}	g_{PL}		g_{abs}	g_{PL}	
$5.0\cdot10^{-4}$	$4\cdot10^{-4}$		$3.8\cdot10^{-4}$	$1.2\cdot10^{-4}$ [f]		$8.0\cdot10^{-4}$	$2.1\cdot10^{-4}$	
			Calc. TDDFT (cisoid conformer)[b,c]			**Calc. CC2** (cisoid conformer)[b,d]		
			Absorption	Emission	Stokes shift	Absorption	Emission	Stokes shift
			467 nm (2.66 eV)	528 nm (2.35 eV)	61 nm (0.31 eV)	478 nm (2.59 eV)	521 nm (2.38 eV)	43 nm (0.21 eV)
			g_{abs}	g_{PL}		g_{abs}	g_{PL}	
			$8.3\cdot10^{-4}$	$3.4\cdot10^{-4}$ [f]		$1.8\cdot10^{-3}$	$3.1\cdot10^{-4}$	

[a] In dichloromethane solution. Absorption and emission maxima are listed and Stokes shift estimated thereof. [b] M06-2X/def2-TZVP level in vacuo. [c] SCS-CC2/def2-SVP level in vacuo. [d] SCS-CC2/def2-TZVP level in vacuo. [e] Calculated on model **2a**. [f] Calculated sign is opposite to the experiment (see the text).

In addition to the g_{PL} value, the corresponding absorption dissymmetry factor (g_{abs}) should be considered.

It can be observed from Table 6-1 that g_{PL} and g_{abs} are roughly comparable for **1** (both in the order of 10^{-3}). This indicates that the phenomena responsible for the two chiroptical properties, namely absorption (ECD) and emission (CPL), are consistent with each other.

The experimental CPL spectra of compound **2** (Table 6-1 and Figure 6-2) shows a weaker signal by an order of magnitude than compound **1**, with a $g_{PL} = \pm 4 \cdot 10^{-4}$ (positive for (a*R*)-**2** and negative for (a*S*)-**2**). The Stokes shift is also smaller, although still very large, amounting to 51 nm (0.19 eV). Again, the sign and the magnitude of the g_{PL} are roughly comparable with the corresponding g_{abs} values and any effect of light re-absorption and circular dichroism on the CPL spectrum can be neglected.

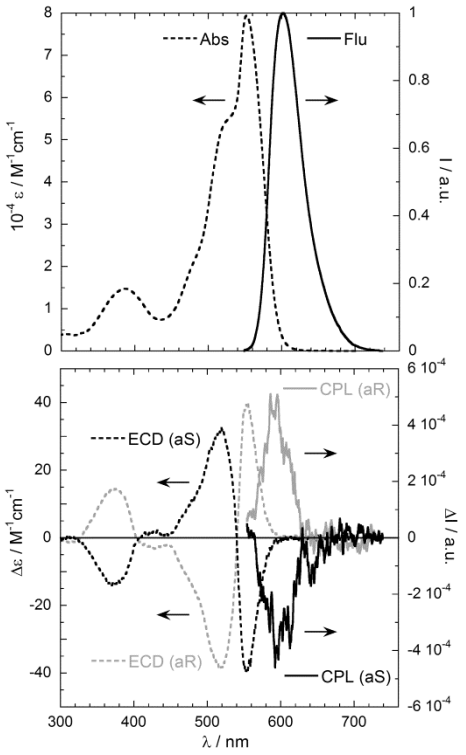

Figure 6-2. Experimental absorption and fluorescence spectra (top), ECD and CPL spectra (bottom) of compound **2**. The scale of the CPL is normalized to the maximum of emission, so that the g_{PL} values can be directly read on y-axis at the maximum of each curve. Note the different ECD and CPL scales with respect to Figure 6-1. λ_{exc} = 517 nm.

In particular, the CPL sign is consistent again with the sign of the most red-shifted ECD band, thus the apparent violation of the exciton chirality rule mentioned in the Introduction seems to be valid also for the emission. In the case of compound **2**, the fluorescence spectrum is slightly tailed towards long wavelengths,

suggesting the presence of two distinct emission bands; as we will discuss below, they are related to the contribution from different conformers. This compound shows a B_{CP} around 10 $M^{-1}\cdot cm^{-1}$, comparable with monomeric BODIPY.

Excited state and CPL spectra simulations

Extensive studies of the excited states of BODIPY dyes have been recently performed by Le Guennic, Jacquemin and co-workers.[55-57] From their studies, it appears that the time-dependent density functional theory (TDDFT) is able to reproduce absorption and emission sspectra of these compounds.

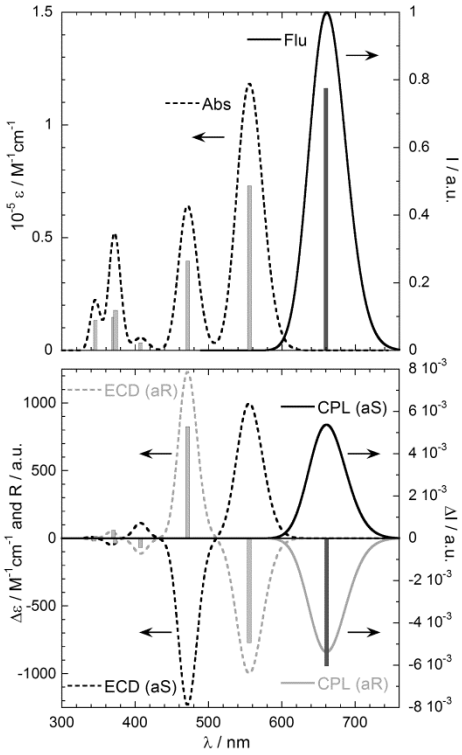

Figure 6-3. Calculated absorption and fluorescence spectra (top), ECD and CPL spectra (bottom) of compound 1. Calculations run at M06-2X/def2-TZVP level in vacuo, spectra generated as sums of Gaussians with σ = 0.1 eV, shifted by –0.4 eV. The scale of the CPL is normalized with the same procedure used for experimental spectra. Vertical bars represent oscillator and rotational strengths (in arbitrary absolute units).

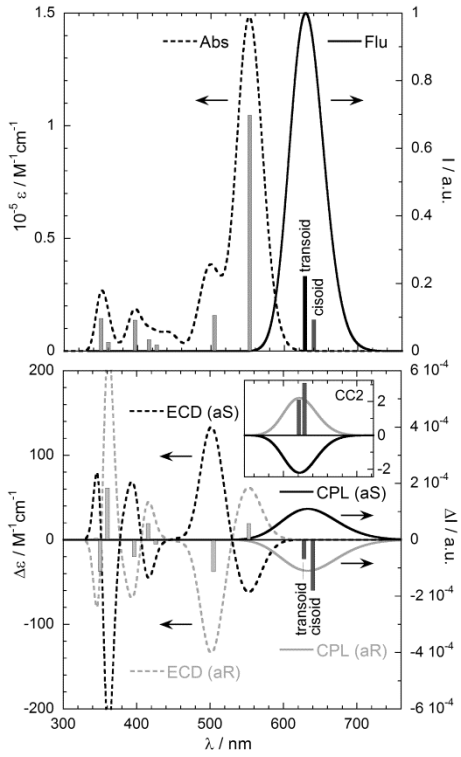

Figure 6-4. Calculated absorption and fluorescence spectra (top), ECD and CPL spectra (bottom) of model compound **2a**. Calculations run at M06-2X/def2-TZVP level in vacuo, spectra generated as sums of Gaussians with σ = 0.1 eV, shifted by –0.4 eV. The scale of the CPL is normalized with the same procedure used for experimental spectra. Vertical bars represent oscillator and rotational strengths (in arbitrary absolute units), shown only for the transoid conformer in the case of absorption and ECD spectra. Calculated spectra are the Boltzmann-weighted averages for the two conformers (cisoid and transoid), using populations estimated from relative free energies at 300 K. The inset shows CPL spectra calculated at CSC-CC2/def2-TZVP level in vacuo; the horizontal axis is aligned to the main axis, while the vertical axis is offset and the labels are 10^{-4} ΔI/a.u.

In Table 6-1 and Figure 6-3 and Figure 6-4, we show the results of the calculations performed at the M06-2X/def2-TZVP level (compound **2** is replaced here by the truncated model **2a**, Scheme 6-1), which confirm the already observed trends. M06-2X calculations reproduce very well both absorption and ECD spectra, apart from a systematic energy shift which amounts to 0.4 eV at the current level of calculation. For compound **1**, a single energy minimum is found with N-C3-C3'-N' dihedral of 105° (Figure 6-5, grey). The potential energy associated with the aryl-aryl torsional mode is a sharp curve with high barriers,

due to steric and electronic repulsion between the BF_2 groups and the 2/2'-CH_3 groups. For the other isomer, **2a**, such contacts are removed so that a larger torsional motion is allowed around the aryl-aryl axis. As a consequence, two shallow energy minima are obtained (Figure 6-6, grey) with C8a-C1-C1'-C8a' dihedral angles of 52° (cisoid conformer) and 128° (transoid conformer) separated by a barrier of less than 3 kcal/mol along a flat potential energy well (Figure 6-7, bottom curve).

All the computational procedures tested consistently predicted the cisoid conformer to be the more stable one according to internal energies, but the less stable according to free energies. On the basis of these latter values, the transoid conformer has a population of 80 % to 98 % at 300 K, depending on the method. An independent source of information, namely VCD spectra, confirms that the transoid isomer is largely dominant at room temperature.[27] Thus in this specific case, the calculated free energies appear to be more accurate than internal energies. Although this is expected in principle, it is not always true in practice, because of the inaccurate estimation of vibrational entropy terms associated with low-frequency modes.[51][52] Therefore, the calculated spectra for model **2a** shown in Figure 6-4 were obtained after a Boltzmann averaging based on free energies.

The DFT-optimized conformations of compounds **1** and **2a** can be checked against available X-ray structures, although it must be stressed that for flexible biaryls the X-ray geometries may sometimes largely differ from solution or gas-state ones.[55-57] For compound **1** no X-ray structure is available, however two 6,6'-di-*p*-tolyl analogues of **1** were considered for comparison.[51,58] They show N-C3-C3'-N' dihedrals in the range 92−97° and an overall arrangement similar to that calculated for **1**. The X-ray structure of compound **2** had been determined previously.[59] It features C8a-C1-C1'-C8a' dihedral angles of 46° and 51° (two independent molecules) which compare well with our calculated structure for the cisoid conformer (see Appendix B, Figure B6-1).

For both compounds **1** and **2** (or its model **2a**), experimental absorption and ECD spectra (Figure 6-1 and Figure 6-2) compare very well with simulated ones

(Figure 6-3 and Figure 6-4). In particular, the sign of the ECD couplet around 500 nm is reproduced by the calculations also for compound **2**, for which the exciton chirality rule fails as mentioned above and discussed previously.[44] A positive ECD couplet is experimentally found and consistently predicted by TDDFT for the (a*S*) enantiomer of compound **1** and the (a*R*) enantiomer of compound **2**. More interestingly, the calculated dissymmetry factors g_{abs} are also in excellent agreement with the experimental values for both compounds (see Table 6-1, where the transoid conformer should be considered for model **2a**).

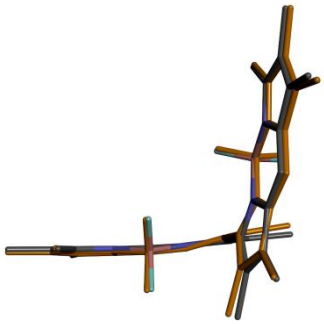

Figure 6-5. Overlap of ground state (grey) and excited state (orange) geometries calculated at M06-2X/def2-TZVP level for compound (a*R*)-**1**. Hydrogen atoms removed for clarity.

Figure 6-6. Overlap of ground state (grey) and excited state (orange) geometries calculated at M06-2X/def2-TZVP level for model compound (a*R*)-**2a** in the transoid (**a**) and cisoid (**b**) conformation. Hydrogen atoms removed for clarity.

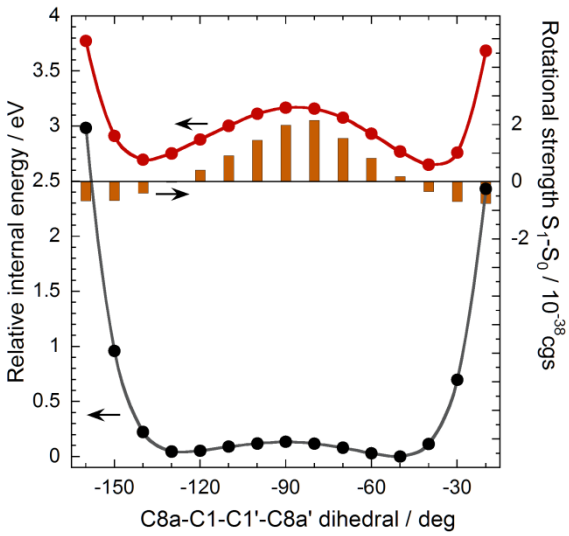

Figure 6-7. Torsional energy scans around the aryl-aryl axis for the ground state (lower black curve) and the first excited state (upper grey curve) for model compound (a*R*)-**2a**, and corresponding calculated rotational strengths for the excited-to-ground state emission (vertical bars). Each curve is the results of two non-relaxed scans run at M06-2X/def2-TZVP level using the transoid structures (depicted in Figure 6-6a) as starting geometries for dihedrals $< -90°$ and the cisoid structures (depicted in Figure 6-6b) as starting geometries for dihedrals $\geq -90°$. The internal energies relative to the lowest-energy structure (ground state cisoid conformer) are plotted.

The procedure to calculate CPL[60-65] emission is based on the optimization of the molecule in its first singlet excited state geometry, and on the evaluation of the excited states obtained thereof. Such a procedure has a general validity as it has been applied to various organic compounds, ranging from simple ketones and enones[61,63] to e.g. helicenes[18,62] and oligothiophenes.[65] Our calculations were run *in vacuo* at the already mentioned M06-2X/def2-TZVP level. As far as compound **1** is concerned, this procedure led to very satisfying results (Figure 6-3 and Table 6-1): the calculated Stokes shift is 0.35 eV, in excellent agreement with the experimental value of 0.32 eV; the predicted sign of the CPL band is in agreement with both the first calculated ECD band and the experiment, that is, positive for enantiomer (a*S*)-**1**; the computed value for g_{PL} is also very close to the experimental value (5.6 vs $3.8 \cdot 10^{-3}$). The good agreement confirms the validity of the current computational approach in a case devoid of any conformational

ambiguity. The excited-state geometry of compound (a*R*)-**1** is overlapped in Figure 6-5 (orange) with the ground-state one. Both BODIPY rings appear more distorted in the excited state as a consequence of two opposite forces, namely the propensity to augment conjugation (see the results for **2a** below) and the resulting steric contact between the BF_2 group on one ring and the 2-CH_3 group on the other ring. The relatively large difference between the ground and excited structures is one reason for the large Stokes shift.

The situation for compound **2** is much more complicated because of the rotational freedom. Two excited-state energy minima are obtained for model **2a**, again with cisoid and transoid conformation. In agreement with a known tendency of biaryl compounds,[66] this BODIPY dimer relaxes toward a more planar geometry in the first excited state. For the cisoid conformer, in fact, the C8a-C1-C1'-C8a' dihedral decreases from 52° to 40°, while for the transoid one, it increases from 128° to 136° (Figure 6-6, orange). In both the cases, the planarity of each ring is almost unaffected. In the excited state, the torsional energy curve shows two minima separated by a barrier as high as 10 kcal/mol (upper curve in Figure 6-7). Full optimization of the maximum-energy excited-state conformer (with C8a-C1-C1'-C8a' dihedral ~90°) lowers the barrier to about 7 kcal/mol, which is still high enough to prevent any transoid-to-cisoid conversion during the excited state lifetime. In this situation, we may assume that the two excited-state minima are populated in a measure proportional to the population of the respective ground state conformers.

Starting from the discussed excited-state geometries of model compound **2a**, TDDFT calculations were run using the same approach followed for compound **1**. The calculated Stokes shift for **2a** is 0.26 eV for the transoid conformer and 0.31 eV for the cisoid conformer. Taking into account the conformer populations discussed above, the overall simulated emission profile is a curve tailed toward the long wavelengths, similarly to the experimental one (Figure 6-2 and 6-4). The calculated Stokes shifts and g_{PL} values for the dominating transoid conformer turn out to be both very close to the experimental values (see Table 6-1). However, the

sign of the calculated CPL band is opposite to both the first calculated ECD band and the experimental CPL band. Thus, enantiomer (a*R*)-**2** shows a positive ECD couplet and positive CPL band, while the predicted CPL band for model (a*R*)-**2a** is negative. This inconsistency occurs for both conformers. Thus, the TDDFT-based computational approach fails to reproduce the CPL spectrum of compound **2** when the recommended M06-2X functional is employed.

In the attempt to improve the results of TDDFT calculations we first tried other functionals, namely CAM-B3LYP and ω-B97XD, which are known to be very accurate in the calculations of chiroptical properties.[67] Both CAM-B3LYP/def2-TZVP and ω-B97XD/def2-TZVP calculations however predicted again the wrong sign for the critical CPL band. Next, M06-2X/def2-TZVP calculations were performed including a solvent model for dichloromethane.[68] The results obtained were very similar to those *in vacuo*, apart from a small bathochromic shift. Similarly, representative calculations run on the whole compound **2**, rather than on its model **2a**, did not solve the problem.

Therefore, the entire set of calculations was run at SCS-CC2 level of theory, employing DFT- and TDDFT-optimized geometries for ground and excited-state SCS-CC2 calculations, respectively, and using the def2-SVP and def2-TZVP basis sets for compounds **1** and **2a**, respectively.

The results of SCS-CC2 calculations on compounds **1** and **2a** are summarized in Table 6-1. The agreement between SCS-CC2 theory and experimental data is as good as TDDFT for compound **1**, and slightly better than TDDFT for compound **2** (and its model **2a**) in terms of relative transition energies (Stokes shift) and *g*-values. Most importantly, the calculated CPL spectrum for compound **2a** has now the correct sign in keeping with the experiment, namely the predicted CPL band for model (a*R*)-**2a** is positive (see inset in Figure 6-4). The present inconsistency between TDDFT and coupled-cluster calculations is, to the best of our knowledge, unprecedented in the context of CPL.

At this point we may ask whether there are any specific reasons for the failure of the three different hybrid functionals (M06-2X, CAM-B3LYP and ω-B97XD)

employed for compound **2**. This failure seems to be strictly related to the intrinsic non-robustness of the CPL band measured on **2** and calculated on **2a.** Where the prediction of chiroptical properties is concerned, an estimation of the robustness of calculations (and of the corresponding measurements) is possible by evaluating the angle ξ between the calculated electric and magnetic dipole moments **μ** and **m**.[69,70] All the chiroptical properties are in fact allied with the rotational strength, defined as the scalar product between **μ** and **m**. The larger is the deviation of ξ from 90°, the more robust is the prediction of the rotational strength. In the case of $S_1 \rightarrow S_0$ emission calculations for (*R*)-**2a**, the angle ξ between the electric and magnetic dipole moments is between 87° and 93° for both transoid and cisoid conformers, very close to 90°, i.e. the value where the rotational strength vanishes. In comparison, the corresponding ECD band for the S_0-S_1 excitation of (*R*)-**2a** is much more robust, with ξ angles between 75° and 81°. The situation is much less critical in isomer **1**, for which both ECD and CPL bands appear very robust with ξ angles are ~132° and 123°-125°, respectively.

A second reason for the weak CPL band of the BODIPY DYEmer **2**, which concurs with the previous discussed one, is related to the conformational flexibility. In fact, the sign and intensity of the predicted CPL band for model **2a** at M06-2X/def2-TZVP level depend on the aryl-aryl torsion as shown in Figure 6-7 (vertical bars). For the enantiomer (a*R*)-**2a**, the band is negative and small for the transoid excited-state minimum with C8a-C1-C1'-C8a' dihedral of –136°, however it vanishes around –130° and is positive at –120°. A similar situation occurs for the cisoid conformer: the band is negative and small for a C8a-C1-C1'-C8a' dihedral of –40°, but it turns to positive already at –50°. Thus, this CPL band is also non-robust with respect to small geometrical distortions. In particular, it vanishes and changes sign within each of the two energy wells associated with the excited-state minima for the aryl-aryl torsional mode. In the ground state, conversely, the predicted first ECD band is always positive for (a*R*)-**2a** along a large portion of the torsional energy curve. A pronounced dependence of CPL on the aryl-aryl torsion has been reported for other biaryls, for example 1,1'-binaphthyl derivatives.[71-73] In the present situation, it is also

likely that the dependence of the magnetic and electric transition dipoles on the torsional motion cannot be disregarded. The introduction of such effect with a fully quantum approach cannot be accomplished at a pure electronic level and it would require the inclusion of vibronic contributions beyond the Franck-Condon approximation.[74-76]

Conclusions

With our current experimental set-up, it is possible to record CPL spectra with excellent signal-to-noise ratio and to reliably measure signals at least down to $g_{PL} \approx 10^{-4}$.

The results presented in this chapter shows that for compound **1**, which exists as a single minimum in both the ground-state and excited-state, it is possible to accurately reproduce the features of both the ECD and CPL spectra (including the absorption and emission dissymmetry factors), using a consolidated calculation method based on the M06-2X functional recommended for BODIPY's. On the other hand, compound **2** is associated with weaker ECD and CPL spectra, and it is endowed with large flexibility in both the ground and excited states. In this case several functionals failed to reproduce the sign of the CPL spectra. In our interpretation, the failure of the such methods is due to two concomitant factors. First, a peculiar combination of electric/electric and electric/magnetic exciton-couplings makes the rotational strength intrinsically non-robust for **2**. Second, the calculated CPL band is very sensitive to the excited-state conformation and it varies from one sign to another for geometries close to the predicted excited-state minimum.

Chapter 7

A pH responsive helicene based CPL switch

Introduction

In this Chapter an example of SCOM-based chiroptical switch will be presented.

Despite low g_{PL} and moderate overall B_{CP}, helicenes are versatile chiral scaffold lending themselves to a wealth of chemical transformation,[77] such as modifying the number of condensed rings and the nature of substituents, inserting etheroatoms into the main skeleton and even binding them to *d*-metals.[78] In this way it is possible to obtain chiral molecules with a considerable variation in their optical properties both in absorption and in emission. Through carefully tailored design, several research group reported helicenes able to change their ECD response upon various stimuli,[21] such as pH[20,79] or temperature variations,[80] ionic interactions[81,82] or redox transformations.[83-86]

In this context, the group of J. Lacour synthesized a zwitterionic diaza [4]helicene (**1**, Scheme 7-1), following the procedure reported in references [22] and [35]. The presence of a carboxylic moiety has two effects.[35]

- It enhances its solubility in aqueous media: **1-H** (Scheme **7-1**) has a water solubility up to 10^{-4} M (100 mg·L^{-1}); 4.10^{-4} M, for form **1** (400 mg·L^{-1}).
- Upon protonation-deprotonation in acid/basic media (HCl/NaOH in water, HBF_4 or Et_3N in acetonitrile), the compound changes significantly its optical properties.

The absorption maximum of the visible band undergoes a blue shift by 25 nm in water, and by 36 nm in acetonitrile, allowing a visual detection of pH change (see Table **7-1** and Figure **7-1**, bottom). Moreover, deprotonation of **1-H** is accompanied by a dramatic quench of the fluorescence (Table **7-1**, Scheme **7-1**, Figure B7-1).

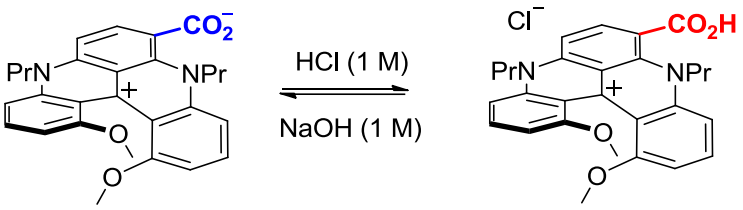

1 **1-H**

Scheme 7-1. Strucuture of the zwitterionic diaza [4]helicene in both deprotonated (**1**) and protonated (**1-H**) forms. Only *P* enantiomer is shown.

Table 7-1. Optical properties and B_{CP} values for compound **1** and **1-H** in acetonitrile and water.[35]

Dye	solvent[a]	λ_{max} / nm (ε_{max} / $M^{-1}\cdot cm^{-1}$)	λ_{em} / nm	Φ[b]	B_{CP}
1	CH_3CN	626 (10400)	709	0.01	/
1	H_2O	612 (11300)	690	0.02	/
1-H	CH_3CN	590 (11300)	654	0.29	1.6
1-H	H_2O	587 (11700)	675	0.10	0.6

[a)] In CH_3CN in presence of HBF_4 or Et_3N; in H_2O in presence of HCl or NaOH. [b] Relative to Cresyl Violet (Φ = 0.54 in MeOH); estimated error = ±10 %.

Beside optical properties, chiroptical properties changes as a function of pH as well.

ECD spectrum of the cationic species **1-H** displays a maximum around 300 nm ($\Delta\varepsilon \approx 50\ M^{-1}\cdot cm^{-1}$), while the deprotonated form **1** displays no Cotton effect at this wavelength (Figure 7-1, top). This behaviour was found to be fully reversible over several protonation-deprotonation cycles (inset of Figure 7-1).

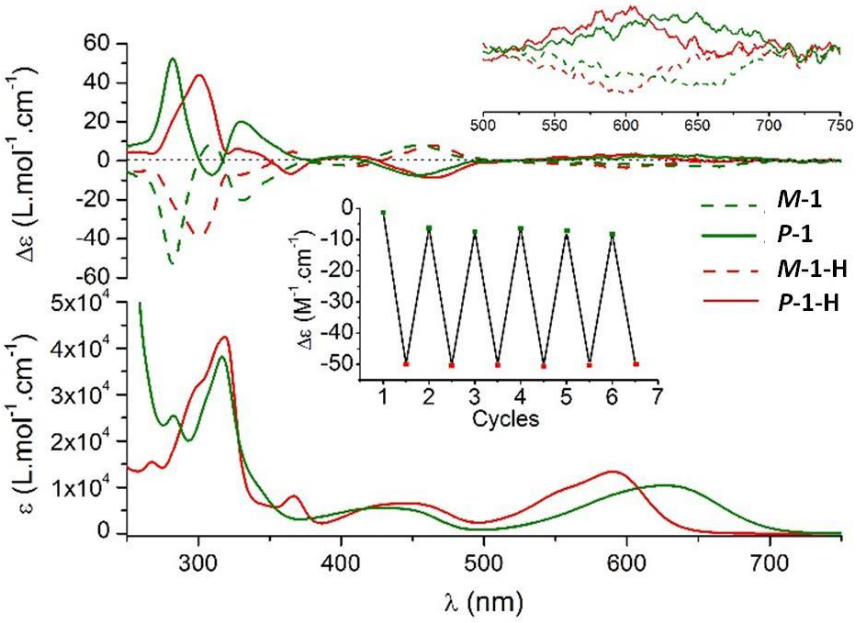

Figure 7-1. Top: ECD spectra (10^{-5} M) of *M*-**1-H**, *P*-**1-H** (CH_3CN/HBF_4) and *M*-**1**, *P*-**1** (CH_3CN/ Et_3N). **Bottom:** absorption spectra of **1-H** (red) and **1** (green) in CH_3CN. **Insert:** reversibility of pH-switching monitored at 300 nm for *M*-**1**/**1-H**

Results

Given the significant chiroptical switch behaviour seen in the ECD spectra and given the remarkably different fluorescence properties of the two species, it was interesting to investigate their CPL response.

Enantiomers *P*-(+) and *M*-(–) of **1-H** in acidic acetonitrile solution (HBF_4 1 M) displayed weak monosignate CPL signals with a maximum at ~650 nm (Figure 7-2), as expected from the fluorescence spectra. The signs of the bands for the two enantiomers are in agreement with the sign of the most red-shifted Cotton effect, *i.e.*, the bands centered at 600 nm in the ECD spectrum (Figure 7-1, top). The g_{PL} factor was estimated to be $5 \cdot 10^{-4}$ in water and acetonitrile, however since the compounds are much more emissive in acetonitrile, the CPL spectra display a higher S/N ratio (see Figure B7-2 for CPL spectra in water). These values are very similar to the absorption dissymmetry factors at 600 nm estimated from the

CD spectrum ($g_{abs} = 4 \cdot 10^{-4}$). This indicates that there is no significant geometry change between the ground electronic state and the emitting excited state. Moreover, the measured g_{PL} factors are in agreement with those previously reported for organic compounds.[1,17] The narrow range of concentration investigated ($1-5 \cdot 10^{-5}$ M) did not appear to change significantly the normalized intensities of the spectra. Owing to insufficient emission in basic medium, it was not possible to record any significant CPL signal for zwitterion **1**, thus validating the ON/OFF CPL switching between the two species. BCP of compound **1-H** in acetonitrile is comparable to the values of other helicenes. As expected, B_{CP} in water was lower due to poor total quantum yield (Table 7-1).

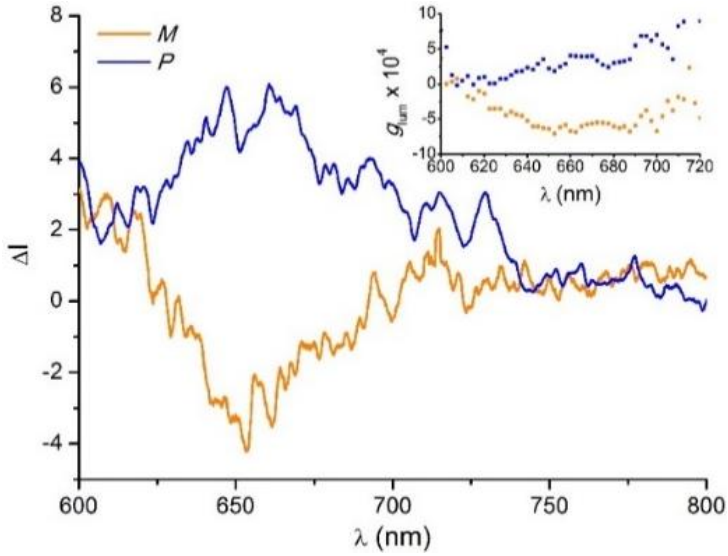

Figure 7-2. CPL spectra and gPL response (inset) of the two enantiomers of **1-H** in acidic acetonitrile solution (HBF_4 1 M). λ_{exc} = 517 nm

Conclusions

In this Chapter, we have presented the first report of ON/OFF CPL switching of a helicene derivative upon an external bias such as pH. Moreover, it is worth stressing that such compound displays CPL emission in the red region, which is

of first importance, for instance, in bio-imaging applications, as biological tissues are more transparent to long wavelength radiation.

Chapter 8

CPL to reveal interaction between fluorescent stains and protein-based matrices used in paintings

Introduction

Painters from all the periods and across the globe relied on a wide range of organic substances as painting materials, such as oils, saccharide gums, terpenoid resins and proteinaceous materials. The development of specific methods for the stratigraphic localization and identification of these materials in paint samples is one of the most important steps to understand the painting techniques, to highlight degradation phenomena, to identify the best conservation conditions and to prevent considerable damage brought on by misguided restoration interventions on painted artworks.[87]

Today, the stratigraphic localization of proteinaceous materials in art samples is still relatively arduous.[88,89] Following a common technique, the sample is mounted on a *cross-section*, after embedding it in a synthetic resin, which is subsequently polished in order to expose the sample stratigraphy. Cross-sections can then be analyzed by imaging techniques based on magnetic resonance, mass spectrometry or optical spectroscopies[89] such as Raman microscopy.[90,91] For proteins, one may take advantage of staining methods using visible or fluorescent dyes. Such methods do not require specific instrumentation or complex sample handling and are very appealing to non-specialized conservation laboratories.[89,92,93] These dyes may be coupled to immunochemical assays, for obtaining a selective detection of specific epitopes.[94-98] However, proteins can undergo severe changes within the complex matrix of a paint upon (very) long term exposure to the changeable and sometimes harsh environment, where the artwork is displayed or stored.[93,99-102] Degradation processes of proteinaceous binders include oxidation and deamidation, partial hydrolysis, crosslinking, formation of aggregates and complexes with other organic binders and inorganic

pigments and fillers.[103,104] As a consequence, antibodies selected to recognize native proteins may fail localizing degraded proteins or their aggregates in aged paint cross-sections. On the other hand, there is a wide variety of low molecular weight dyes, developed to reveal proteins or peptides non specifically, by visual inspection, through colour or fluorescence on/off.

We may distinguish between covalent[105-107] and non-covalent dyes,[93,108,109] depending on the type of interaction they establish with the protein or the peptide.

For the localization of proteinaceous binders in paint cross sections, one may use common fluorescent protein gel stains, although false negatives and positives have been reported.[109] Before moving to practical applications, these cases should be understood and a rational understanding of success and failure in these assays should be provided. To this end, we propose to enrich more traditional investigation techniques[110] with circularly polarized luminescence, which has proven a valuable tool to investigate the interaction between fluorophores and chiral environments.

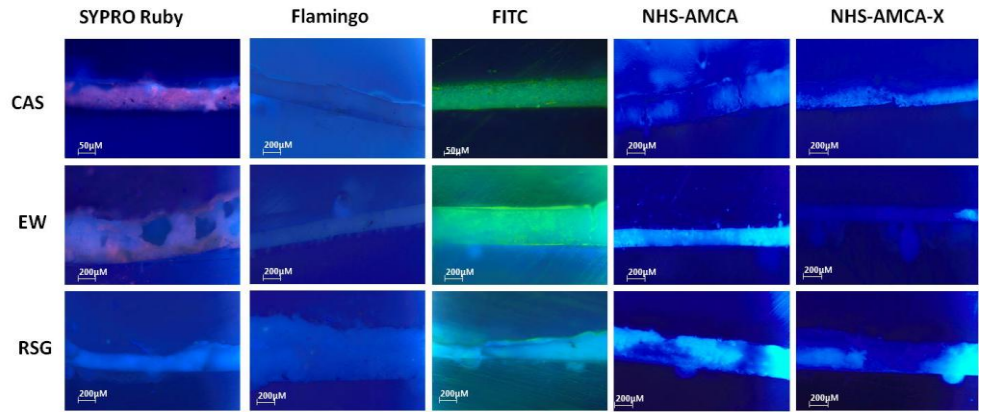

Figure 8-1. Visible fluorescence microscopy images of cross sections of a **CAS** matrix (top row), **EW** (middle row) and a **RSG** (bottom row) matrix, stained with SYPRO Ruby (first column from the left), Flamingo (second column), FITC (third column), NHS-AMCA (fourth column) and NHS-AMCA-X (fifth column) under UV (λ_{exc}=365 nm) light.

As discussed in Chapter 5, chiroptical spectroscopies are a well known tool to monitor the interaction between a small achiral or racemic molecule to a chiral guest such as proteins or DNA.[111] Chiroptical techniques are particularly beneficial when complex systems are involved, thanks to the specificity of the

chiroptical response. Most commonly, electronic circular dichroism (ECD) is used to this purpose,[111] since induced ECD can be an extremely powerful way to reveal and follow small molecule-protein binding. On the other hand, as extensively detailed in the previous Chapters, CPL can be used as well if the excited state is chirally perturbed.

The aim of this work is to study the interaction of selected fluorescent stains with the proteins contained in real painting matrices.

We propose a straightforward method based on CPL to complement more common techniques. Our long term goal is to provide a rational approach to the development of successful and simple fluorescent stains, to understand scopes and limitations of protein staining in painting cross-sections and to put forward an improved, reliable and robust methodology for restorers.

Results

For the reasons given above, in order to obtain a realistic insight, we had to employ products of the typical grade which would actually be employed in painting practice, together with some commercial fluorescent stains. We screened five widespread stains (Scheme 8-1), which are normally used to reveal denatured proteins or peptides,[108,109,112] mainly on gel electrophoresis, and three relevant protein-based substrates, namely dried egg white (**EW**) based on ovalbumin, casein (**CAS**) from dried cow milk, and rabbit skin glue (**RSG**) based on partially hydrolysed collagen. As a standard reference we used a purified protein (chicken egg ovalbumin, **OVA**).

In a first screening of cross sections containing our three different model proteinaceous binders (**CAS**, **RSG** and **OVA**) we observed remarkably different responses from the five stains. In , we report the fluorescence microscopy images of cross-sections prepared with the three proteins after staining with the fluorophores reported in Scheme 8-1. SYPRO Ruby (**1**) and FITC (**3**) give **CAS** and **EW**-containing cross-sections a characteristic red (in the case of staining

agent **1**) and green (in the case of **3**) fluorescence (Figure 8-1), while no staining emission is visible with **RSG**. NHS-AMCA (**4**) and NHS-AMCA-X (**5**) give blue fluorescence with the three proteins, while flamingo (**2**) does not give any fluorescence with any of the samples.

In this work, for the first time, we exploited CPL to signal the interaction of some of these commercial achiral (or racemic) fluorophores with common painting grade protein-based matrices. These results are complemented with the affinity constants of the fluorescent stains obtained by fluorescence titrations in aqueous solution.

SYPRO Ruby **1** and Flamingo **2** (Scheme 8-1) are known to bind *denatured* proteins *on a gel*, and were recently proposed to localize proteins in paint cross sections.[93,113] Both **1** and **2** are only weakly emissive in aqueous solution (Tris buffer, pH 7.2), while they become brighter upon irradiation with 365 nm UV-B light when they interact with certain proteins, peptides or some proteinaceous material.

In the presence of **CAS**, **EW** and **OVA**, **1** yields red luminescence, which allowed us to carry out titration experiments, monitoring its total fluorescence. The results are displayed in Table 8-1. On the contrary, **RSG** did not induce any luminescence enhancement at any mole ratio. A similar behaviour is also observed for the Flamingo stain (**2**). **2** shows very weak fluorescence when it is alone in aqueous solution, but the binding with **CAS**, **EW** and **RSG** leads to an increase of the fluorescence intensity upon addition of proteins. Moreover, an increase of the protein content generates a shift in the fluorescence emission maximum to lower wavelengths, from 550 nm of **2** alone to 535 nm with **CAS**, 536 nm with **EW** and 543 nm with **RSG**. These changes further confirm the interaction between **2** and the three proteins.

Table 8-1. A summary of the emission spectra characteristics of Sypro Ruby and Flamingo with proteins and the association constants (K_b). The association constants (K_b) were determined by Eq. (B8-10), see Appendix B. $\Delta\varphi$ is defined in Eq. (B8-6).

	Sypro Ruby			**Flamingo**		
Proteinaceous materials	Emission maximum [nm] (λ_{ex} 470 nm)	$\Delta\varphi$ [M^{-1}] saturating level	K_b	Emission maximum [nm] (λ_{ex} 490 nm)	$\Delta\varphi$ [M^{-1}] saturating level	K_b
Without proteins	603			550		
CAS	603	$5.8\cdot10^{7}$	$3.1\cdot10^{5}$	535	$6.1\cdot10^{8}$	$1.1\cdot10^{5}$
EW	603	$4.1\cdot10^{7}$	$5.2\cdot10^{4}$	536	$7.1\cdot10^{8}$	$2.6\cdot10^{5}$
RSG	603	$4.8\cdot10^{6}$	–	543	$2.5\cdot10^{8}$	$9.5\cdot10^{3}$
OVA	603	$7.2\cdot10^{7}$	$2.5\cdot10^{5}$			

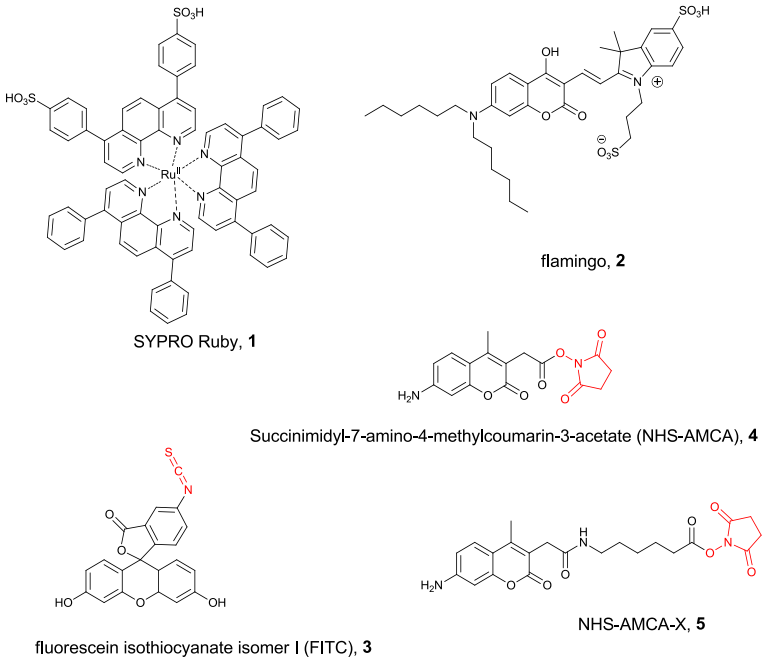

Scheme 8-1. Structures of the fluorescent stains studied in this work. The reactive moieties of the covalent stains are highlighted in red.

In order to compare quantitatively the binding affinity of stains **1** and **2** with the proteins, we determined the association constant values (K_b) by monitoring the

changes of emission at the maximum band position with increasing concentration of proteins. The constants K_b, determined by a modified Hildebrand and Benesi equation, are reported in Table 8-1.

The comparison of the K_b values obtained for **1** and **2** shows that there are very large differences between these two stains: **1** has strong affinity for **CAS** and **OVA** and only to a much lesser extent to **EW**, while it does not bind to **RSG**. The large differences between **EW** and the purified protein **OVA** indicate that the latter may not be a satisfactory model for the complex **EW** and therefore a study of the real complex matrix is mandatory to understand the interaction of the stains and the proteins in real samples.

On the contrary, **2** prefers **EW** and **CAS** over **RSG**. Interestingly, in cross-sections no fluorescence was visible, suggesting that in the solid phase different phenomena might take place, such as quenching of fluorescence, or the binding site of the protein is not available when not in solution.

These quantitative data deserved further insight and we proceeded to chiroptical measurements. In the first place, we resorted to ECD spectroscopy in the visible range, aiming at the detection of induced ECD of the dye-centred absorption bands.

In this context, we should notice that **1** is the racemic mixture of a (*tris*(phenanthroline)Ruthenium(II) disulfonate),[114] which stems from the octahedral coordination of Ru(II) ion with the bidentate ligand (phen) enabling two enantiomeric configurations, (Δ) and (Λ).

On the contrary, Flamingo (**2**) is *achiral*, as well as all the other dyes (shown in Scheme 8-1) that we shall discuss below.

For a racemic molecule like **1**, ECD may arise only if: a) one of the two enantiomers interacts more strongly than the other with the protein *and at the same time* this interaction induces significant changes in the ECD spectrum of the bound species compared to the free one; b) if both enantiomers bind to a similar extent but in different sites, such that the ECD spectra of the two become different

and no longer cancel out (as it would normally occur in the absence of the protein).[29]

In our case, we could detect no ECD signal in the region of **1** absorption (around 450 nm), therefore we must exclude both possibilities. Moreover, we monitored the protein UV-ECD spectrum as well, but we could not detect significant changes. This reveals that the binding event does not cause any secondary structure change in the protein.[115]

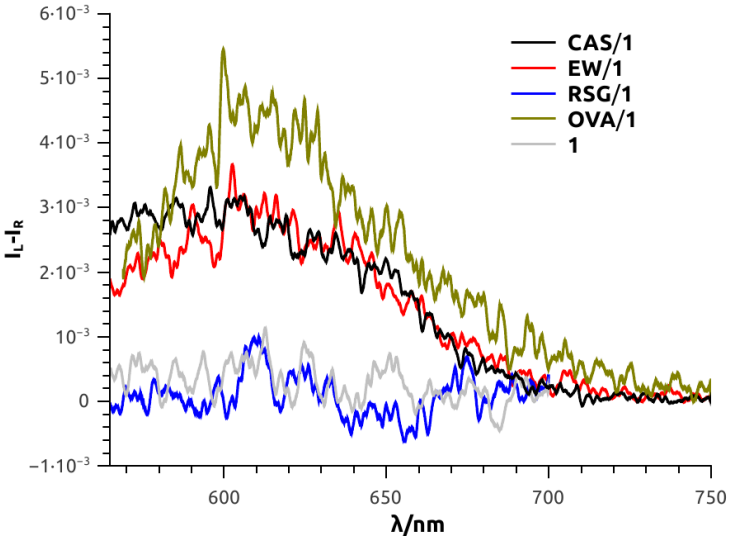

Figure 8-2. CPL spectra of SYPRO Ruby, **1**, without protein and with the three proteins studied (**CAS**, **EW** and **RSG**) and with the model protein **OVA**. The spectra are normalized to the maximum of the fluorescence intensity, so that the g_{PL} values can be directly read on y-axis at the maximum of each curve. λ_{exc} = 470 nm. 1: 6.4 µM, proteins: 245 µM.

On account of the large effect on luminescence, we turned to CPL of **1** with proteins in plateau conditions. In the case of **CAS**, **EW** and **OVA**, we observed a relatively intense positive signal whose maximum around 605 nm roughly matches **1** luminescence spectrum (Figure 8-2). In these cases we found $g_{PL} \approx +3 \cdot 10^{-3}$, which is typical for organic molecules, as well as for most metal complexes (with the notable exception of lanthanides).[1,116] At first sight, this

finding is in striking contrast with the lack of response in ECD, i.e. in absorption. A simple reasoning can solve this puzzle. We know that luminescence of **1** is enhanced upon binding to the protein, while it is only weakly emissive in its free form. If one of the two Δ/Λ coordination enantiomers binds more strongly than the other one, on account of protein stereoselectivity, then it will provide a distinct CPL signal, which cannot be cancelled by its mirror-image. Thus, the mere presence of a CPL band corresponding to the emission of the Ru compound strongly supports the hypothesis of a stereoselective interaction between **1** and the proteins occurs, possibly owing to dye inclusion in a protein pocket or cleft. This holds true for **CAS**, **EW** and also for the model protein **OVA.** *Ceteris paribus*, the most intense signal was recorded with the model protein **OVA**, which is in agreement with fluorescence data. Also in agreement with the fluorescence data is the absence of any CPL signal of the solution of **1** with **RSG**.

In order to confirm the reliability of the signals, we also measured the CPL spectrum of **1** alone in the same conditions and we checked that it gave no signal, as expected. From these observations, we may conclude that **CAS** and **OVA** can host **1** in a cavity, where it is shielded from luminescence quenching effects and which is enantioselective, with a preference for Λ-configuration. **EW** possibly responds similarly to **OVA**, although with some weakened effect, possibly on account of the fact that **OVA** is somewhat diluted in **EW**.

In the case of **2** with all the protein systems, we were not able to measure any significant CPL spectra due to its overall low fluorescence.

Covalent stains (FITC, AMCA and AMCA-X, Scheme 8-1) open on a different landscape, where again CPL plays a fundamental role. In this case the binding to the protein is irreversible and in principle one can securely wash off the excess stain. This applies when developing electrophoretic gels or working with paint cross-sections, because the protein is immobilized, but it is poorly fit for model studies conducted in solution. In contrast with what we required for **1** and **2**, which are necessarily in free/bound exchange, here no change in fluorescence between free and bound dye is necessary. As a result one might not be able to

gain any information from total fluorescence in solution, while chiroptical methods could be of use if the dye, upon binding, experiences a chiral environment.

Indeed, when a fixed concentration of FITC in aqueous solution of carbonate buffer at pH 9 was titrated with increasing amount of proteins (**CAS**, **EW** and **RSG**, respectively), the fluorescence did not change in a noticeable way. Similarly, the proteins had no significant effect on fluorescence intensity of AMCA and AMCA-X during the titrations in carbonate buffer.

We tried to record ECD spectra of FTIC (**3**), but, as in the previous cases, no induced ECD signal was detected corresponding to the absorption band of **3** around 470 nm. On the contrary, taking advantage of the strong fluorescence of FTIC (**3**), we measured the CPL spectra of the three proteins covalently bonded with **3** (Figure 8-3). We were able to measure a weak but significant positive CPL signal ($g_{PL} \approx +6 \cdot 10^{-4}$) in the case of **3/CAS** and **3/EW,** while the spectrum measured for **3**/**RSG** was not significantly different from the baseline recorded on a buffer solution containing **3** without any protein. The mere presence of a CPL signal in the two cases is direct evidence of the occurrence of an interaction between achiral fluorophore **3** and the proteins. It was reported before that fluorescein can give rise to a relatively strong CPL signal (but notably without ECD) when it is in a chiral medium such as in a chiral solvent.[117]

These results are in agreement with the staining tests carried out on cross-sections (Figure 8-1). It is therefore apparent that in such a case CPL provides a clear indication of the interaction, while ECD and fluorescence do not.

Unfortunately, the emission region of AMCA and AMCA-X is currently unsuited to our CPL apparatus.

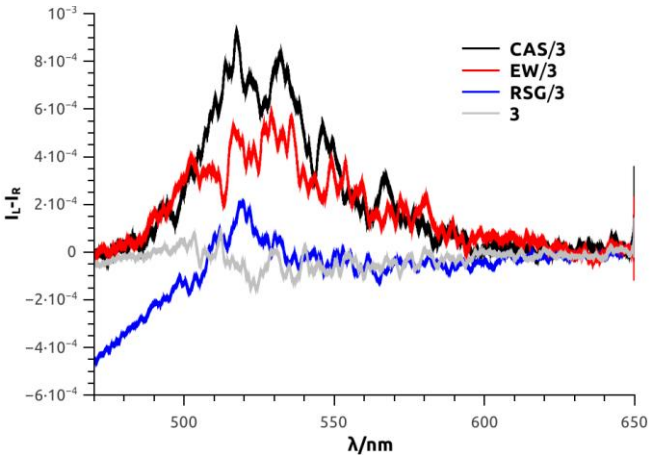

Figure 8-3. CPL spectra of FTIC without protein and with the three proteins studied (**CAS**, **EW**, and **RSG**). The spectra are normalized to the maximum of the fluorescence intensity, so that the g_{PL} values can be directly read on y-axis at the maximum of each curve. λ_{exc} = 365 nm. 3:0.55 µM, proteins: 245 µM.

Conclusions

In this Chapter, we have shown that CPL can be conveniently employed to shed light on the selective interaction between commercial achiral or racemic fluorophores with proteinaceous materials of interest in the field of cultural heritage. CPL can complement fluorescence data or even give information about the occurrence of an interaction when fluorescence or ECD fail, as in the case of the covalent stain FITC. These data will help rationalizing empirical observations from the use of fluorescent stains to localize proteins in samples from works of art, and will provide a rational way to design stains, which reliably, selectively and/or specifically respond to various types of proteinaceous layers in paint cross-sections.

Chapter 9

Home-made spectrofluoropolarimeter

A part of this thesis work was devoted to update an old home-made CP luminescence instrument (spectrofluoropolarimeter).[37,38,118] Our spectrofluoropolarimeter is a converted decommissioned ECD spectropolarimeter (Jasco J500-C, 1981; see Figure 9-1). A simplified scheme of the optical components of our CP luminescence instrument is drawn in Figure 9-2.

Figure 9-1. Our spectrofluoropolarimeter.

In the updated instrument, the sample can be excited with non polarized radiation from a lamp source (such as a xenon or a halogen lamp) passed through a prism monochromator (using a 180° geometry between excitation an detection) or directly from a LED source with a narrow emission spectrum (using a 90° geometry). In this case the excitation light is linearly polarized parallel to the emission detection direction to avoid artifacts due to photoselection.[119] In the case of lanthanide complexes, the sample can be conveniently excited with a fluorescent mercury lamp ($\lambda \approx 365$ nm, again with a 90° geometry).

The light emitted by the sample is passed through a photoelastic modulator (PEM) which converts alternatively (50 KHz) right and left circularly polarized

light into linearly polarized light. A component of the linearly polarized light is then selected by a linear polarizer (oriented at 45° with respect to the PEM easy axis), rendered monochromated by the emission monochromator (diffraction grating, Jasco CT-10, 1200 grooves/mm blazed at 500 nm) and sent to the detector (photomultiplier tube, PMT; Hamamatsu R376).

A lock-in amplifier, working in phase with the PEM, extracts the left and right polarized component of the emission and therefore the CPL signal ($CPL = I_L - I_R$). In the same time, the instrument acquires the total luminescence signal ($I_L + I_R$). The two signals are referred to as alternating current (AC) and direct current (DC) respectively.

We introduced a programmable electronic prototyping platform (Arduino UNO) to control the step motor driving the emission monochromator and to digitalize the analog signals (both AC and DC) from the instrument. These data are transferred to a Microsoft Excel spreadsheet through a data acquisition macro (PLX-DAQ) and the CP luminescence and total emission spectra are plotted in real time in an excel spreadsheet. The fact that the same Arduino board is in charge of both the monochromator motion and signal digitalization ensures that the signal is always in sync with the current wavelength.

Parameters controlled by Arduino, such as starting and ending wavelength and scan-speed, are inputted directly through the same Excel macro. Amplification of CPL signal (sensitivity scale), integration time and the PMT voltage (gain) are selected using the knobs of the original hardware from J500-C. Emission slit-widths are manually adjusted through micrometric heads with vernier scales.

In a standard measurement, the best excitation source is selected for the given sample, usually LED sources of different colours are suitable for SCOMs emitting in the green-red region, while lanthanide complexes are always excited with the UV lamp. Once found the best excitation source available and the maximum emission wavelength, one has to regulate the PM voltage in order to have a measurable DC signal. Increasing the voltage too much results in highly noisy CPL signal. In the mean time, the slit-widths are adjusted according to the

broadness of the emission bands of the sample. When dealing with lanthanides, narrow slit-widths are required (see Chapter 1), while with SCOMs with broad emission bands with no measurable fine structures, it is convenient to open the slit-widths fully (~10 nm) in order to allow as much light as possible to reach the detector. In this way, it is possible to lower the PMT voltage. This precaution is necessary when measuring broad signals with low g factors ($< 10^{-3}$). At this point, a quick measurement suggests the proper CPL scale (sensitivity) and integration time (4 sec are typical for most SCOMs). Scan-speed is set according to Eq. (1-4). The spectrum is accumulated several times, if needed.

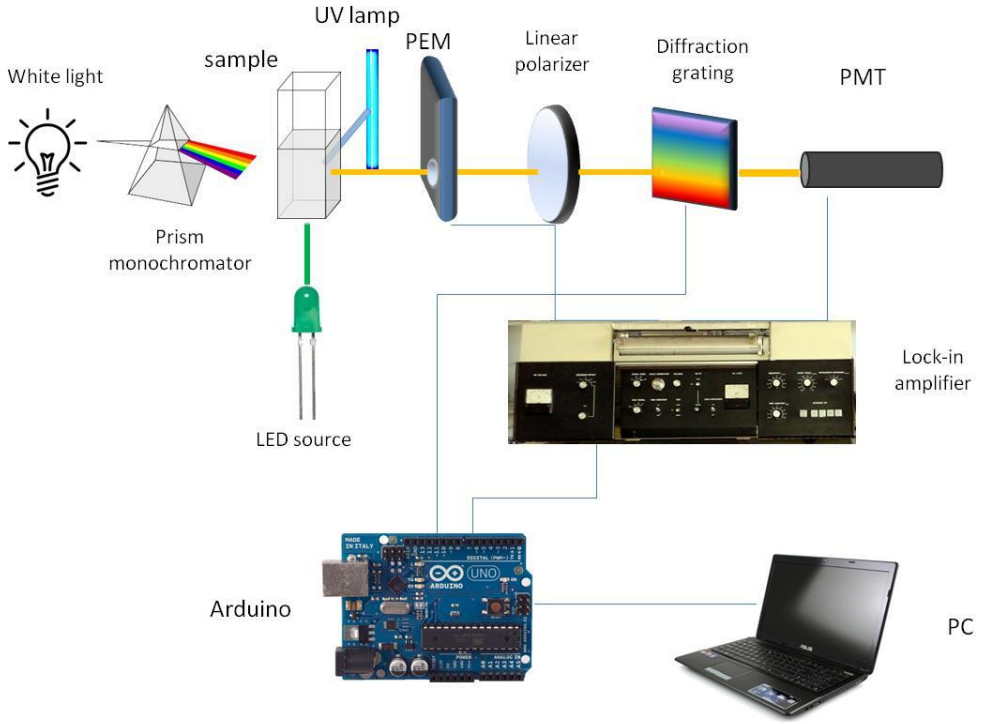

Figure 9-2. Scheme of our spectrofluoropolarimeter.

Both the luminescence (DC) and CPL (AC) signals are given in arbitrary units, with their ratio being directly proportional to g:

$$g = \alpha \cdot \frac{\mathrm{AC}}{\mathrm{DC}} \qquad (9\text{-}1)$$

where α is a constant determined using a standard, such as $CsEu(hfbc)_4$.

As demonstrated by the examples shown in Chapters 6-9, our set-up is able to reliably measure g factors down to 10^{-4}.

Conclusions of Part II

Thanks to our work to update our spectrofluoropolarimeter, we were able to reliably measure CPL of organic molecules with g_{PL} ranging from 10^{-4} to 10^{-3}.

This opened the way to the works that we have detailed in Part II.

A joined computational and spectroscopic work elucidated the intricated photophysics of the excited states of two axially chiral BODIPYs.

An interdisciplinary work involving cultural heritage chemists allowed us to demonstrate that CPL spectroscopy can provide interesting information beside more common techniques (ECD and fluorescence) even in rather complex cases. This demonstrates once again that CPL is a tool able to respond to the needs of modern chemistry.

References

[1] E. M. Sánchez‐Carnerero, A. R. Agarrabeitia, F. Moreno, B. L. Maroto, G. Muller, M. J. Ortiz , S. de la Moya, *Chem. Eur. J.*, **2015**, *21*, 13488.

[2] J. Roose, B. Z. Tang , K. S. Wong, *Small*, **2016**.

[3] Q. Ye, D. Zhu, L. Xu, X. Lu , Q. Lu, *J. Mater. Chem. C*, **2016**, *4*, 1497.

[4] J. Kumar, T. Nakashima , T. Kawai, *J. Phys. Chem. Lett.*, **2015**, *6*, 3445.

[5] S. R. Wilson, M. E. Yurchenko, D. I. Schuster, E. N. Yurchenko, O. Sokolova, S. E. Braslavsky , G. Klihm, *J. Am. Chem. Soc.*, **2002**, *124*, 1977.

[6] M. Oda, H.-G. Nothofer, U. Scherf, V. Šunjic, D. Richter, W. Regenstein , D. Neher, *Macromol.*, **2002**, *35*, 6792.

[7] T. Hamamoto , M. Funahashi, *J. Mater. Chem. C*, **2015**, *3*, 6891.

[8] M. R. Craig, P. Jonkheijm, S. C. Meskers, A. P. Schenning , E. Meijer, *Adv. Mater.*, **2003**, *15*, 1435.

[9] C. Resta, S. Di Pietro, M. Majerić Elenkov, Z. Hameršak, G. Pescitelli , L. Di Bari, *Macromol.*, **2014**, *47*, 4847.

[10] C. Emeis , L. Oosterhoff, *Chem. Phys. Lett.*, **1967**, *1*, 129.

[11] C. A. Emeis , L. J. Oosterhoff, *J. Chem. Phys.*, **1971**, *54*, 4809.

[12] N. Berova, L. Di Bari , G. Pescitelli, *Chem. Soc. Rev.*, **2007**, *36*, 914.

[13] Y. Uchida, T. Hirose, T. Nakashima, T. Kawai , K. Matsuda, *Org. Lett.*, **2016**.

[14] S. Hirata , M. Vacha, *J. Phys. Chem. Lett.*, **2016**, *7*, 1539.

[15] K. Nakabayashi, S. Kitamura, N. Suzuki, S. Guo, M. Fujiki , Y. Imai, *Eur. J. Org. Chem.*, **2016**, *2016*, 64.

[16] M. Okazaki, T. Mizusawa, K. Nakabayashi, M. Yamashita, N. Tajima, T. Harada, M. Fujiki , Y. Imai, *J. Photochem. Photobiol. A*, **2016**.

[17] J. E. Field, G. Muller, J. P. Riehl , D. Venkataraman, *J. Am. Chem. Soc.*, **2003**, *125*, 11808.

[18] G. Longhi, E. Castiglioni, C. Villani, R. Sabia, S. Menichetti, C. Viglianisi, F. Devlin , S. Abbate, *J. Photochem. Photobiol. A*, **2016**.

[19] Y. Yamamoto, H. Sakai, J. Yuasa, Y. Araki, T. Wada, T. Sakanoue, T. Takenobu, T. Kawai , T. Hasobe, *Chem. Eur. J.*, **2016**.

[20] H. Sakai, T. Kubota, J. Yuasa, Y. Araki, T. Sakanoue, T. Takenobu, T. Wada, T. Kawai , T. Hasobe, *Org. Biomol. Chem.*, **2016**.

[21] H. Isla , J. Crassous, *C. R. Chim.*, **2016**, *19*, 39.

[22] I. H. Delgado, S. Pascal, A. Wallabregue, R. Duwald, C. Besnard, L. Guénée, C. Nançoz, E. Vauthey, R. Tovar , J. Lunkley, *Chem. Sci.*, **2016**.

[23] E. M. Sánchez-Carnerero, F. Moreno, B. L. Maroto, A. R. Agarrabeitia, M. J. Ortiz, B. G. Vo, G. Muller , S. d. l. Moya, *J. Am. Chem. Soc.*, **2014**, *136*, 3346.

[24] R. B. Alnoman, S. Rihn, D. C. O'Connor, F. A. Black, B. Costello, P. G. Waddell, W. Clegg, R. D. Peacock, W. Herrebout , J. G. Knight, *Chem. Eur. J.*, **2016**, *22*, 93.

[25] C. Ray, E. Sánchez-Carnerero, F. Moreno, B. Maroto, A. Agarrabeitia, M. Ortiz, Í. López-Arbeloa, J. Bañuelos, K. Cohovi , J. Lunkley, *Chem. Eur. J.*, **2016**.

[26] H. Lu, J. Mack, T. Nyokong, N. Kobayashi , Z. Shen, *Coord. Chem. Rev.*, **2016**, *318*, 1.

[27] Y. Gobo, M. Yamamura, T. Nakamura , T. Nabeshima, *Org. Lett.*, **2016**, *18*, 2719.

[28] M. Gon, Y. Morisaki , Y. Chujo, *Eur. J. Org. Chem.*, **2015**, *2015*, 7756.

[29] J. L. Lunkley, D. Shirotani, K. Yamanari, S. Kaizaki , G. Muller, *Inorg. Chem.*, **2011**, *50*, 12724.

[30] J. Yuasa, T. Ohno, K. Miyata, H. Tsumatori, Y. Hasegawa , T. Kawai, *J. Am. Chem. Soc.*, **2011**, *133*, 9892.
[31] K. Binnemans, *Coord. Chem. Rev.*, **2015**, *295*, 1.
[32] F. Zinna, U. Giovanella , L. Di Bari, *Adv. Mater.*, **2015**, *27*, 1791.
[33] F. Zinna, T. Bruhn, C. A. Guido, J. Ahrens, M. Bröring, L. Di Bari , G. Pescitelli, *Chem. Eur. J.*, **2016**, *22*, 16089.
[34] S. Orsini, F. Zinna, T. Biver, L. Di Bari , I. Bonaduce, *Rsc Advances*, **2016**, *6*, 96176.
[35] S. Pascal, C. Besnard, F. Zinna, L. Di Bari, B. Le Guennic, D. Jacquemin , J. Lacour, *Org. Biomol. Chem.*, **2016**, *14*, 4590.
[36] P. Schippers, A. van den Buekel , H. Dekkers, *J. Phys. E*, **1982**, *15*, 945.
[37] E. Castiglioni, S. Abbate, F. Lebon , G. Longhi, *Methods Appl. Fluoresc.*, **2014**, *2*, 024006.
[38] E. Castiglioni, S. Abbate , G. Longhi, *Appl. Spectrosc.*, **2010**, *64*, 1416.
[39] A. Loudet , K. Burgess, *Chem. Rev.*, **2007**, *107*, 4891.
[40] G. Ulrich, R. Ziessel , A. Harriman, *Angew. Chem. Int. Ed.*, **2008**, *47*, 1184.
[41] J.-J. Lee, S.-C. Lee, D. Zhai, Y.-H. Ahn, H. Y. Yeo, Y. L. Tan , Y.-T. Chang, *Chem. Commun.*, **2011**, *47*, 4508.
[42] J. F. Kögel, S. Kusaka, R. Sakamoto, T. Iwashima, M. Tsuchiya, R. Toyoda, R. Matsuoka, T. Tsukamoto, J. Yuasa , Y. Kitagawa, *Angew. Chem. Int. Ed.*, **2016**, *55*, 1377.
[43] A. B. Nepomnyashchii, M. Bröring, J. Ahrens , A. J. Bard, *J. Am. Chem. Soc.*, **2011**, *133*, 19498.
[44] T. Bruhn, G. Pescitelli, S. Jurinovich, A. Schaumlöffel, F. Witterauf, J. Ahrens, M. Bröring , G. Bringmann, *Angew. Chem. Int. Ed.*, **2014**, *53*, 14592.
[45] S. Jurinovich, C. A. Guido, T. Bruhn, G. Pescitelli , B. Mennucci, *Chem. Commun.*, **2015**, *51*, 10498.
[46] K. Tanaka, G. Pescitelli, K. Nakanishi , N. Berova, *Monatsh. Chem.*, **2005**, *136*, 367.
[47] T. Kawai, K. Kawamura, H. Tsumatori, M. Ishikawa, M. Naito, M. Fujiki , T. Nakashima, *ChemPhysChem*, **2007**, *8*, 1465.
[48] T. Nishikawa, N. Tajima, M. Kitamatsu, M. Fujiki , Y. Imai, *Org. Biomol. Chem.*, **2015**, *13*, 11426.
[49] F. C. Spano, S. C. Meskers, E. Hennebicq , D. Beljonne, *J. Chem. Phys.*, **2008**, *129*, 024704.
[50] R. Tempelaar, A. Stradomska, J. Knoester , F. C. Spano, *J. Phys. Chem. B*, **2011**, *115*, 10592.
[51] M. Bröring, R. Krüger, S. Link, C. Kleeberg, S. Köhler, X. Xie, B. Ventura , L. Flamigni, *Chem. Eur. J.*, **2008**, *14*, 2976.
[52] B. Ventura, G. Marconi, M. Bröring, R. Krüger , L. Flamigni, *New J. Chem.*, **2009**, *33*, 428.
[53] J. Kumar, T. Nakashima, H. Tsumatori , T. Kawai, *J. Phys. Chem. Lett.*, **2014**, *5*, 316.
[54] P. Schippers, J. Van der Ploeg , H. Dekkers, *J. Am. Chem. Soc.*, **1983**, *105*, 84.
[55] S. Chibani, A. D. Laurent, B. Le Guennic , D. Jacquemin, *J. Chem. Theory Comput.*, **2014**, *10*, 4574.
[56] S. Chibani, B. Le Guennic, A. Charaf-Eddin, A. D. Laurent , D. Jacquemin, *Chem. Sci.*, **2013**, *4*, 1950.
[57] S. Chibani, B. Le Guennic, A. Charaf-Eddin, O. Maury, C. Andraud , D. Jacquemin, *J. Chem. Theory Comput.*, **2012**, *8*, 3303.

[58] M. Bröring, Y. Yuan, R. Krüger, C. Kleeberg , X. Xie, *Z. Anorg. Allg. Chem.*, **2010**, *636*, 518.
[59] J. Ahrens, PhD Thesis, Technische Universität Braunschweig, 2013.
[60] G. Mazzeo, S. Abbate, G. Longhi, E. Castiglioni, S. E. Boiadjiev , D. A. Lightner, *J. Phys. Chem. B*, **2016**, *120*, 2380.
[61] M. Pecul , K. Ruud, *Phys. Chem. Chem. Phys.*, **2011**, *13*, 643.
[62] S. Abbate, G. Longhi, F. Lebon, E. Castiglioni, S. Superchi, L. Pisani, F. Fontana, F. Torricelli, T. Caronna , C. Villani, *J. Phys. Chem. C*, **2014**, *118*, 1682.
[63] G. Longhi, E. Castiglioni, S. Abbate, F. Lebon , D. A. Lightner, *Chirality*, **2013**, *25*, 589.
[64] G. Longhi, E. Castiglioni, C. Villani, R. Sabia, S. Menichetti, C. Viglianisi, F. Devlin , S. Abbate, *J. Photochem. Photobiol. A*.
[65] G. Longhi, S. Abbate, G. Mazzeo, E. Castiglioni, P. Mussini, T. Benincori, R. Martinazzo , F. Sannicolò, *J. Phys. Chem. C*, **2014**, *118*, 16019.
[66] R. Fukuda , M. Ehara, *Phys. Chem. Chem. Phys.*, **2013**, *15*, 17426.
[67] G. Pescitelli , T. Bruhn, *Chirality* **2016**, *28*, 466.
[68] A. V. Marenich, C. J. Cramer, D. G. Truhlar, C. A. Guido, B. Mennucci, G. Scalmani , M. J. Frisch, *Chem. Sci.*, **2011**, *2*, 2143.
[69] V. P. Nicu , E. J. Baerends, *Phys. Chem. Chem. Phys.*, **2011**, *13*, 16126.
[70] G. Longhi, M. Tommasini, S. Abbate , P. L. Polavarapu, *Chem. Phys. Lett.*, **2015**, *639*, 320.
[71] T. Kimoto, N. Tajima, M. Fujiki , Y. Imai, *Chem. Asian J.*, **2012**, *7*, 2836.
[72] T. Kinuta, N. Tajima, M. Fujiki, M. Miyazawa , Y. Imai, *Tetrahedron*, **2012**, *68*, 4791.
[73] Y. Kitayama, K. Nakabayashi, T. Wakabayashi, N. Tajima, M. Fujiki , Y. Imai, *Rsc Advances*, **2015**, *5*, 410.
[74] V. Barone, A. Baiardi , J. Bloino, *Chirality*, **2014**, *26*, 588.
[75] B. Pritchard , J. Autschbach, *ChemPhysChem*, **2010**, *11*, 2409.
[76] Y. Liu, J. Cerezo, G. Mazzeo, N. Lin, X. Zhao, G. Longhi, S. Abbate , F. Santoro, *J. Chem. Theory Comput.*, **2016**, *12*, 2799.
[77] M. Gingras, *Chem. Soc. Rev.*, **2013**, *42*, 1051.
[78] N. Saleh, C. Shen , J. Crassous, *Chem. Sci.*, **2014**, *5*, 3680.
[79] N. Saleh, B. Moore, M. Srebro, N. Vanthuyne, L. Toupet, J. A. G. Williams, C. Roussel, K. K. Deol, G. Muller, J. Autschbach , J. Crassous, *Chem. Eur. J.*, **2015**, *21*, 1673.
[80] M. Shigeno, Y. Kushida , M. Yamaguchi, *J. Am. Chem. Soc.*, **2014**, *136*, 7972.
[81] H. Maeda, Y. Bando, K. Shimomura, I. Yamada, M. Naito, K. Nobusawa, H. Tsumatori , T. Kawai, *J. Am. Chem. Soc.*, **2011**, *133*, 9266.
[82] S. Akine, S. Hotate , T. Nabeshima, *J. Am. Chem. Soc.*, **2011**, *133*, 13868.
[83] J. Nishida, T. Suzuki, M. Ohkita , T. Tsuji, *Angew. Chem.*, **2001**, *113*, 3351.
[84] J. K. Zak, M. Miyasaka, S. Rajca, M. Lapkowski , A. Rajca, *J. Am. Chem. Soc.*, **2010**, *132*, 3246.
[85] T. Biet, A. Fihey, T. Cauchy, N. Vanthuyne, C. Roussel, J. Crassous , N. Avarvari, *Chem. Eur. J.*, **2013**, *19*, 13160.
[86] L. Pospíšil, L. Bednárová, P. Štěpánek, P. Slavíček, J. Vávra, M. n. Hromadová, H. Dlouhá, J. n. Tarábek , F. Teplý, *J. Am. Chem. Soc.*, **2014**, *136*, 10826.
[87] M. P. Colombini , F. Modugno, *Organic mass spectrometry in art and archaeology*, Wiley Online Library, 2009.
[88] M. P. Colombini, A. Andreotti, I. Bonaduce, F. Modugno , E. Ribechini, *Acc. Chem. Res.*, **2010**, *43*, 715.

[89] S. Dallongeville, N. Garnier, C. Rolando , C. Tokarski, *Chem. Rev.*, **2015**, *116*, 2.
[90] L. Burgio, R. J. Clark , R. R. Hark, *Proc. Natl. Acad. Sci.*, **2010**, *107*, 5726.
[91] R. J. Clark, *Chem. Soc. Rev.*, **1995**, *24*, 187.
[92] A. Hawe, M. Sutter , W. Jiskoot, *Pharm. Res.*, **2008**, *25*, 1487.
[93] I. C. A. Sandu, A. C. A. Roque, P. Matteini, S. Schäfer, G. Agati, C. R. Correia , J. F. F. P. Viana, *Microsc. Res. Tech.*, **2012**, *75*, 316.
[94] L. S. Dolci, G. Sciutto, M. Guardigli, M. Rizzoli, S. Prati, R. Mazzeo , A. Roda, *Anal. Bioanal. Chem.*, **2008**, *392*, 29.
[95] G. Sciutto, L. S. Dolci, A. Buragina, S. Prati, M. Guardigli, R. Mazzeo , A. Roda, *Anal. Bioanal. Chem.*, **2011**, *399*, 2889.
[96] G. Sciutto, L. Dolci, M. Guardigli, M. Zangheri, S. Prati, R. Mazzeo , A. Roda, *Anal. Bioanal. Chem.*, **2013**, *405*, 933.
[97] G. Sciutto, S. Prati, R. Mazzeo, M. Zangheri, A. Roda, L. Bardini, G. Valenti, S. Rapino , M. Marcaccio, *Anal. Chim. Acta*, **2014**, *831*, 31.
[98] I. Sela-Culang, V. Kunik , Y. Ofran, *Immune system modeling and analysis*, **2015**, 8.
[99] C. Duce, E. Bramanti, L. Ghezzi, L. Bernazzani, I. Bonaduce, M. P. Colombini, A. Spepi, S. Biagi , M. R. Tine, *Dalton Trans.*, **2013**, *42*, 5975.
[100] C. Duce, L. Ghezzi, M. Onor, I. Bonaduce, M. P. Colombini, M. R. Tine , E. Bramanti, *Anal. Bioanal. Chem.*, **2012**, *402*, 2183.
[101] L. Ghezzi, C. Duce, L. Bernazzani, E. Bramanti, M. P. Colombini, M. R. Tiné , I. Bonaduce, *J. Therm. Anal. Calorim.*, **2015**, *122*, 315.
[102] D. Pellegrini, C. Duce, I. Bonaduce, S. Biagi, L. Ghezzi, M. P. Colombini, M. R. Tinè , E. Bramanti, *Microchem. J.*, **2016**, *124*, 31.
[103] G. Leo, I. Bonaduce, A. Andreotti, G. Marino, P. Pucci, M. P. Colombini , L. Birolo, *Anal. Chem.*, **2011**, *83*, 2056.
[104] A. Nevin, D. Anglos, S. Cather , A. Burnstock, *Appl. Phys. A*, **2008**, *92*, 69.
[105] J. E. Berlier, A. Rothe, G. Buller, J. Bradford, D. R. Gray, B. J. Filanoski, W. G. Telford, S. Yue, J. Liu , C.-Y. Cheung, *J. Histochem. Cytochem.*, **2003**, *51*, 1699.
[106] D. Kretschy, G. Koellensperger , S. Hann, *Anal. Chim. Acta*, **2012**, *750*, 98.
[107] K. Muramoto, H. Kamiya , H. Kawauchi, *Anal. Biochem.*, **1984**, *141*, 446.
[108] S. Kuckova, I. C. A. Sandu, M. Crhova, R. Hynek, I. Fogas , S. Schafer, *J. Cult. Herit.*, **2013**, *14*, 31.
[109] D. Magrini, S. Bracci , I. C. A. Sandu, *Procedia Chem.*, **2013**, *8*, 194.
[110] M. S. Ball , P. Karuso, *J. Proteome Res.*, **2007**, *6*, 4313.
[111] G. Pescitelli, L. Di Bari , N. Berova, *Chem. Soc. Rev.*, **2014**.
[112] P. R. Banks , D. M. Paquette, *Bioconjugate Chem.*, **1995**, *6*, 447.
[113] S. Dallongeville, M. Richter, S. Schäfer, M. Kühlenthal, N. Garnier, C. Rolando , C. Tokarski, *Analyst*, **2013**, *138*, 5357.
[114] G. Crosby, W. Perkins , D. Klassen, *J. Chem. Phys.*, **1965**, *43*, 1498.
[115] G. D. Fasman, *Circular dichroism and the conformational analysis of biomolecules*, Springer Science & Business Media, 2013.
[116] F. Zinna , L. Di Bari, *Chirality*, **2015**, *27*, 1.
[117] H. Brittain , F. Richardson, *J. Phys. Chem.*, **1976**, *80*, 2590.
[118] E. Castiglioni, P. Albertini , S. Abbate, *Chirality*, **2010**, *22*, E142.
[119] H. P. Dekkers, P. F. Moraal, J. M. Timper , J. P. Riehl, *Appl. Spectrosc.*, **1985**, *39*, 818.

Appendices

Appendix A

Appendix to Chapter 2

NMR were performed with a Varian spectrometer operating at 600, 150 and 79 MHz for ^{1}H, ^{13}C and ^{133}Cs respectively, inversion recovery and 2D experiments were performed using standard pulse sequences, a reverse triple resonance ^{1}H, ^{13}C tunable or a direct broadband with z-gradients probe head were used. Temperature was set to 25.0 ± 0.1 °C and in all cases the sample was let equilibrate for at least 10 min before acquisition.

The MALDI-TOF mass spectra were collected with a Voyager DE (PerSeptive Biosystem) equipped with a nitrogen laser (emission at 337 nm for 3 ns) and a flash AD converter (time base 2 ns). In order to avoid fragmentation of the sample, the laser irradiance was maintained slightly above threshold. Each spectrum was an average of 32 laser shots. The MALDI-TOF investigations were performed by loading on the plate 0.4 mmol of matrix, trans-2-[3-(4-tert-butylphenyl)-2-methyl-2propenylidene]-malonitrile (DCTB), and 0.005 mmol of sample, using CH_2Cl_2 as the solvent. For positive MALDI-TOF mass spectra, both 5,10-di(p-dodecanoxyphenyl)-15,20-di(p-hydroxyphenyl) porphyrin ($C_{68}H_{78}N_4O_4$, 1014 Da), tetrakis(p-dodecanoxyphenyl)porphyrin ($C_{92}H_{126}N_4O_4$, 1350 Da) and a PEG sample of known structure were used as external standards for m/z calibration. Instead, for negative MALDI-TOF spectra, fullerene-[60] ($C_{60,}$ 720 Da) and 61,61-bis(p-methoxyphenyl)methano-1,2-fullerene[60] ($C_{75}H_{14}O_2$, 946 Da) were used as external standards for m/z calibration. The MALDI-TOF mass spectra were elaborated with Grams software (ver. 3.04), from Perseptive Biosystems.

UV-Vis spectra were recorded with a JASCO V-650 spectrophotometer, ECD spectra were recorded with a JASCO J-710 spectropolarimeter.

CPL spectra were measured using 370 nm excitation; solutions samples were measured with a 90° geometry (scan-speed 0.5 nm/sec, 4 accumulations, acquisition time ~13 min), while for film samples a 180° geometry were used (scan-speed 0.5 nm/sec, 1 accumulation, acquisition time ~3 min). The presence of artifacts due to linear polarization components were excluded by demodulating the signal at twice the frequency of photoelastic modulator, with an additional 100KHz lock-in amplifier.

The ligand geometry used as the PERSEUS calculation input was determined optimizing a Na^+ anion of trifluoromethylcarvonate at DFT level with B3LYP functional and 6-31G* basis set using Gaussian.[A1]

All the syntheses were carried under N_2 atmosphere in oven dried glassware using standard Schlenk techniques.

Synthesis of heptafluorobutyrylcarvone

To a solution of 7.5 mL (53 mmol) of $^{i}Pr_2NH$ in 60 mL of distilled diethyl ether 21.6 mL (53 mmol) of ^{n}BuLi 2.5 M in 100 mL of ether were slowly dropped; after a hour, the system was cooled to -90 °C, 8.0 mL (53 mmol) of (±)-carvone and, after additional two hours, 9.7 mL (56 mmol) of ethyl heptafluorobutyrate were added. The resulting mixture was allowed to warm to room temperature under stirring overnight and then it was hydrolyzed with 60 mL of HCl ~3M and extracted with ether (2x100 mL). The recombined organic phases were washed with water until neutrality (5x100 mL), dried on Na_2SO_4 and the solvent was evaporated under reduced pressure. The crude product was purified by flash chromatography (SiO_2; CH_2Cl_2/petroleum ether:8/2) to afford the product as a reddish-brown liquid (5.5 g, 30 %).

^{1}H-NMR ($CDCl_3$, 25 °C, eno form), δ (ppm): 1.74 (s, 3H); 1.90 (s, 3H); 2.57 (m, 2H); 3.56 (m, 1H); 4.52 (m, 1H); 4.84 (m, 1H); 6.50 (m, 1H); 16.48 (s, 1H).

^{13}C-NMR ($CDCl_3$, 25 °C, eno form), δ (ppm): 15.8 (C-Me); 22.1 (C-Me); 28.5 (C4); 37.9 (C5); 113.1 (C8); 142.8 (C3); 190.3; 195.0.

Negative MALDI-TOF (m/z): calc for $C_{14}H_{13}F_7O_2$ ($[M]^-$), 346.1, found 346.2 (Figure A2-6).

λ_{max}/nm, CH_3CN (ε/$M^{-1}cm^{-1}$): 240 (5640); 313 (2680); 358 (2160).

Preparation of Cs[Ln(hfbcv)$_4$]

To 260 mg (0.75 mmol) of heptafluorobutyrylcarvone in 5 mL of distilled CH_3CN, 254 mg (0.75 mmol) of Cs_2CO_3 were added at 50 °C; after an hour 0 19 mmol of anhydrous $LnCl_3$ were added, and the mixture was stirred for 4 hours at 50 °C. The solvent was removed under reduced pressure and the crude product product was taken up with 2 mL of distilled diethyl ether and filtered through a sintered glass filter (porosity G3). After removing the solvent, 800 mL of petroleum ether were added, and the mixture was allowed to cool down to -10 °C; the supernatant solution was recovered and the solvent was evaporated under reduced pressure.

^{1}H-NMR (CD_3CN, 25 °C, broad singlets)

δ (ppm) (Ln = La): 1.66 (6H); 2.94; 3.27; 3.44; 4.51; 4.64; 6.17.

δ (ppm) (Ln = Ce): 0.28 (3H); 2.77 (3H); 3.52; 5.73; 6.15; 7.54; 8.14.

δ (ppm) (Ln = Pr): -2.67 (3H); 3.39 (3H); 4.35; 4.85; 6.93; 7.47; 8.41; 10.03.

δ (ppm) (Ln = Nd): 0.69 (3H); 2.62 (3H); 3.09; 3.34; 5.51; 5.93; 7.6; 8.19.

δ (ppm) (Ln = Eu): 0.78 (3H); 1.45; 1.55; 1.64; 2.08; 2.82 (3H); 3.11; 3.44.

δ (ppm) (Ln = Tb): -27.21 (3H); 14.81; 21.74 (3H); 25.71; 33.19; 36.03; 41.45; 75.26.

^{13}C-NMR

δ (ppm) (Ln = La): 16.2; 21.1; 40.1; 112.2; 135.9.

δ (ppm) (Ln = Ce): 15.0; 23.4; 31.0; 42.3; 115.0; 133.8.

δ (ppm) (Ln = Pr): 23.9; 33.3; 42.8; 116.0; 134.6.

δ (ppm) (Ln = Nd): 15.2; 22.6; 31.8; 39.2; 114.8; 135.4.

δ (ppm) (Ln = Eu): 18.4; 21.3; 25.3; 43.8; 110.9; 132.8.

Positive MALDI-TOF (Figure A2-7) of Cs[Eu(hfbcv)$_4$] (m/z): calc for $C_{56}H_{48}CsEuF_{28}O_8$ ([M]H$^+$) 1666.1, found 1666.5.

Negative MALDI-TOF (Figure A2-8) of Cs[Eu(hfbcv)$_4$] (m/z): calc for $C_{14}H_{12}F_7O_2$ (hfbcv$^-$), 345.1, found 345.5; calc for $C_{42}H_{36}EuF_{21}O_6$ (Eu(hfbcv)$_3$) 1188.1, found 1187.3; calc for C56H48EuF28O8 ([Eu(hfbcv)$_4$]$^-$) 1533.2, found 1532.6.

Preparation of Cs[Ln(hfbcv)$_4$]/Ln(hfbcv)$_3$ mixture

$LnCl_3$ (0.13 mmol) and CsCl (0.5 mmol) were dissolved in water (10 mL), simultaneously a Et_3N (0.50 mmol) and hfbcvH (0.50 mmol) solution in $CHCl_3$ (10 mL) was prepared. The two solution were mixed together in a separatory funnel and shaken. The organic phase was recovered, washed with water dried over anhydrous Na_2SO_4. The solvent was evaporated under reduced pressure.

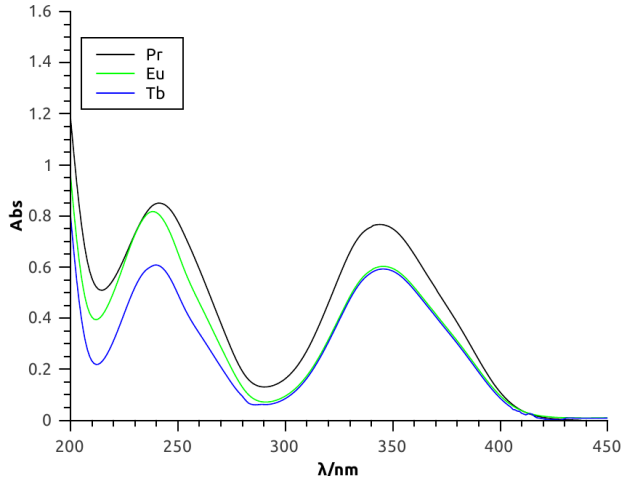

Figure A2-1: Absorption spectra of Cs[Ln(*(R)*-hfbcv)$_4$] (Ln = Pr, Eu, Tb) $6.0 \cdot 10^{-3}$ M in CH_3CN solution (optical path 0.01 cm).

NMR structural characterization

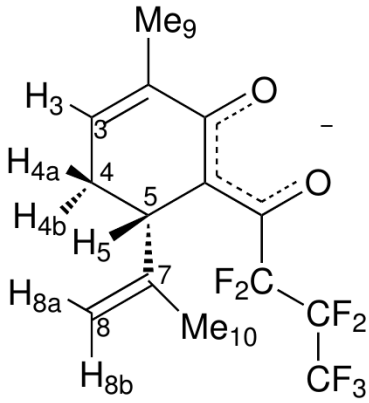

Resonances and isostructurality

Paramagnetic shifts (δ^{para}) were extracted by subtracting the shifts obtained from the diamagnetic Cs[La(hfbcv)$_4$] complex from the observed shifts (δ^{obs}).

$$\delta^{para} = \delta^{obs} - \delta^{dia} \qquad \text{(A2-1)}$$

Table A2-1: ^{1}H δ^{para} for the Cs[Ln(*(R)*-hfbcv)$_4$] complexes and diamagnetic references (δ^{dia}) from Cs[La(hfbcv)$_4$].

	Pr	**Ce**	**Nd**	**Eu**	**Tb**	**La**
^{1}H	δ^{para}	δ^{para}	δ^{para}	δ^{para}	δ^{para}	δ^{dia}
Me$_9$	-4.33	-1.38	-0.97	1.16	-29.11	1.66
Me$_{10}$	1.73	1.11	0.96	-0.88	20.00	1.66
3	2.24	1.37	2.20	-3.06	29.54	6.17
4a	1.08	0.25	0.07	-1.63	11.52	3.27
4b	1.91	/	0.15	-0.86	23.15	2.94
5	4.03	2.29	2.07	-1.99	37.90	3.44
8a	5.39	3.50	2.96	-3.09	70.78	4.64
8b	2.42	1.64	1.42	-1.07	28.36	4.51

Table A2-2: ^{13}C δ^{para} for the Cs[Ln(*(R)*-hfbcv)$_4$] complexes and diamagnetic references (δ^{dia} from Cs[La(hfbcv)$_4$]).

	Pr	**Ce**	**Nd**	**Eu**	**La**
^{13}C	δ^{para}	δ^{para}	δ^{para}	δ^{para}	δ^{dia}
C-Me$_9$	-2.1	-6.1	-5.9	-2.7	21.1
C-Me$_{10}$	7.7	7.2	6.4	5.1	16.2
C3	-1.3	-2.1	-0.5	-3.1	135.9
C5	2.7	2.2	-0.9	3.7	40.1
C8	3.8	2.8	2.6	-1.3	112.2

Isostructurality along the investigated part of the series can be assessed plotting the ^1H paramagnetic shifts for each resonances of a given lanthanide (δ^{para}(Ln)) against the paramagnetic shifts observed for a reference complex, in our case Cs[Pr(hfbcv)$_4$] δ^{para}(Pr).[A2]

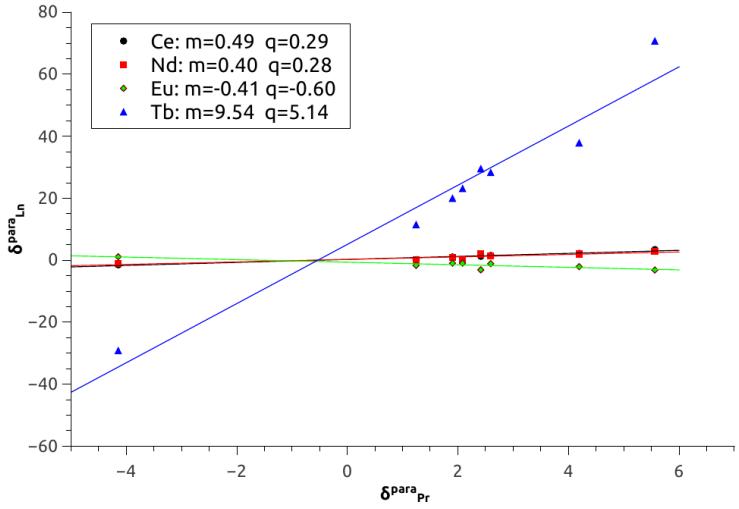

Figure A2-2. δ^{para}(Ln) against δ^{para}(Pr) for the Cs[Ln(*(R)*-hfbcv)$_4$] complexes with slopes (*m*) and intercepts (*q*), showing isostructurality. Notice that the lines were not forced through the origin.

The linearity ($R^2 > 0.99$) between the obtained m_{Ln} slopes (Figure A2-2) and the Bleaney C_j constants demonstrates no major crystal field parameter variation from Ce to Eu.

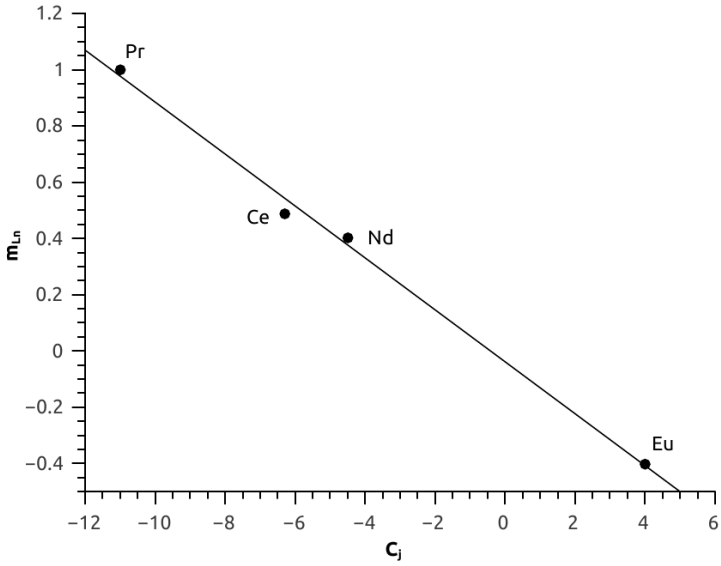

Figure A2-3. m_{Ln} (see Figure A2-2) against Bleaney C_j constants.

Fermi contact/pseudocontact separation

Pseudocontact shifts (δ^{PC}) are relevant for structure determination (see below), they are determined by subtracting the Fermi contact shifts (δ^{FC}) from the paramagnetic shift (δ^{para}):

$$\delta^{PC} = \delta^{para} - \delta^{FC} \qquad \text{(A2-2)}$$

To determine δ^{FC} we used the slopes of the linear interpolations m_{Ln} (Figure A2-2) through the modified Reilley procedure,[A3] with Pr complex as the reference, since it provides a large $C_j/\langle S_Z \rangle_{Ln}$ ratio.[A3] In our case, the contribution of the Fermi contact shift resulted negligible or very small for both ^1H and ^{13}C resonance sets (Table A2-3**Errore. L'origine riferimento non è stata trovata.**).

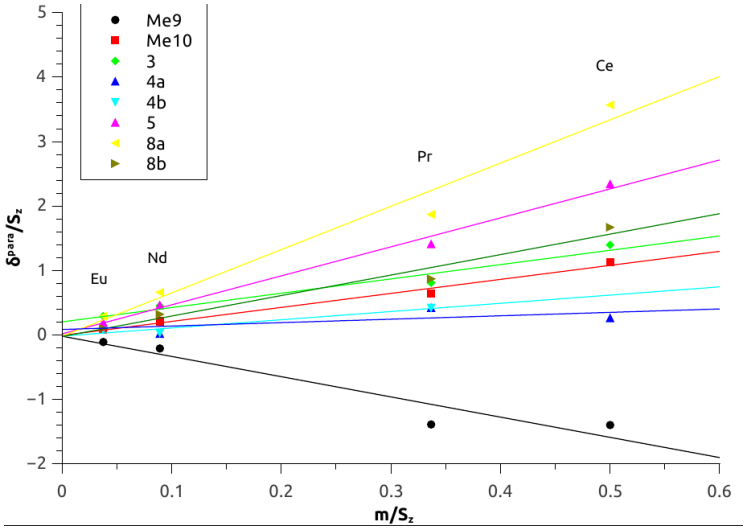

Figure A2-4. Modified Reilley plot[A3] for the Cs[Ln((*R*)-hfbcv)$_4$] complexes (Ln = Ce, Pr, Nd, Eu) for ^{1}H Pseudocontact/Fermi contact shift separation.

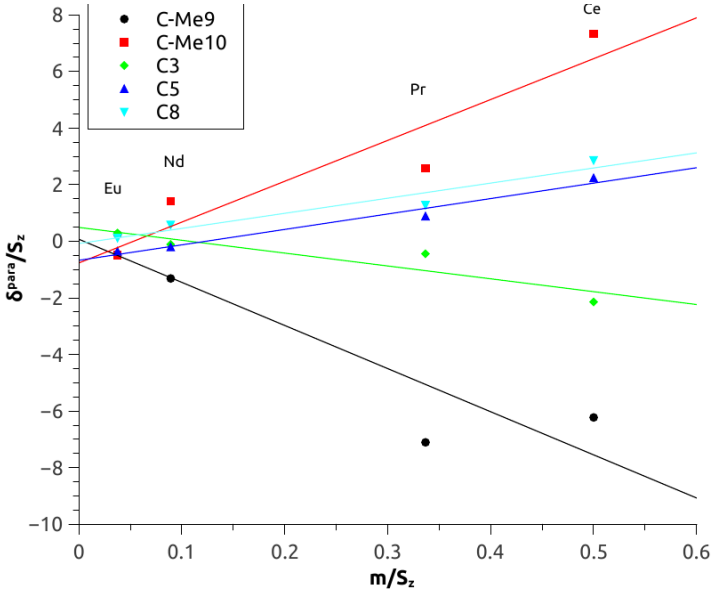

Figure A2-5. Modified Reilley plot[A3] for the Cs[Ln((*R*)-hfbcv)$_4$] complexes (Ln = Ce, Pr, Nd, Eu) for ^{13}C Pseudocontact/Fermi contact shift separation.

Structure determination

Pseudocontact shifts contain geometric information. The pseudocontact shift of each observed nucleus *i* is:

$$\delta_i^{PC} = D\ \frac{3\cos^2\vartheta_i - 1}{r_i^3} \qquad \text{(A2-3)}$$

where ϑ is the angle between the nucleus-Ln vector and the C_4 axis, r_i is the distance between the lanthanide and nucleus *i* and *D* is a parameter related to the anisotropy susceptibility tensor of the complex.

Table A2-3. PERSEUS output: Cs[Pr(*(R)*-hfbcv)$_4$] ^{1}H and ^{13}C-NMR calculated (δ^{PC}_{calc}) and experimental (δ^{PC}_{exp}) pseudocontact shifts, and Fermi contact shifts (δ^{FC}) obtained through modified Reilley procedure. [A4]

Nucleus	δ^{PC}_{calc}	δ^{PC}_{exp}	δ^{FC}
Me_9	-4.02	-4.31	-0.02
Me_{10}	1.71	1.74	-0.01
3	0.53	2.04	0.20
4a	1.80	1.08	0.01
4b	2.62	1.91	-0.02
5	3.64	4.02	0.02
8a	5.39	5.41	-0.02
8b	2.62	2.44	-0.02
C-Me_{10}	2.86	8.46	-0.76
C3	1.38	-1.79	-0.49
C5	6.02	3.17	-0.67
C8	4.31	3.81	-0.01

PERSEUS routine takes a guess structure as the input, calculates δ^{PC}_{exp} for each nucleus (using the equation above) and compare the obtained value with the experimental one (δ^{PC}_{exp}). Then, by minimizing the functional

$$\sum_i \frac{(\delta^{PC}_{i,calc} - \delta^{PC}_{i,exp})^2}{\delta^{PC}_{i,exp}{}^2} \qquad \text{(A2-4)}$$

it can determine the best-fitting geometrical parameters.

In a similar way it can use also paramagnetic relaxation rates (ρ^{para}_i) as additional constraints. In fact

$$\rho_i^{para} = \frac{Const}{r_i^3} \qquad \text{(A2-4)}$$

Table A2-4. PERSEUS output: Cs[Pr(*(R)*-hfbcv)$_4$] calculated (ρ^{para}_{calc}) and experimental (ρ^{para}_{exp}) relaxation rates, and their residuals ($\Delta\rho = \rho^{para}_{calc} - \rho^{para}_{exp}$).

Nucleus	ρ^{para}_{calc}	ρ^{para}_{exp}	$\Delta\rho$
Me$_9$	9.87	9.21	0.66
Me$_{10}$	1.04	1.67	-0.63
3	0.57	4.73	-4.16
4a	0.45	3.42	-2.97
4b	0.77	3.96	-3.19
5	1.66	3.48	-1.82
8a	13.46	13.16	0.30
8b	1.59	0.84	0.75

Exchange kinetics

EXSY spectrum of Cs[Nd(hfbcv)$_4$] with a mixing time of 450 msec, displaying exchange cross peaks between all paramagnetically shifted signals and those of

the free ligand can be employed to calculate the exchange rate between bound and free ligands.

Selecting three pairs of exchange patterns (proton **3** which in bound/free form falls at 8.19/6.12 ppm, proton **5** falling at 5.51/3.67 ppm and proton **8b** falling at 5.93/4.60 ppm, all of which are well-separated from any interfering signals), we quantified diagonal and cross peak volumes, which were analyzed through the EXSYCalc routine; [A5] the direct and reverse rate constants resulted to be $6 \cdot 10^{-2}$ and $1 \cdot 10^{-2}$ sec^{-1}.

Tris/*tetrakis* recognition experiment

The biphasic protocol was the only one affording a tris/tetrakis mixture. The signals of the two species can be assigned through standard bidimensional homo and hetero-correlation experiments. The DMSO experiment (see main text), is a quick way to distinguish them unambiguously.

Table A2-5. μL of added DMSO to the mixture of *tris* + *tetrakis* (Pr(*(R)*-hfbcv)$_3$ + [Pr(*(R)*-hfbcv)$_4$]$^-$), molar ratio of DMSO/(*tris* + *tetrakis*) and molar ratio of *tris*/*tetrakis*.

DMSO/*μ*L	**DMSO/(*tris*+*tetrakis*)**	***tris*/*tetrakis***
0	0	3.0
1	3.4	3.9
2	6.7	5.5
5	16.9	9.8
10	33.7	13.8

The analysis of the paramagnetic shifts of the *tris* species during the titration with DMSO reveals that the structure of $Pr(hfbcv)_3$ is not deeply affected by axial coordination to water or to DMSO and that the change of the resonance shifts is mainly due to a variation of the anisotropy of the magnetic susceptibility tensor of the Pr complex, as shown by the good linearity (R^2>0.99) obtained plotting δ^{para} at various DMSO concentrations against δ^{para} of the complex before adding DMSO.

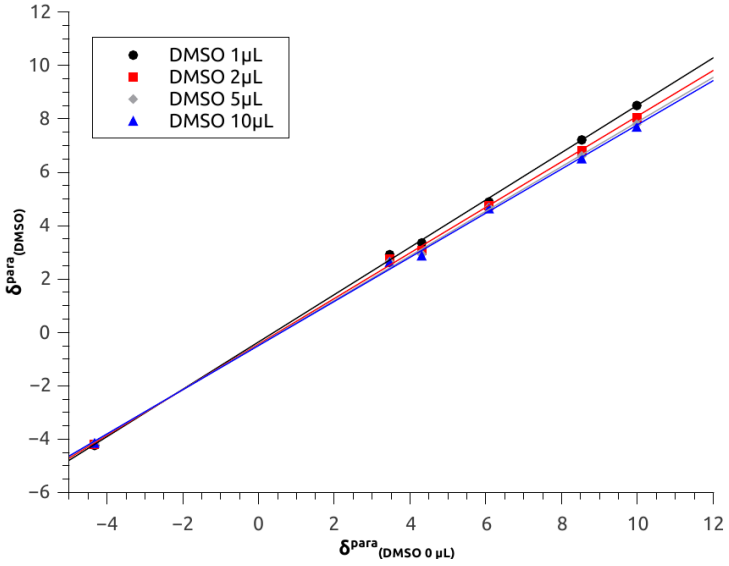

Figure A2-5. ^{1}H-NMR paramagnetic shifts of $Pr((R)\text{-}hfbcv)_3$ (δ^{para}(Pr,i)) at increasing quantities of DMSO against (δ^{para}(Pr,i)) at DMSO = 0.

MALDI-TOF MS characterization

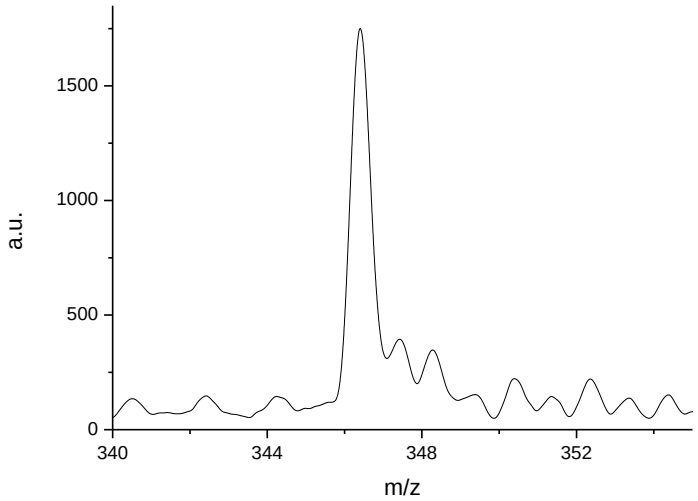

Figure A2-6. MALDI-TOF mass spectrum of *(R)*-hfbcvH.

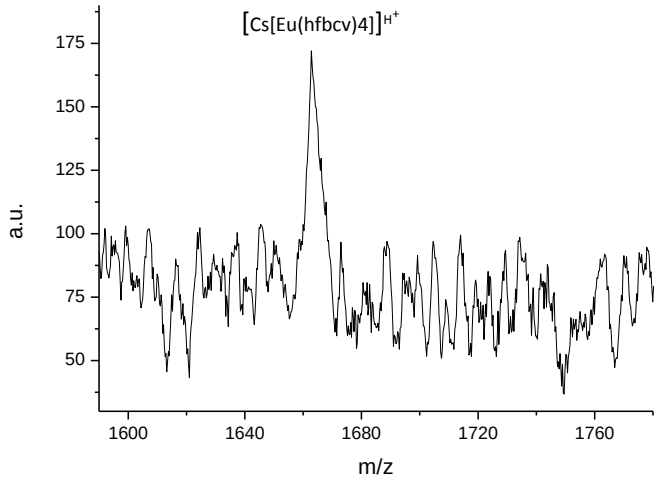

Figure A2-7. Positive MALDI-TOF mass spectrum of Cs[Eu(*(R)*-hfbcv)$_4$].

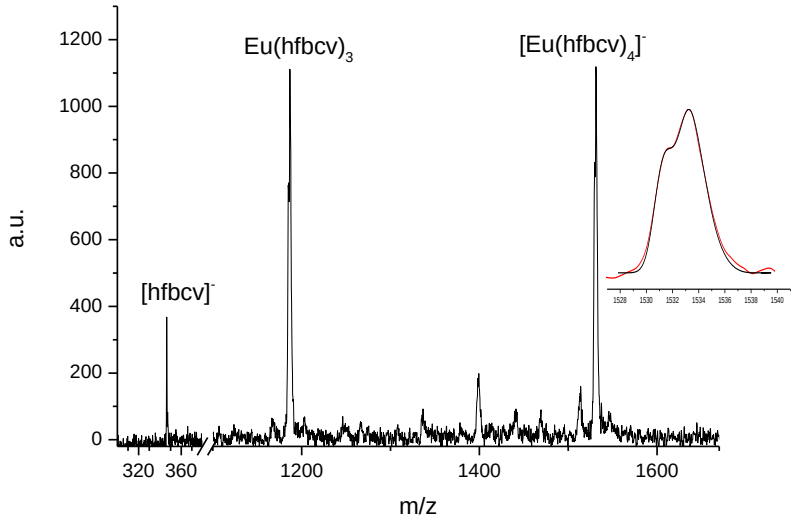

Figure A2-8. Negative MALDI-TOF mass spectrum of Cs[Eu(*(R)*-hfbcv)$_4$]. In the inset, for the sake of comparison, the experimental isotopic cluster peaks of [Eu(*(R)*-hfbcv)$_4$]$^-$ species (red line) and its simulated isotopic distribution (black line), FWHM = 860, is reported. The peak in the inset was smoothed using Savitzky-Golay filter.

Appendix to Chapter 3

The complexes were synthesized following a slightly modified literature procedure,[A6] described below. Their identity and purity was confirmed by comparing ^{1}H-NMR (Agilent Inova 600 operating at 14.1 T) spectra with the literature data.

Synthesis of CsEu(*(+)*-hfbc)$_4$

CsCl (200 mg, 1.01 mmol) and $EuCl_3$ (132 mg, 0.50 mmol) were dissolved in H_2O (20 mL). In the mean time a solution containing *(+)*-heptafluorobutyrylcamphor (*(+)*-hfbcH; 0.54 mL, 2.04 mmol) and triethylamine (0.30 mL, 2.15 mmol) in $CHCl_3$ (30 mL) was prepared. The two solutions were mixed together. The resulting biphasic system was left for 1 hour at room temperature under vigorous stirring.

The $CHCl_3$ layer was recovered and the aqueous phase was extracted with fresh $CHCl_3$ (2x15 mL). The combined organic phases were washed with water (3x15

mL), dried over anhydrous Na_2SO_4 and the solvent was removed under vacuum. The crude product was crystallized from hot CH_3CN.

The title compound was obtained as white needle crystals in 21% yield.

^{1}H-NMR ($CDCl_3$, 600 MHz, 25.0 °C, broad singlets), δ (ppm): 5.20 (Me^3); -0.89 (Me^2); -0.99 (A); -1.66 (C); -2.72 (Me^1+D); -4.55 (E); -6.35 (B).

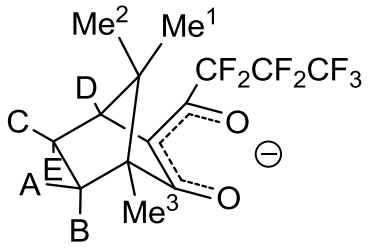

Synthesys of CsEu(*(–)*-hfbc)$_4$

For the synthesis of CsEu(*(–)*-hfbc)$_4$, the same procedure reported above for CsEu(*(+)*-hfbc)$_4$ was followed. Yield 23%; same ^{1}H NMR data as above.

CPL measurements

The instrumental set-up for detection of circular polarization of emitted light consisted in a Spex 270M monochromator combined with CCD allowing one to measure the whole spectrum simultaneously. Between the sample and the detector we put a quarter wave plate (Thorlabs, AQWP05M-600) which was rotated through angles defining the orientation of the easy axis vs. the linear polarizer (Oriel 25010), which was kept fix.

Setup calibration

We validated the CPL measurements using $CHCl_3$ solutions ($2\cdot10^{-3}$ M, λ_{exc}=365 nm) of each CsEu(hfbc)$_4$ enantiomer. The emission of each solution was measured by rotating the quarter wave plate by ±45°; the measurements were repeated 6 times for each equivalent position of the quarter wave plate for each

solution. The CPL spectrum (Figure 3b) was obtained by subtracting the left and right component of the emission (I_L-I_R); the g_{PL}-s were calculated using the definition:

$$g_{PL} = 2\frac{I_L - I_R}{I_L + I_R} \qquad \text{(A3-1)}$$

averaging over the whole set of measurements. The total intensity (I_L+I_R) was corrected by subtracting the background (the background signal was generally below 5% of the least intense band). The CPL spectra obtained for the two enantiomers were mirror-like, as expected. This rules out any linear birefringence contribution in the measurement apparatus. The calculated g_{PL} values were in very good agreement with the ones reported in the literature[A7] for CsEu(*(+)*-hfbc)$_4$

CPEL measurements on the OLEDs

The devices were turned on by applying 10-12 V (corresponding to 20 mA/cm^2) and were let stabilize for several seconds (15-20 sec) before the measurement. The differential emission was measured by rotating the quarter wave plate by ±45°, as described above for the solutions. The measurements were repeated at least 4 times for each equivalent position of the quarter wave plate for each LED pixel. This set of measurements was repeated at least on 5 pixels for each device. The CPL spectra and g_{EL} values were obtained as described above. Each spectrum was acquired with a single accumulation, integration time = 1.5 sec.

OLED fabrication

A blend of PVK:OXD7:CsEu(hfbc)4 in the mass ratio (3:1:0.4) was dissolved in CHCl3 15 mg/mL. Indium tin oxide (ITO; 15 Ω per square) substrates were cleaned by sonication in distilled water, acetone, and isopropyl alcohol. After treatment with nitrogen plasma, a thin film (40 nm) of filtered (nylon 0.45 μm) poly-(3,4-ethylenedioxythiophene)-poly(styrenesulfonic acid) (PEDOT:PSS, Clevios P VP AI 4083, H.C. Starck) used as a hole-injection layer at the anode interface was spin-coated onto the ITO substrate, and then dried under nitrogen atmosphere at 150 °C for 15 minutes.

A film of emitting blend (65-120 nm) was then spin-coated. A thin layer of barium (4 nm) and subsequently a layer of Al (6-80 nm) were deposited on the top by vacuum (5·10-7 mbar) thermal evaporation. The device active area was 5.4 mm2. All operations were carried out inside a nitrogen-filled drybox with less than 0.1 ppm of both oxygen and water.

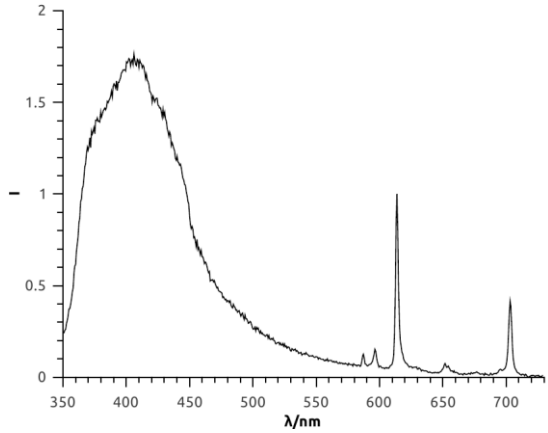

Figure A3-1. Total photoluminescence of the blend film (λ_{exc} = 320 nm).

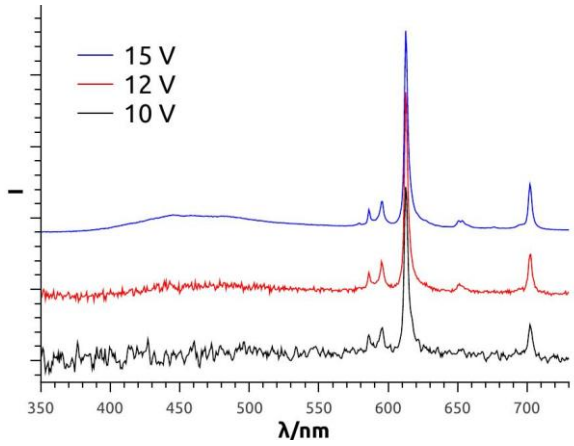

Figure A3-2. Voltage dependence of EL spectra of a ITO/PEDOT:PSS/PVK:OXD7: CsEu((–)-hfbc)4/Ba/Al device (10-15 V). Spectra are vertically shifted for clarity.

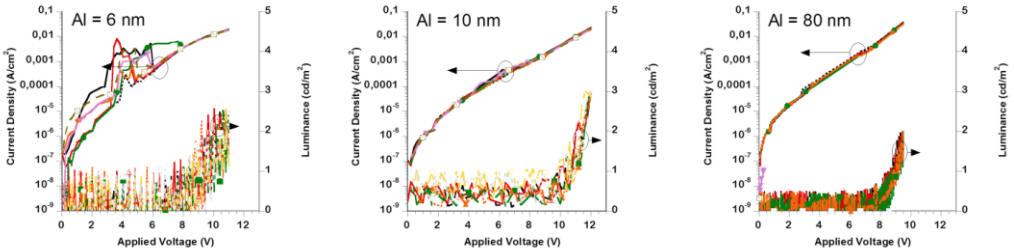

Figure A3-4. Reproducibility (8 sweeps) of current density-brightness-voltage curves of ITO/PEDOT:PSS/PVK:OXD7: CsEu((+)-hfbc)$_4$/Ba/Al devices with 6 nm (left), 10 nm (center) and 80 nm Al cathode (right).

Active layer film Morphology

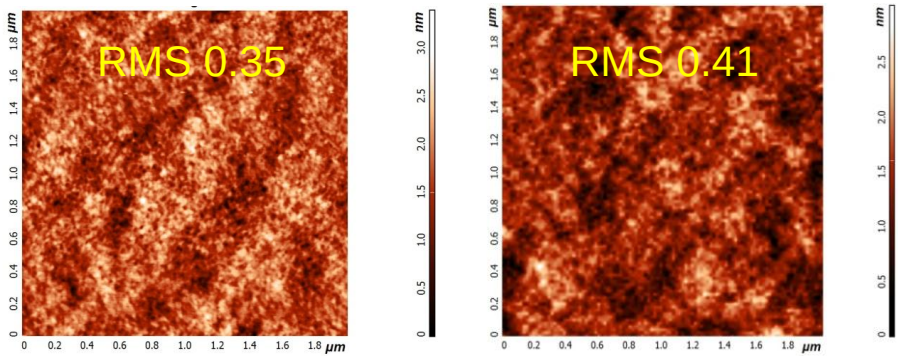

Figure A3-5. Left: AFM topography images of CsEu((+)-hfbc)$_4$. **Right:,** CsEu((-)-hfbc)$_4$ dispersed in PVK:OXD7. Root mean square roughness (RMS) values are reported.

Appendix to Chapter 4

Table A4-1. HOMO, LUMO, energy levels and charge carrier mobility of host materials.

Compounds	**HOMO** (eV)	**LUMO** (eV)	**triplet energy $T_1 \rightarrow S_0$** (eV)	**Charge carrier Mobility** (cm^2/Vs)		**Ref.**
TCTA	-5.7	-2.3	2.8	$\sim 10^{-4}$	/	[S2, S3]
OXD7	-6.2	-2.6	/	/	$\sim 10^{-5}$	[S4]

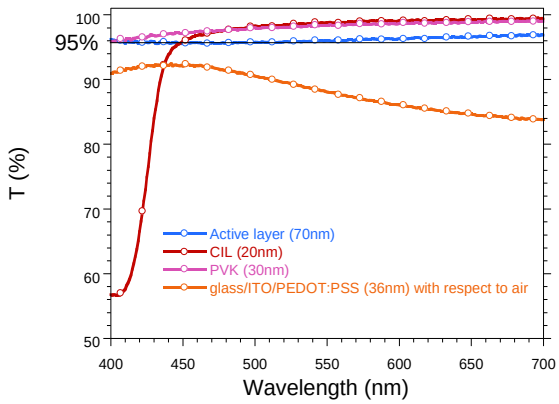

Figure A4-1. Transmittance spectra of the various layers of the device

Effects of the electrodes-recombination zone (RZ) position on the polarization efficiency

As in our previous model,[A8] we consider that half of the radiation is emitted forward and half backward. According to Beer–Lambert law, the emitted light (I_0) is attenuated exponentially with the distance x between the anode (where the light exits the device) and the recombination zone, where the photon is generated:

$$I = I_0 e^{-\alpha x} \qquad \text{(A4-1)}$$

where α is the attenuation coefficient of the all the layers between the anode and the cathode. Eq. (A4-1) is related to the total transmittance T (including absorption, scattering and any other dissipation process) of the layers as $T = e-\alpha d$.

In first approximation, we shall consider that the light is emitted only by an infinitesimally thin layer of the active layer (see Figure A4-1). The loss of the fraction of the light emitted backward and forward varies with the distance of the recombination zone from the cathode according to Eq. (A4-1). The backward component eventually undergoes reflection on the cathode, and therefore its handedness is reversed.

The pathway travelled by the backward light is conveniently divided into three steps:

In the way between the RZ and the cathode, it is attenuated by a factor $e^{-\alpha(d-x)}$.

Owing to the reflection on the cathode surface it is further attenuated by a factor R (reflectance) and its handedness is reversed.

In the way back from the cathode to the anode, it is finally attenuated by a factor $e^{-\alpha d}$.

The total attenuation factor is therefore:

$$R \cdot e^{-\alpha(2d-x)} \qquad \text{(A4-2)}$$

Applying these attenuation factors to the two intrinsic polarized component ($I_L^{(0)}$ and $I_R^{(0)}$) and taking into account the sign reversal of the polarization after reflection, we have that the two polarized components exiting the device (I'_L and I'_R) are:

$$I'_L = \frac{1}{2} I_L^{(0)} \cdot e^{-\alpha x} + \frac{1}{2} I_R^{(0)} \cdot R \cdot e^{-\alpha(2d-x)} \qquad \text{(eq. A4-2a)}$$

$$I'_R = \frac{1}{2} I_R^{(0)} \cdot e^{-\alpha x} + \frac{1}{2} I_L^{(0)} \cdot R \cdot e^{-\alpha(2d-x)} \qquad \text{(A4-2b)}$$

Where $I_L^{(0)}$ and $I_R^{(0)}$are the intrinsic polarization components emitted by the chiral molecule. Factor ½ is needed because half of the light is emitted forward and half backward.

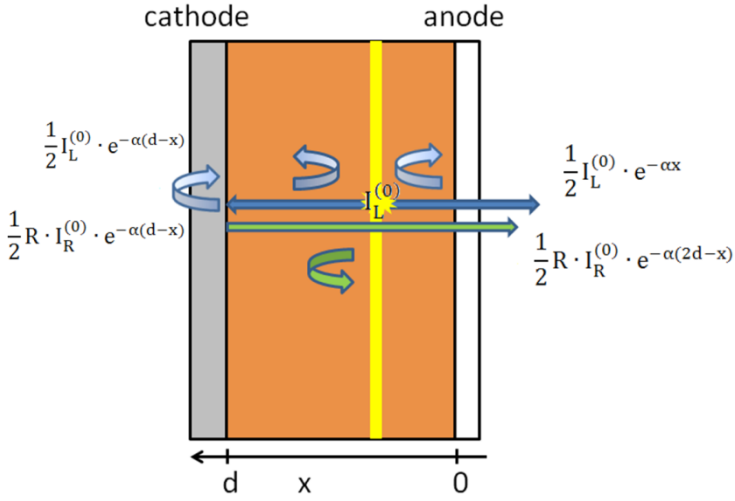

Figure A4-1. Schematic representation of a device. The yellow strip represents the recombination zone, curved arrows represent light losses. Light before reflection is indicated in blue, light after reflection is indicated in green. On top of each arrow, we report the attenuation for the left polarized component.

The overall g_{EL} factor that we measure for the device is:

$$g_{EL} = 2\frac{I'_L - I'_R}{I'_L + I'_R} \qquad \text{(A4-3)}$$

By substituting Eq. (A4-2a) and (A4-2b) in Eq. (A4-3) and rearranging the terms, we obtain:

$$g_{EL} = 2\frac{e^{-\alpha x}\left(I_L^{(0)} - I_R^{(0)}\right) - R \cdot e^{-\alpha(2d-x)}\left(I_L^{(0)} - I_R^{(0)}\right)}{e^{-\alpha x}\left(I_L^{(0)} + I_R^{(0)}\right) + R \cdot e^{-\alpha(2d-x)}\left(I_L^{(0)} + I_R^{(0)}\right)} = 2\frac{\left(I_L^{(0)} - I_R^{(0)}\right)}{\left(I_L^{(0)} + I_R^{(0)}\right)} \cdot \frac{e^{-\alpha x} - R \cdot e^{-\alpha(2d-x)}}{e^{-\alpha x} + R \cdot e^{-\alpha(2d-x)}}$$

(eq. A4-4)

We note that $2\frac{\left(I_L^{(0)} - I_R^{(0)}\right)}{\left(I_L^{(0)} + I_R^{(0)}\right)} = g_{EL}^{(0)}$, i.e. the intrinsic g factor of the chiral emitter, and by substituting it in Eq. (A4-4), after multiplying both the numerator and denominator by $e^{+\alpha x}$, we get:

$$g_{EL} = g_{EL}^{(0)} \frac{1 - R \cdot e^{-2\alpha(d-x)}}{1 + R \cdot e^{-2\alpha(d-x)}} \qquad \text{(A4-5)}$$

Eq. (A4-5) shows that g_{EL} monotonously increases with x, meaning that higher g_{EL}-s are expected when the recombination zone is close to the anode interface.

It is worth noting that when the recombination occurs very close to the anode (x = 0), Eq. (A4-5) becomes:

$$g_{EL} = g_{EL}^{(0)} \frac{1-R \cdot e^{-2\alpha d}}{1+R \cdot e^{-2\alpha d}} \quad \text{(A4-6)}$$

Since $e^{-\alpha d} = T$, i.e. the overall transmittance of the active layer and the CIL, Eq. (A4-6) becomes:

$$g_{EL} = g_{EL}^{(0)} \frac{1-R \cdot T^2}{1+R \cdot T^2} \quad \text{(A4-7)}$$

In the opposite case, when the recombination occurs very close to the cathode (x = d), we have:

$$g_{EL} = g_{EL}^{(0)} \frac{1-R}{1+R} \quad \text{(A4-8)}$$

Eq. (A4-8) is the equation worked out in our previous model, which did not take into account loss of radiation within the layers between anode and cathode.

References

[A1] Gaussian 09, Revision D.01, M. J. Frisch, G. W. Trucks, H. B. Schlegel, G. E. Scuseria, M. A. Robb, J. R. Cheeseman, G. Scalmani, V. Barone, B. Mennucci, G. A. Petersson, H. Nakatsuji, M. Caricato, X. Li, H. P. Hratchian, A. F. Izmaylov, J. Bloino, G. Zheng, J. L. Sonnenberg, M. Hada, M. Ehara, K. Toyota, R. Fukuda, J. Hasegawa, M. Ishida, T. Nakajima, Y. Honda, O. Kitao, H. Nakai, T. Vreven, J. A. Montgomery, Jr., J. E. Peralta, F. Ogliaro, M. Bearpark, J. J. Heyd, E. Brothers, K. N. Kudin, V. N. Staroverov, R. Kobayashi, J. Normand, K. Raghavachari, A. Rendell, J. C. Burant, S. S. Iyengar, J. Tomasi, M. Cossi, N. Rega, J. M. Millam, M. Klene, J. E. Knox, J. B. Cross, V. Bakken, C. Adamo, J. Jaramillo, R. Gomperts, R. E. Stratmann, O. Yazyev, A. J. Austin, R. Cammi, C. Pomelli, J. W. Ochterski, R. L. Martin, K. Morokuma, V. G. Zakrzewski, G. A. Voth, P. Salvador, J. J. Dannenberg, S. Dapprich, A. D. Daniels, Ö. Farkas, J. B. Foresman, J. V. Ortiz, J. Cioslowski, and D. J. Fox, Gaussian, Inc., Wallingford CT, **2009**.

[A2] L. Di Bari and P. Salvadori, Coord. Chem. Rev., **2005**, *249*, 2854.

[A3] S. Di Pietro, S. Lo Piano, L. Di Bari, Coord. Chem. Rev., **2011**, *255*, 2810.

[A4] S. Di Pietro and L. Di Bari, Inorg. Chem., **2012**, *51*, 12007.

[A5] J. C. Cobas, M. Martin-Pastor, EXSYCalc Version 1.0, Mestrelab Reasearch.

[A6] D. Shirotani, T. Suzuki, K. Yamanari, S. Kaizaki, *J. Alloys Compd.* **2008**, 451, 325.

[A7] J. L. Lunkley, D. Shirotani, K. Yamanari, S. Kaizaki, G. Muller, *Inorg. Chem.* **2011,** 50, 12724.

[A8] F. Zinna, U. Giovanella, L. Di Bari, *Adv Mater* **2015**, *27*, 1791.

Appendix B

Appendix to Chapter 6

CPL measurements

Absorption and ECD spectra were measured with a JASCO V-650 Spectrophotometer and a JASCO J-710 spectropolarimeter, respectively, on $5 \cdot 10^{-5}$ M CH_2Cl_2 solutions using a 1 cm quartz cell. CPL and fluorescence spectra were recorded on $5 \cdot 10^{-5}$ M CH_2Cl_2 solutions with a home-built instrument. The samples were excited with a 90° geometry using a green LED source (λ_{max} = 517 nm, HWHM = 15 nm). 2 accumulations were needed for compound **1** (scan-speed 1 mn/sec, total acquisition time ~5 min), while 4 accumulations were needed for compound **2** (scan-speed 1 mn/sec, acquisition time ~10 min).

Calculations

All DFT-based computations were run with the Gaussian'09 program.[B1] DFT and TDDFT calculations were run with the hybrid M06-2X functional[B2] and the triple-ζ basis set with polarization functions def2-TZVP. [B3] Other functionals (CAM-B3LYP, ωB97X-D, M06-HF) and basis sets (TZVP, def2-SVP) were also tested. All calculations were performed in vacuo. Some representative calculations were run including a solvent model for dichloromethane, using a state-specific vertical excitation model (VEM).[B4] Ground-state geometries were optimized with DFT at M06-2X/def2-TZVP level and verified as true minima by frequency calculations at the same level. Excited-state calculations were run with TDDFT at M06-2X/def2-TZVP level. Fluorescence and CPL spectra were normalized at the maximum of fluorescence. In this way, the CPL spectra reflect immediately the corresponding g_{PL} values. [B5] SCS-CC2 (spin-component scaling approach for second-order approximate coupled-cluster) calculations[B6-B7] were done with Turbomole[B8-B9] applying the resolution-of-identity (RI)

approximation. For compound **1** the def2-SVP basis set was used while for **2a** the def2-TZVP basis set was used. All spectra were obtained as sums of Gaussians with σ = 0.1 eV exponential half-width. Calculated spectra were shifted by 0.4 eV to the red in the comparison with experimental spectra.

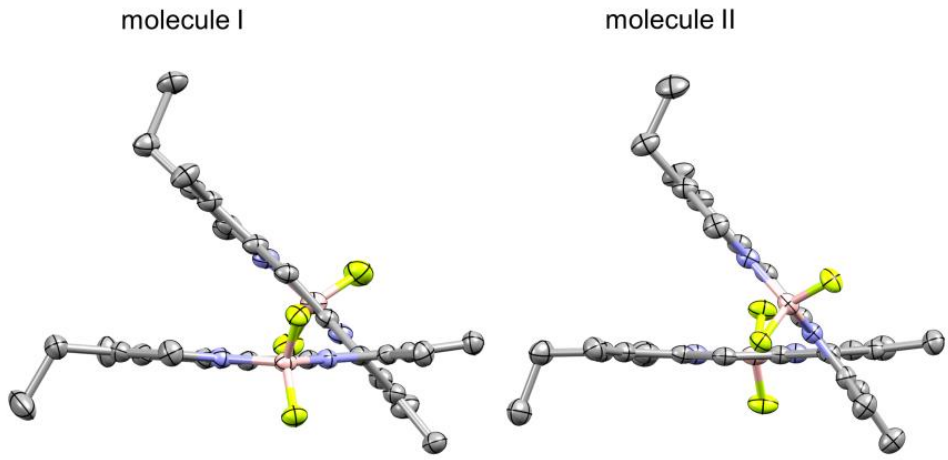

Figure B6-1. Selected views of the two independent molecules in the unit cell of **2** (hydrogen atoms removed for clarity; thermal ellipsoids set at 50% probability).

Appendix to Chapter 7

CPL measurements

The samples were excited using a 90° geometry with a green LED source (λ_{max} = 517 nm, HWHM = 15 nm). The concentration of all the samples was $2/3.10^{-5}$ M. The spectra were baseline corrected by subtracting the spectrum of the racemic mixture. Each spectrum is the average of 8 accumulations (scan-speed 1 mn/sec, acquisition time ~27 min).

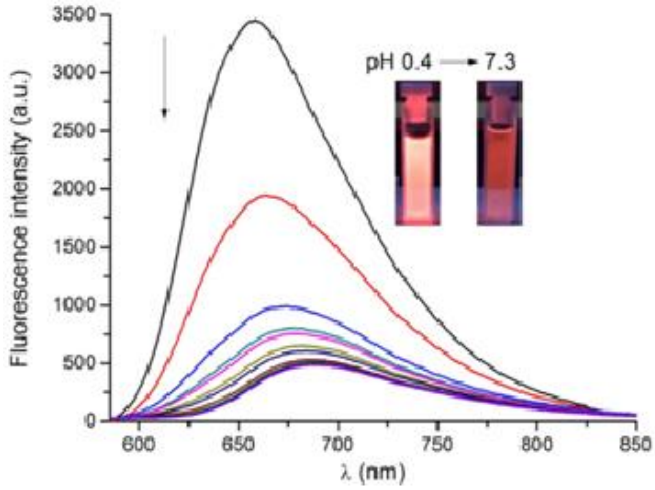

Figure B7-1. pH-dependent absorption and fluorescence spectra of **1**/**1-H** in aqueous solution (*ca.* 10^{-5} M). Insert: Optical density measured at 630 nm in function of the pH for **1/1-H** in aqueous solution.

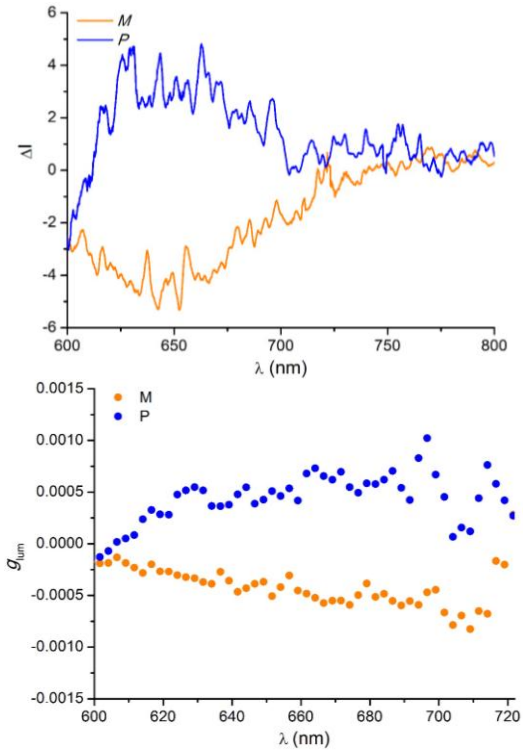

Figure B7-2. CPL spectra (left) and g_{PL} response (right) of the two enantiomers of **1-H** in aqueous solution (HCl 1 M). λ_{exc} = 517 nm.

Appendix to Chapter 8

Materials and Methods

Materials

Proteins Three different proteinaceous painting media were selected for this study: dried egg white from chicken (Sigma Aldrich, for egg), casein powder (Zecchi, from cow milk) and rabbit skin glue (Zecchi, for animal tissue). Ovalbumin from chicken (**OVA**) was from Sigma Aldrich (purity > 97 %). The materials were added to buffer solutions and sonicated in ultrasonic bath until total solubilization of the sample. The molar concentration of the protein will be indicated as CP.

Fluorescent tags Sypro Ruby was the protein blot stain by Molecular Probes. Flamingo was purchased as a solution in 35-50 % ethanol, 2.5-5 %, methanol, 0.01-0.1 % dimethyl sulfoxide and 35-50 % water mixture (BioRad). For these two dyes the molar concentration of the dyes was evaluated using the molar absorption coefficients ε (463 nm) = 19·103 $M^{-1}cm^{-1}$ for Sypro Ruby and ε (508 nm) = 1·105 $M^{-1}cm^{-1}$ for Flamingo. AMCA (succinimydyl-7-amino-4-methylcoumarin-3-acetic acid) and FITC (fluorescein isothiocyanate) were purchased from Sigma-Aldrich as powders; AMCA-X (6-((7-Amino-4-methylcoumarin-3-acetyl)amino) hexanoic acid, N-succinimidyl ester) solid was purchased from Adipogen life Sciences. Working solutions of the above dyes were obtained by dissolving weighted amount of the solid in DMSO and kept in the dark at 4 °C. The molar concentration of the dyes will be indicated as CD.

Buffers Experiments were carried out at pH 7.2 in 50 mM Tris-HCl, 0.28 M NaCl (buffer 1) or 0.1 M Na2CO3 pH 9.0 (buffer 2). Solutions were prepared with milliQ water.

Embedding resin Hardrock 554 epoxy resin and hardner were purchased from Tecnocontrol, Italy.

Methods

Cross sections and OM observation

After curing of the epoxy resin the blocks were cut and polished to reveal the casein and polysaccharide gum layer in cross section. The cross sections were dry polished with successively finer grades of micromesh abrasive cloths (600, 800 and 1200 mesh). Felt was used for the final polishing. The cross-sections were observed at different magnifications (from 5× to 20×) using an BX51M imaging binocular microscope and the images were acquired using a Olympus XC30 digital color camera, coupled to the microscope (provided with a mercury lamp USH-1030OL).

The staining test on cross-sections was carried out depositing few drops of the stain solution on the embedded protein and leaving it in the dark for 10 min. The cross-section was then washed with a solvent (hexane for SYPRO Ruby, Flamingo and DMSO for FITC, NHS-AMCA and NHS-AMCA-X) 3 times.

Fluorescence experiments

Protein solubilization was carried out using an Sonorex super 10 P (Bandelin) ultrasonic bath, by applying to suitable proteinaceous materials sample one cycle of 60' at 25 °C.

Measurements of pH were made by a Metrohm 713 pH-meter equipped with a combined glass electrode.

Fluorescence measurements were carried out on a PerkinElmer LS55 spectrofluorometer. Fluorescence titrations were performed at λ_{exc} = 490 nm (Flamingo), λexc = 470 nm (Sypro), λ_{exc} = 450 nm (FITC) and λ_{exc} = 350 nm (AMCA and AMCA-X). The titrations were done using a batch wise procedure: several samples were prepared containing the same amount of fluorescent dye (0.28 μM Flamingo, 6.4 μM Sypro Ruby, 0.55 μM FITC, 0.38 μM AMCA and 0.25 μM AMCA-X) and increasing amounts of protein.

As for data treatment, the model used is based on the (reasonable) assumption that, under the diluted dye conditions used, the intensity of the emitted light is proportional to the molar concentration, i.e. relationships analogous to the Beer's law do apply. In the fluorescence titrations we measure the light emission changes upon the addition of proteins. The association of fluorescent tags/dyes (D) with proteins (P) may be represented by the following equation:

$P + D \leftrightarrows PD$

where the related association constant is defined as $K_b = [PD]/([P]\cdot[D])$. The association constants were determined by the fluorescence spectral changes using the Eq. (B8-10) that is derived as described below.

$$K_b = \frac{[PD]}{[P][D]} \quad \text{(B8-1)}$$

$$C_P = [P] + [PD] \quad \text{(B8-2)}$$

$$C_D = [D] + [PD] \quad \text{(B8-3)}$$

where C_P and C_D are total analytical concentrations. If D and PD only emit light, then:

$$F = F_D + F_{PD} = \varphi_D [D] + \varphi_{PD} [PD] \quad \text{(B8-4)}$$

If we now define

$$\Delta F = F - \varphi_D - C_D \quad \text{(B8-5)}$$

$$\Delta\varphi = \varphi_{PD} - \varphi_D \quad \text{(B8-6)}$$

Eq. (B8-4) becomes

$$\Delta F = \Delta\varphi[PD] \quad \text{(B8-8)}$$

Introduction of Eq. (B8-2) and (B8-3) into (B8-1) yields

$$K_b = \frac{[PD]}{(C_P - [PD])(C_D - [PD])} \quad \text{(B8-9)}$$

Substituting [PD] obtained from Eq. (B8-7) into Eq. (B8-8) and rearranging, one obtains

$$\frac{C_P C_D}{\Delta F} + \frac{\Delta F}{\Delta\varphi^2} = \frac{1}{K_b \Delta\varphi} + \frac{C_P + C_D}{\Delta\varphi} \quad \text{(B8-10)}$$

which corresponds to Eq. (B8-8) of the text. Such equation enables K_b and $\Delta\varphi$ to be obtained by an iterative procedure. That is, disregarding the $\Delta F/\Delta\varphi^2$ term on first approximation, $\Delta\varphi$ can be calculated from the reciprocal of the slope of the straight line interpolating the data of the $C_P C_D/\Delta F$ vs. (C_P+C_D). Then, introduction of this $\Delta\varphi$ value into Eq. (B8-9) enables the $(C_P C_D/\Delta F + \Delta F/\Delta\varphi^2)$ term to be evaluated and new values of K_b and $\Delta\varphi$ to be obtained. The procedure is repeated until convergence is reached. Eq. (B8-9) is a modification of the Hildebrand and Benesi Equation[B10] and is valid also if the conditions of protein excess are not fulfilled.

CPL measurements

The measurement were carried out on solutions containing 6.4 μM Sypro Ruby or 0.55 μM FITC and 245 μM protein concentration.

All the samples were excited using a 90° geometry. Spectra of the samples containing Sypro Ruby were excited using a blue LED source (λ_{exc} = 470 nm) and are the average of 8 accumulations each. Spectra of the samples containing FITC were excited using a UV fluorescent lamp (λ_{exc} = 365 nm) and are the average of 4 accumulations each (scan-speed 1 mn/sec, acquisition time ~13 min). The spectra were not corrected for the baseline.

References

[B1] Gaussian 09, Revision D.01, M. J. Frisch, G. W. Trucks, H. B. Schlegel, G. E. Scuseria, M. A. Robb, J. R. Cheeseman, G. Scalmani, V. Barone, B. Mennucci, G. A. Petersson, H. Nakatsuji, M. Caricato, X. Li, H. P. Hratchian, A. F. Izmaylov, J. Bloino, G. Zheng, J. L. Sonnenberg, M. Hada, M. Ehara, K. Toyota, R. Fukuda, J. Hasegawa, M. Ishida, T. Nakajima, Y. Honda, O. Kitao, H. Nakai, T. Vreven, J. A. Montgomery, Jr., J. E. Peralta, F. Ogliaro, M. Bearpark, J. J. Heyd, E. Brothers, K. N. Kudin, V. N. Staroverov, R. Kobayashi, J. Normand, K. Raghavachari, A. Rendell, J. C. Burant, S. S. Iyengar, J. Tomasi, M. Cossi, N. Rega, J. M. Millam, M. Klene, J. E. Knox, J. B. Cross, V. Bakken, C. Adamo, J. Jaramillo, R. Gomperts, R. E. Stratmann, O. Yazyev, A. J. Austin, R. Cammi, C. Pomelli, J. W. Ochterski, R. L. Martin, K. Morokuma, V. G. Zakrzewski, G. A. Voth, P. Salvador, J. J. Dannenberg, S. Dapprich, A. D. Daniels, Ö. Farkas, J. B. Foresman, J. V. Ortiz, J. Cioslowski, and D. J. Fox, Gaussian, Inc., Wallingford CT, **2009**.

[B2] Y. Zhao, D. G. Truhlar, *Theor. Chem. Acc.* **2007**, *120*, 215.

[B3] F. Weigend, R. Ahlrichs, *Phys. Chem. Chem. Phys.* **2005**, *7*, 3297.

[B4] A. V. Marenich, C. J. Cramer, D. G. Truhlar, C. A. Guido, B. Mennucci, G. Scalmani, M. J. Frisch, *Chem. Sci.* **2011**, *2*, 2143.

[B5] G. Longhi, E. Castiglioni, S. Abbate, F. Lebon, D. A. Lightner, *Chirality* **2013**, *25*, 589.

[86] H. Christof, F. Weigend, *J. Chem. Phys.* **2000**, *113*, 5154.

[87] A. Hellweg, S. A. Grun, C. Hattig, *Phys. Chem. Chem. Phys.* **2008**, *10*, 4119.

[B8] F. Furche, R. Ahlrichs, C. Hättig, W. Klopper, M. Sierka, F. Weigend, *WIREs Comput. Mol. Sci.* **2014**, *4*, 91.

[B9] TURBOMOLE, Version 6.6. R. Ahlrichs, M. K. Armbruster, R. A. Bachorz, M. Bär, H.-P. Baron, R. Bauernschmitt, F. A. Bischoff, S. Böcker, N. Crawford, P. Deglmann, F. Della Sala, M. Diedenhofen, M. Ehrig, K. Eichkorn, S. Elliott, D. Friese, F. Furche, A. Glöß, F. Haase, M. Häser, C. Hättig, A. Hellweg, S. Höfener, H. Horn, C. Huber, U. Huniar, M. Kattanek, W. Klopper, A. Köhn, C. Kölmel, M. Kollwitz, K. May, P. Nava, C. Ochsenfeld, H. Öhm, M. Pabst, H. Patzelt, D. Rappoport, O. Rubner, A. Schäfer, U. Schneider, M. Sierka, D. P. Tew, O. Treutler, B. Unterreiner, M. von Arnim, F. Weigend, P. Weis, H. Weiss, N. Winter. Karlsruhe, Germany, 2014.

[B10] H. A. Benesi and J. Hildebrand, *J. Am. Chem. Soc.*, **1949**, 71, 2703.

Acknowledgment

I would like to thank my research group at the University of Pisa, where this work was carried out. I am grateful to my supervisor Prof. Lorenzo Di Bari for his inspiring guidance throughout these years and to Prof. Gennaro Pescitelli for his constant help and stimulating criticism.

I am indebted to all the collaborators whose experience was essential to accomplish the results presented here.

Prof. Sergio Abbate, Prof. Giovanna Longhi for their help with our first CPL measurement (Chapter 2) and Dr. Ettore Castiglioni who gave valuable suggestions on renovating and operating the CPL instrument but unfortunately passed away before seeing it fully working.

Dr. Umberto Giovanella who lent us his skills in manufacturing the CP-OLEDs discussed in Chapter 3 ad 4.

Prof. Martin Bröring and Dr. Johannes Ahrens for the synthesis of the BODIPY derivatives and Prof. Gennaro Pescitelli and Dr. Torsten Bruhn for calculations (Chapter 6).

Prof. Jérôme Lacour and Dr. Simon Pascal for the synthesis of the helicenes detailed in Chapter 7 and for having involved us in their project on *chiroptical switch*.

Prof. Ilaria Bonaduce, Dr. Tarita Biver and Ms. Sibilla Orsini for having provided us with a stimulating problem and with the samples described in Chapter 8.

Finally I would like to thank Mr. Manrico Nardi and Mr. Paolo Nardini whose craftsmanship in manufacturing custom objects was highly valuable and Mr. David Michelotti for technical support with electronic equipment.